学位論文

The nature of star forming galaxies and environmental influence during cluster formation

(銀河団形成期における星形成銀河の性質および環境依存性に関する研究)

平成29年 12月 博士 (理学) 申請

東京大学大学院理学系研究科
天文学専攻
李　民主

Minju M. Lee

The nature of star forming galaxies and environmental influence during cluster formation

Abstract

Galaxies are formed in various environments of the Universe, such as clusters, groups, fields and voids. During the last decade, we have seen a great improvement in understanding galaxy formation and evolution in field population at high redshift. Several dedicated observations on gas content and kinematics have been conducted toward star forming galaxies in general fields; at least up to $z \sim 3$, both a large gas content and efficient star formation explain the high cosmic star forming activity at high redshift galaxies, and turbulence in gas has been also found to increase. In contrast, such observations are lack in overdense regions at high redshift. Overdense regions in the early Universe are expected to be a progenitor of the present-day clusters of galaxies, so that we refer as protoclusters.

Probing star-forming galaxies in protoclusters is essential for understanding the formation mechanism of disks and early-type galaxies, and environmental effects at the very early epoch of cluster and galaxy formation. A few observations in overdense regions have focussed only on extremely bright populations of star-forming galaxies and AGNs, which are easy to probe in more details. Observational studies of less extreme, typical star-forming galaxies have been desired but not executed yet, because they need large survey volumes, spectroscopic confirmation of member galaxies and a proper sample selection of protoclusters. Recently, well-defined overdense regions as targets for the studies have been increasing by large surveys, and allowed us to perform systematic surveys of star forming galaxies in overdense regions.

In this Thesis, we report on a systemic study on the cold gas properties for the first time toward typical star forming galaxies in a $z = 2.49$ protocluster, which is one of the overdense regions of H-alpha emitters (HAEs), the star forming galaxies. We observed the HAEs in dust continuum emission at 1.1 mm and in CO rotational transitional lines (CO (3–2) and CO (4–3)) with Atacama Large Millimeter/submillimeter Array (ALMA); our sample for the study consists of 25 HAEs found by the Subaru telescope.

We probe the global gas content of the star forming galaxies associated to the protocluster by using the 1.1 mm dust continuum and CO (3–2) emissions observed at spatial resolutions of $0''.7 - 0''.9$. We detect the CO (3–2) emission from seven HAEs and the 1.1 mm dust continuum from four HAEs, among 22 and 19 HAEs targeted, respectively. Two independent gas-mass estimates from the CO (3–2) and 1.1 mm are consistent with each other for simultaneous detections. From the gas measurements, we find that the average gas fraction of the star forming galaxies is comparable to that of field galaxies, with $f_{\rm gas} (= M_{\rm gas}/(M_{\rm gas} + M_{\star}))$ of 0.53 ± 0.07. We find a correlation between the gas fraction and mass, and between the gas fraction and the local density, though the latter case is very marginal. Furthermore, we find that the average depletion-time scales of HAEs are similar to those obtained in fields. A positive correlation between the global star forming efficiency and the stellar mass is tentatively found in the mass range of

$\log M_\star = [10.64, 11.30]$. Further studies are necessary for the confirmation of the correlation by observing a larger number of galaxies in a wider mass range.

We also analyze CO (4–3) data observed toward 16 HAEs, a subset of 22 HAEs observed in CO (3–2). We detect a total of ten HAEs in CO (4–3); five galaxies are previously detected in CO (3–2) line, and other five HAEs are newly detected in CO (4–3). The redshifts are roughly consistent between CO (3–2) and CO (4–3) for the five HAEs, which provides more robust detection of the CO emissions. From the CO redshifts, we calculate the halo mass of the protocluster and the estimate suggests the protocluster to be a possible candidate for local Virgo-like clusters. The spatial resolution in CO (4–3) is $0''.3 \times 0''.5$, which is improved by a factor of two than our previous CO (3–2) observations. Two galaxies, HAE8 and HAE16, are detected in relatively high $S/N > 8$, and show indications of disk-like galaxies with smooth velocity gradients in the data cubes. It allows us to make a detailed kinematic model for these galaxies. From the best-fit model, we estimate a ratio between rotational velocity ($V_{\rm rot}$) and intrinsic velocity dispersion (σ_0), which evaluates how rotation dominates the gas kinematics. HAE16 shows a clear velocity gradient and $V_{\rm rot}/\sigma_0 \simeq 2$, and HAE8 has a less clear velocity gradient with a narrower line width and $V_{\rm rot}/\sigma_0 \simeq 10$. Provided the average value that found in fields, which is $V_{\rm rot}/\sigma_0 \sim 4$, the ratios found for protocluster galaxies seem to be consistent with that obtained in general fields, if we consider a large scatter of the observed $V_{\rm rot}/\sigma_0$ in field disk-like galaxies and a large uncertainty in the estimate from the modeling. We also find that these two galaxies are consistent with local spiral galaxies in terms of the specific angular momentum; they need to lose the angular momentum to evolve into elliptical galaxies. Also, they are located within the expected range of Tully-Fisher relation at high redshift ($z \sim 2$). In addition to these disk-like population, we also find three candidates of mergers or interacting galaxies by investigating CO line widths and images in CO velocity channels together with a help of multi-band Opt/IR data sets, e.g., high spatial resolution Ks-band images. Such merger candidates need to be investigated by future deeper, higher angular resolution observations for the confirmation.

Our findings on cold gas properties suggest that the nature of protocluster galaxies is, on average, similar to those in general fields. We find no clear environmental dependence, although some tentative hints are found; (1) a larger (by 13%) scatter in gas fraction, (2) a negative correlation between depletion time scale and stellar mass (at almost fixed sSFR and redshift), and (3) a high value of $V/\sigma \simeq 10$ for one of two disk galaxies. We need to investigate such trends with a large sample of galaxies as well as with higher angular resolution imaging.

Contents

Acknowledgments

I WOULD LIKE TO EXPRESS MY FIRST AND SINCERE GRATITUDE to my supervisor Dr. Ryohei Kawabe who supported me from various aspects and encouraged me to push through the difficult moments when I felt like quitting during the journey of PhD. I also learned invaluable lessons about observational astronomy from him and the attitude toward the nature during the last five years that I am always impressed by his keen insights and diverse interests on astrophysical phenomena.

The realization of this dissertation has been possible thanks to the additional moral support and help of a large number of people, including my family, friends and colleagues. I appreciate my family members, my parents, Jangreal Lee and Youngnam Bae, my little sister, Minji Lee, and my grandmother, Jungja Kim, for their supports far from Japan in South Korea, so that I could pursue my dream of studying astronomy without thinking of any obstacles that might have been. It has been ten years after I came to Japan, where I spent all of my 20s, and enjoying life in Japan is indeed benefitted by learning how to speak Japanese fluently after taking Japanese classes in the Kagoshima University and by having invaluable friendship with my Japanese older sister or my first and the last tutor, Dr. Mizuno Izumi. Struggling in hard times during the past five years, I could visit her house twice in Hilo and she always welcomed me in delight and with humors.

My special thank should be expressed for my collaborators including Drs. Ichi Tanaka, Tadayuki Kodama and Kenichi Tadaki, and all the people in the MAHALO survey team. They were irreplaceable scientific mentors by letting me to deal with the Subaru data sets and they were always welcomed me for the discussions on the interpretation of ALMA and Subaru data sets. The rich ALMA data sets would not have been obtained without their pioneering works by the narrow-band filter technique and by establishing unique samples.

I am indebted to Dr. Kotaro Kohno and his former student Dr. Kenta Suzuki, since they let me analyze the JVLA and ALMA data sets by their courtesies. Further, the former and current lab members of Dr. Kohno Kotaro including himself were really supportive by inviting me for many seminars to get more insight toward SMGs, AGNs and local galaxies, which I really thank for their hospitality.

I cannot forget to express my deep gratitude for all the people (who were and are) in the ALMA building, the EA ARC members and students. I ask to forgive to choose not to spell out all of people except two, Dr. Daisuke Iono and the past member of Kawabe-lab, Dr. Toshiki Saito. I express my deep gratitude all the other people even though they are not listed in specific. They helped me to solve issues related to all the processes starting from the preparation of the proposal to the delivery of the data and the technical discussions to finally get the scientifically meaningful data sets. I thank all the JAO members in Chile for their efforts for the smooth ALMA operations to get the ALMA data sets in the best quality. I appreciate all of my co-authors who are not mentioned above, who took their own responsibility of the published paper and the works in preparation by deliberative discussions : Drs. Masaru Kajisawa, Min S. Yun, Kouichiro Nakanishi, Yoichi Tamura, Bunyo Hatsukade, Hideki Umehata, Takuma Izumi, Itziar Aretxaga, Milagros Zeballos, Soh Ikarashi, Grant W. Wilson, David H. Hughes, and Rob. J. Ivison.

I thank all the Korean researchers and their family members for their dearest friendship for letting me get relaxed during lunch, tea breaks or dinner, people including Jung-sook Kim, Kyoung-sun Lee, Dong-wook Song, Heran Jung, and Jungha Kim. I would like to thank my fellow Astronomy graduate students for being friendly in any unscheduled visits of myself.

Finally, I thank the official reviewers of this dissertation, Drs. Mamoru Doi, Nobunari Kashikawa, Toshitaka Kajino, Kentaro Motohara, and Noki Yoshida for timely reading and useful criticism.

Minju Lee

Listing of figures

Listing of tables

Somewhere, something incredible is waiting to be known.

Carl Sagan

Chapter 1

Introduction

Preface

ASTRONOMY STANDS AS THE OLDEST NATURAL SCIENCE THAT DATES BACK TO ANTIQUITY. The behavior and the beauty of the sky have always tempted the human being to learn about what makes the world the way it is. While the tools including telescopes and supercomputers have been sophisticated and enlarged in the modern astronomy, we pursue similar desires of ancient people to demystify the nature of the universe.

Our current knowledge is mostly on only 5% of the composition of the Universe (Planck Collaboration et al. 2016). It is the baryonic matter that we could be able to 'see' so far and therefore, vital to expand our grasp of the Universe. In this dissertation, we investigate key underlying questions related to galaxies that are composed of baryonic matter, with hopes to address the concept of galaxy evolution in the distant universe within the larger scale structures.

We present the Introduction with a contextual summary of the former related studies on galaxy formation and evolution. The first section provides observational and the theoretical foundations of hierarchical structural formation and the following section describes observational challenges and successful methods to study high redshift (proto)clusters. Next, several important scaling relations between observables are reviewed, which include the correlations between global gas content ($M_{\rm gas}$), star formation rate (SFR), stellar mass ($M_\star$) and galaxy size. Finally, we invoke an important paradigm to probe galaxy evolution, i.e., environment (nurture) versus mass (nurture) and present the parameter spaces that are addressed within the Dissertation.

1.1 Formation of the cosmic web

1.1.1 Cosmological context : first stars and galaxies

The concordance model for cosmology is ΛCDM (Λ cold dark matter)[*]. It has been established based on the detailed observations of the cosmic microwave background (CMB, Planck Collaboration et al. 2016) with a joint analysis of type Ia supernovae (SNe Ia) (Riess et al. 1998; Perlmutter et al. 1999) and baryonic acoustic oscillation (BAO). The precise determination of the cosmological parameters allows us to know the geometrical curvature as well as the mass and energy budget of the Universe. The total (mass-)energy of the Universe consists of three main components : baryons, cold dark matter and dark energy. Only a small fraction of the total budget is associated to baryons, which is at most five per cent. Baryons indicate all ordinary matters in astronomy that are 'visible' including protons, neutrons and leptons. Cold dark matter compose about a third of the budget, i.e., $\sim$ 27 %, which is a form of matter to account for gravitational effects. It is inferred to exist from the observations of rotation curves of galaxies, gravitational lensing of galaxy clusters, enhanced clustering of galaxies, and to explain BAO. Dark energy is the other form of "matter", which consists of the 69% of the total energy budget, to explain the accelerated expanding universe.

In the ΛCDM model, the Universe was in a very hot and dense state after the Big Bang 13.8 Gyr ago. The temperature was so high that all the matters were ionized and suffered many Thomson-scattering collisions with electrons. With the expansion, the Universe was eventually cooled down. The density also decreased enough, so that it was possible to propagate the radiative information of the recombination between electrons and protons (mostly Hydrogen and Helium). This is the CMB, the 'surface of last scattering' that occurred at $z \sim 1100$, or $380,000$ years after the Big Bang. The CMB looked very homogeneous but turned out to have tiny fluctuations.

The primeval perturbations grew and became the seeds of the first structures in the universe. It gave rise to the formation of the Large-scale structure (LSS) that we observe now (Figure 1.1). The structural growth is at first mainly driven by collisionless cold dark matter to increase its density under the effect of inexorable attraction of gravity. The growth of dark matter proceeds hierarchically. The Jeans mass (Jeans 1902), just after the time of recombination (or decoupling

---

[*] Recently, a tension for the Hubble constant, H_0, was reported between the Planck observations and the local measurements, where the difference is larger than 3σ (e.g., Riess et al. [2016]). While it is tempting, the subject needs to be tested in more details, which is not our main consideration. Hence, we regard the ΛCDM as the concordance model.

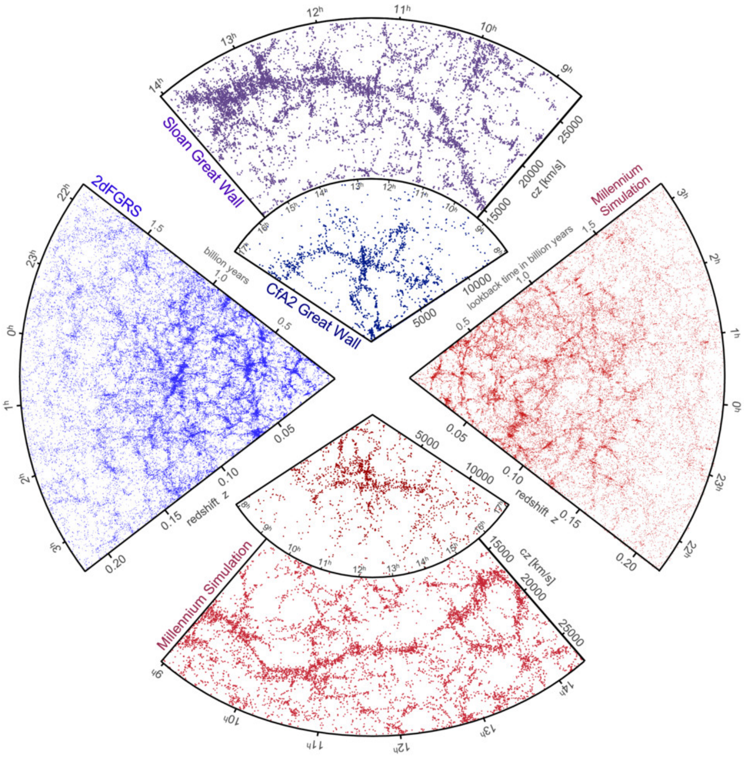

Figure 1.1: The Large-scale structure that is observed (blue and purple) and simulated (red). Taken from Springel et al. [2006]

of matter from photon), was an order of $10^5\ h^{-1}\ \mathrm{M}_{\odot}$, which is close to the mass of globular clusters or dwarf galaxies. The mass scales above the value become unstable and collapse. The concentrated structures of dark matter after the collapse keep growing by mass accretion from outer regions and they merge into a complex network of dark matter, well before baryons (Gunn & Gott 1972). Gas then cools down and decouples from dark matter. The complex star-forming processes start and finally these first stars gather to form first galaxies.

1.1.2 Protoclusters and clusters

The build-up of larger structures further proceeds. Clusters and other large structures including filaments, sheets and walls, are formed via mergers of many smaller haloes. All of these large scale structures have vague boarders and are all continuously linked.

Although the number density of present-day massive clusters is small (e.g., Bahcall & Cen [1993]), the studies of clusters and its progenitors, protoclusters, provide critical constraints on both cosmological (e.g., Allen et al. [2011] for a recent review) and galaxy formation model.

Hereafter, we refer to a progenitor of clusters[†] as a protocluster[‡].

In particular, the formation of massive elliptical galaxies can be investigated by probing protoclusters at high redshifts. Blumenthal et al. [1984] suggested that the formation of the galaxies would be different according to their environment. In moderate dense regions, disk galaxies are formed by angular momentum conservation during the collapse (e.g., Mo et al. [1998]). In denser regions, elliptical galaxies are formed by multiple mergers. As such, we expect to witness the formation of elliptical galaxies in high redshift overdense regions and the merger-driven formation scenario should be tested by observations.

There is a lack of observational studies on the very early stages of galaxy cluster formation before virialization and on the galaxy evolution during that time. Theoretical studies and simulations have provided rather a clear picture that needs to be tested with observations : at $z \sim 10$, star forming activities within the protoclusters could contribute to $\sim 50\%$ of the cosmic star formation rate density (CSFRD), in contrast to the contribution of local clusters which is negligible ($\sim 1\%$) (Chiang et al. [2017]); at $z \sim 1-4$, the protoclusters begin to virialize and transform into a typical massive cluster, and more than a half of the total stellar mass contained in present-day clusters is assembled during the period (e.g., Chiang et al. [2013, 2017]). We note that the later epoch between $z = 1$ and $z = 3$ (the “target” epoch of this dissertation) is also crucial for understanding the assembly of massive galaxies as a whole (e.g., Madau & Dickinson [2014]).

Difficulties in identifying protoclusters

The observational studies of protoclusters are more difficult and complex, because we have insufficient information to trace the formation and the evolution of both such large structures and galaxies inside them. Here, we list various aspects that have caused the lack of observational studies toward protoclusters.

- The rarity of massive (enough) haloes : considering the hierarchical formation, the halo mass above 10^{13} $M_\odot$ is rare at $z > 2$. Instead, a modest overdensity is often used as a probe for protoclusters, which might increase the chance of misidentification of other large-scale structures such as filaments.

[†] Here, we define a galaxy cluster that is with halo mass above 10^{14} $M_\odot$.

[‡] But it is important to understand that the definition of protocluster is only practical in theory and simulations. See the difficulties in defining a protocluster presented in the next page.

- Limited survey volume to constrain the evolution of overdense regions: the expected size of protoclusters at such high redshift is extremely large that extends over a few hundred comoving Mpc (Chiang et al. [2013]). Therefore, it would be difficult to pick out a proper density contrast in a probed volume that is, in general, too small in the up-to-date large surveys. Besides, it is difficult to confirm whether even a moderate density region, which is probed in a limited volume, is a genuine progenitor of clusters or a dense structure that can be other, e.g., filaments, the similar concern as the previous item.
- Difficulties in halo mass measurement : although the halo mass of a protocluster can be used as one of the tracers to infer the evolutionary stage and descendants of the protocluster, the mass itself is hard to measure, since the protocluster may not be dynamically stable and have undefinable morphology (i.e., not spherical); by the nature of the definition, a protocluster is not virialized yet and still in a merging phase of smaller dark matter halos. Therefore, extrapolating the evolution with the observed overdensity should be taken cautiously.

Provided these obstacles, we may need to accept the limitations of what we can do now, and at the same time, observational strategies need to be improved by the inputs from theories and simulations.

Methods to find protoclusters

Virialized clusters have been identified by finding hot, gaseous components around the cluster, using X-ray or inverse-Compton scattering of CMB photons, the Sneav-Zeldovich (SZ) effect, or by probing a large volume in optical/NIR wavelengths using color selection to find red-sequence galaxies. However, finding a protocluster is more difficult because the infant system is less likely to have hot gas or to show enough density contrasts of galaxies, which is another method of searching low-z (virialized) clusters. As mentioned previously, the methods for searching protoclusters are basically finding the moderate density peaks. We list in the below the searching methods that have been successful for searching high-z ($z > 2$) protoclusters.

- Serendipitous detections and large surveys : as by-products of large spectroscopic surveys, several protoclusters have been found. The discoveries include the identification of one of the largest structures located at $z = 3.09$, the protocluster SSA22 (Steidel et al. [1998]). The combination of pre-selecting overdense regions from a large field survey and performing follow-up observations for the spectroscopical redshift confirmation is another way to go faster to find overdense structures (e.g., Shimasaku et al. [2003]; Ouchi et al. [2005]; Toshikawa et al. [2012]; Chiang et al. [2014]). A large number of candidate protoclsuters are also found by Herschel and Planck telescopes, though the candidates need spectroscopic confirmation (Clements et al. [2014]; Planck Collaboration et al. [2015]).

- Using radio galaxies, QSOs and submillimeter-bright galaxies (SMGs) as biased tracers : finding overdense regions around massive populations has been one of the popular methods to find protoclusters. Massive galaxies often indicate a signature of enhanced blackhole accretion and/or star forming activities, which include radio galaxies, QSOs and SMGs. Finding protoclusters around radio galaxies has been quite successful (e.g., Pascarelle et al. [1996]; Le Fevre et al. [1996]; Kurk et al. [2000]; Venemans et al. [2002]; Best et al. [2003]; Venemans et al. [2004, 2007]; Hatch et al. [2011]; Hayashi et al. [2012]; Cooke et al. [2014]). The hosts of radio galaxies are expected to be the most massive galaxies (Seymour et al. [2007]) and are expected to be embedded in the most massive halos (e.g., Rocca-Volmerange et al. [2004]; Orsi et al. [2016]). On the other hand, the success rates in searching protoclusters around QSOs or SMGs have depended on the redshifts and/or the spatial resolutions, e.g., Djorgovski et al. [2003]; De Breuck et al. [2004]; Kashikawa et al. [2007]; Matsuda et al. [2011]; Umehata et al. [2014]; Smail et al. [2014]; Miller et al. [2015]).

- Gas absorption technique : another way to probe the density of the universe is using the absorption lines by probing QSOs as background sources (e.g., Frye et al. [2008]; Matsuda et al. [2010]; Lee et al. [2014]; Chiang et al. [2015]). The method is based on the idea that overdense regions at high redshift should have a large amount of cold or warm, dense gas (Cai et al. [2016]).

With the presented methods, the number of identified protoclusters is increasing. The next step is to investigate the individual galaxies associated to those protoclusters, though such studies have not been carried out extensively. This dissertation focusses on a protocluster “4C23.56”, which is found around the high-z radio galaxy 4C23.56. We specifically investigate Hα emitting galaxies (HAEs) associated to the protoclsuter, which are detected by the narrow-band (NB) filter technique to trace the star forming galaxies. The narrow band filter technique can effectively choose a line emitting galaxy in a relatively secure redshift range defined by the width of the NB filter ($\Delta z \sim$ 0.03 for our case)

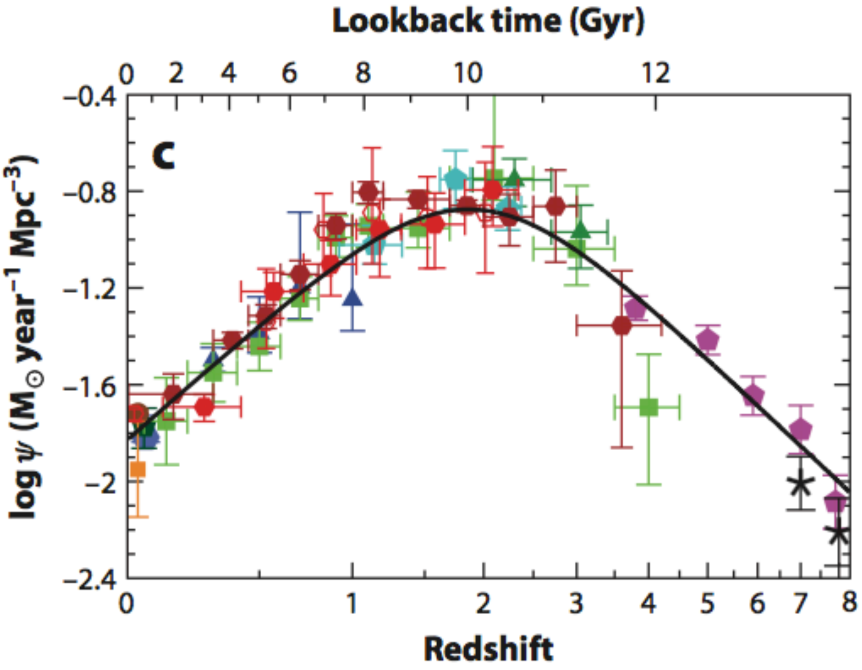

Figure 1.2: Cosmic evolution of star forming activity. Taken from Madau & Dickinson [2014]

1.2 Cosmic star formation history and scaling relation

1.2.1 Gas content and star formation

The peak of star formation in the Universe is found at redshift between 1 and 3 (e.g., Madau et al. [1996]; Madau & Dickinson [2014], Figure 1.2). By $z = 1$, about a half of the stellar mass of the Universe is assembled (e.g. Bundy et al. [2005]; Mortlock et al. [2011]).

In investigating the assembly of cosmic stellar mass by star formation, it is important to probe the fuel of star formation, i.e., cold gas. During the last several years, intensive surveys at FIR-to-mm wavelengths have been conducted to probe the global (within the galactic scale of < 10 kpc) gas content ($M_{\rm gas}$) for a large number of star forming galaxies in both the local and the high redshift universe (e.g., Scoville et al. [2013]; Saintonge et al. [2013]; Santini et al. [2014]; Genzel et al. [2015]; Decarli et al. [2016a]; Schinnerer et al. [2016]; Tacconi et al. [2017]; Scoville et al. [2017]). The measurements of gas content have been done with either low-J CO lines or dust continuum with a suitable conversion to probe the total cold gas (which is mainly composed of H_2 and He). Such observations have confirmed that the evolution of the cosmic star formation is closely connected to the evolution of available gas content (Figure 1.3), which is the sum of the gas that has been accreted and consumed. Feedbacks from the newly formed stars and the black

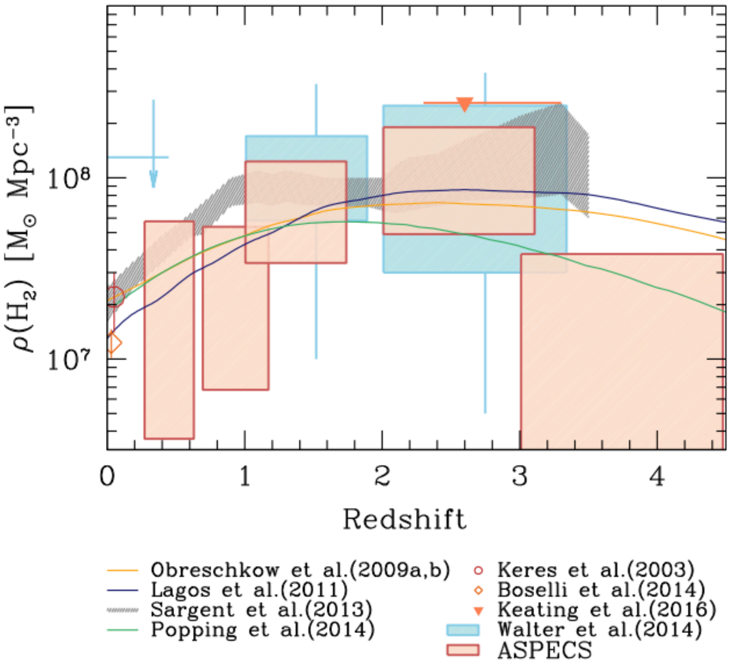

Figure 1.3: Cosmic evolution of total gas mass. Taken from Decarli et al. [2016a].

hole accretion may regulate the available gas.

In understanding the star-formation activity and the regulation of gas content, an empirical relation is often investigated between the observed star formation rate (or star formation rate density) and the gas content (or gas density) (Kennicutt [1998b]). The ratio between the gas mass and the star formation rate is a probe of the depletion time scale of the observed gas content ($\tau_{\rm depl.} = M_{\rm gas}/{\rm SFR}$). The inverse of the depletion time scale is a probe of star formation efficiency (SFE $=1/\tau_{\rm depl.}$ for extragalactic survey in general, while a slightly different definition for SFE is used for a resolved structure, $\Sigma M_{\rm gas}/\Sigma{\rm SFR}$).

By investigating the time evolution of the empirical scaling relation of gas mass–SFR, the cosmic star formation seen at $z = 1 - 3$, which is found to be more active than that of the local universe, can be dominantly explained by the higher gas fraction ($f_{\rm gas} = M_{\rm gas}/(M_{\rm gas} + M_\star)$), rather than high SFE, at least for the typical star forming galaxies (on the main sequence[§]); both SFE and $f_{\rm gas}$ are increasing toward (at least) $z \sim 3$ from $z = 0$, but SFE evolves rather smoothly than $f_{\rm gas}$ on the main sequence. This implies that the star forming activity of the main-sequence galaxies is similar to that occurs in the present-day (e.g., Genzel et al. [2015]; Schinnerer et al. [2016], Figure 1.4 for the evolution of the depletion time scale). Also, the observed high val-

---

[§] A brief introduction on the description of galaxy main-sequence can be found in the next Section 1.2.2

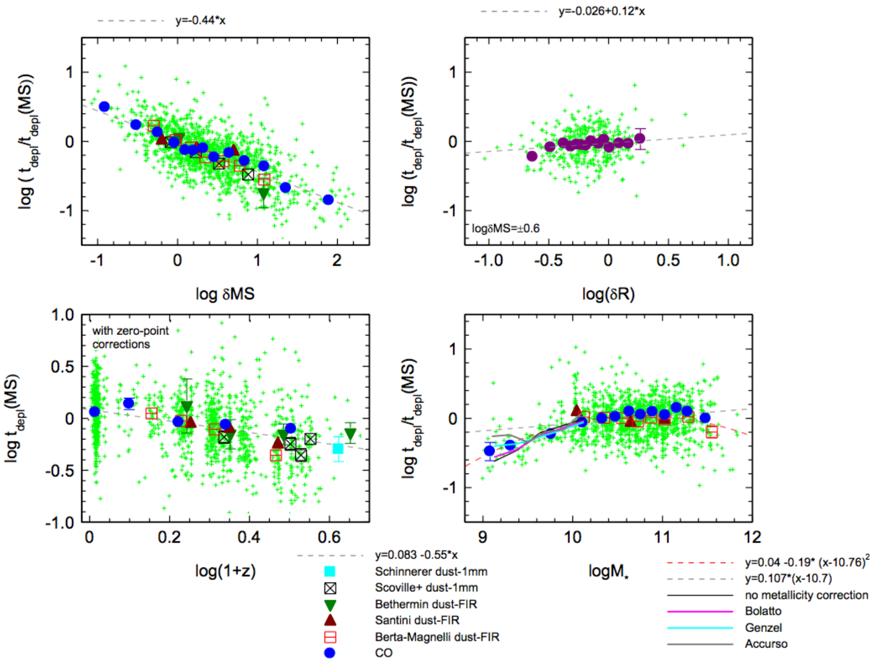

Figure 1.4: Cosmic evolution of depletion time scale for typically star forming, i.e., main sequence galaxies. And its relation to deviation from the main sequence (δ MS), size ($\delta\,R$) and mass ($\delta\,M_\star$). Taken from Tacconi et al. [2017].

ues of $f_{\rm gas}$ and $M_{\rm gas}$ appear to mimic the high gas supply rate at high redshift (e.g., Tacconi et al. [2013]; Magdis et al. [2012]; Saintonge et al. [2013]; Sargent et al. [2014]; Genzel et al. [2015]; Scoville et al. [2014, 2016]; Schinnerer et al. [2016]). As such, current gas measurements describe the galaxy evolution well in the volume “averaged” view, i.e., in the general fields, at least up to $z \sim 3$.

Since galaxies evolve not only as a function of redshift, but also of the their environment, one needs to understand how the gas content and its fraction change with the environment, from fields to groups to clusters. Almost no gas measurements have been reported for the typical star forming galaxies that are associated to overdense regions at high redshift, until this year[¶]. Main reasons of the lack of the observations are owing to the difficulties in the identification in the first order as illustrated in the previous section. The existing observations have been on one or two samples of starbursts[‖] (i.e., well above the main sequence $>$ 0.6 dex) (e.g., Riechers et al.

[¶] Almost at the same time of this year, several papers are published related to the gas measurements or detections for protocluster galaxies on the main sequence, including the work presented Chapter 3 e.g., Noble et al. [2017]; Hayashi et al. [2017].

[‖] We hereafter use the term ”starburst” to refer to a galaxy well above the main sequence (>0.6 dex), which may include *classical* SMGs (i.e., S(850 μm)>5 mJy) as a sub-population. To be clear, the term SMGs indicates galaxies generally detected with a submm single dish, which are in most cases unresolved. We explicitly use the term “main-sequence SMGs” when these galaxies are, once resolved, on the main

[2010]; Tadaki et al. [2014]) and the active galactic nuclei (AGNs) (e.g., Emonts et al. [2013]) per system, which do not represent the whole population in protoclusters; these populations are rare. Therefore, we need to investigate the typical population on the galaxy main sequence which dominates the total number. Studying the gas content of galaxies in different environments would provide crucial information on how galaxy evolution can affect or can be affected by the surrounding environment during star formation and during the collapse and the merging of halos to form clusters. With this motivation, Chapter 3 reports one of the first gas measurements for high redshift overdense regions, and which is the highest redshift till now as one of the systematic surveys.

1.2.2 The star formation main sequence

Another scaling relation related to star formation rate is a correlation between SFR and stellar mass. It is often referred to the main sequence of star forming galaxies (e.g., Bell et al. [2005]; Elbaz et al. [2007]; Noeske et al. [2007]; Daddi et al. [2007]; Santini et al. [2009]; Whitaker et al. [2012, 2014]; Speagle et al. [2014]). The correlation between two observables is very tight within $\sim$ 0.3 dex and the power of the scaling relation is less than one, i.e., sub-linear. Provided these, the origin of the star-forming sequence is often referred to a balance between the gas accretion and outflow i.e., secular processes (e.g., White & Frenk [1991]; Mo et al. [1998]).

The correlation evolves as a function of time. The specific star formation rate at given stellar mass has evolved by a factor 20 from $z \sim 2$ to the present time. This means that the star formation rate for massive star forming galaxies $M_\star > 10^{10.5}$ $\mathrm{M}_\odot$ at $z \sim 2$ is in excess of 100 $\mathrm{M}_\odot\,\mathrm{yr}^{-1}$ (e.g., Shapley et al. [2003]; Daddi et al. [2007]). In local universe, such elevated SFRs are mostly driven by mergers and often associated with starbursts. As opposed to the local expectation, the high SFR at given mass is thought to be mainly produced by continuous mass-dependent processes that declines gradually with time. Light profiles from the HST (e.g, Wuyts et al. [2011]), recent IFU observations and spectroscopic data support this idea that the morphologies and the kinematic structures explain that the galaxies' star forming activities are occurred within a disk-like component, rather than by a merger (Fig 1.5, 1.6, 1.7, and 1.8).

A notable observational fact in the kinematic properties of the high redshift star forming galax-

---

sequence (with smaller flux densities). Recent higher-resolution follow-up observations with ALMA demonstrate that such classical SMGs are in fact a mixture of starbursts and the main sequence galaxies, when they are resolved and plotted on the plane of SFR-$M_\star$ (da Cunha et al. [2015]).

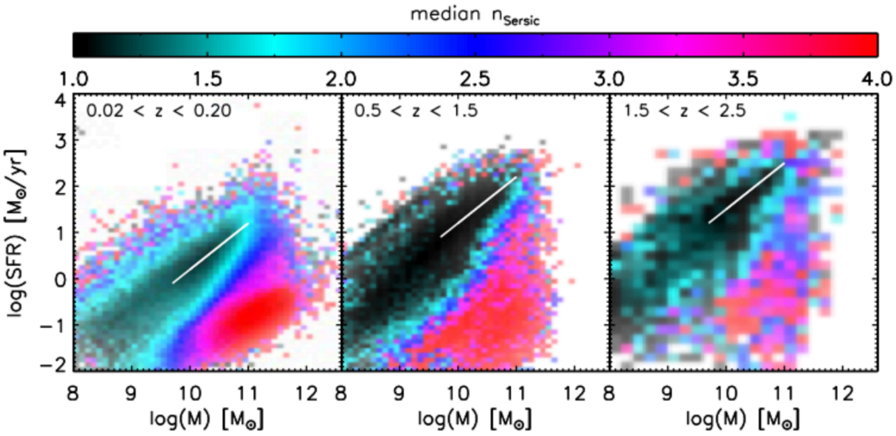

Figure 1.5: The evolution of the star forming galaxies and Sérsic profile. Taken from Wuyts et al. [2011]

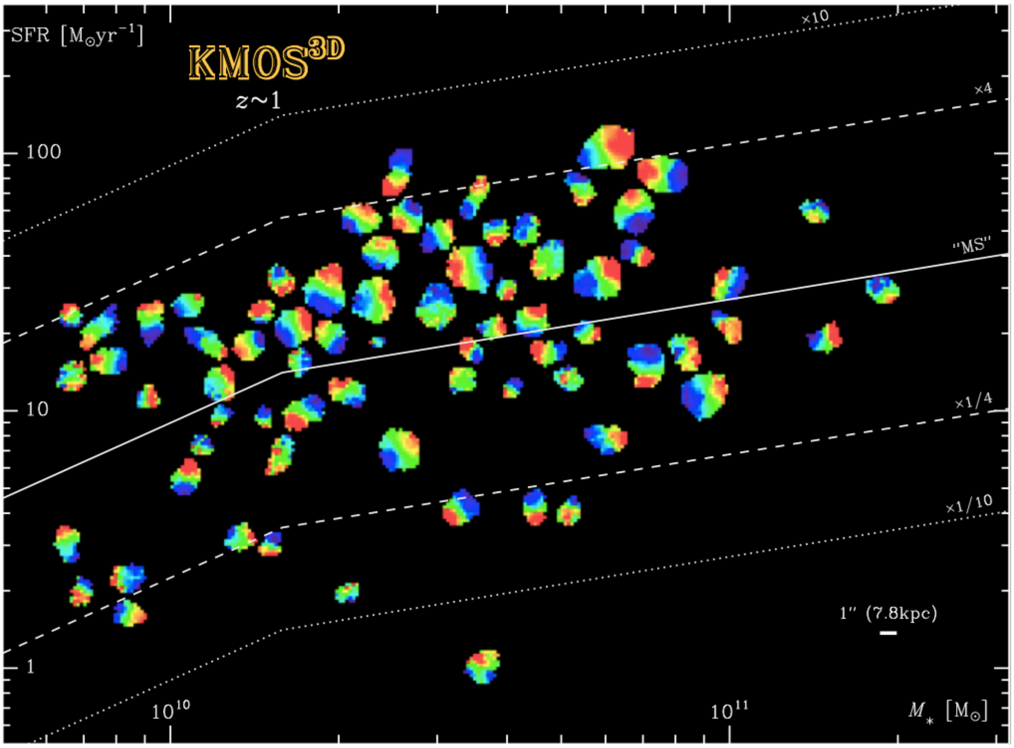

Figure 1.6: Plot of velocity fields for High redshift galaxies at $z \sim 1$ in SFR vs M* diagram that shows disk rotation rather merger features, from the KMOS^{3D} survey. Taken from Wisnioski et al. [2015]

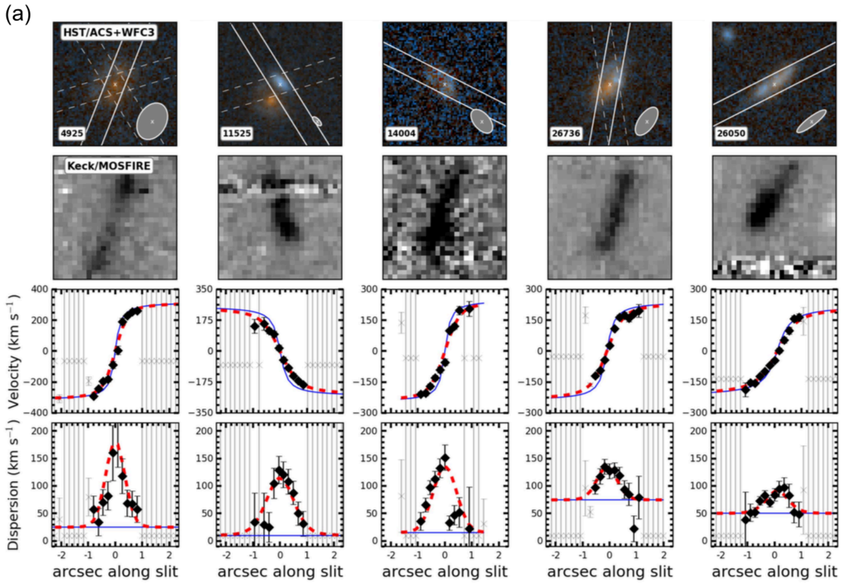

Figure 1.7: High redshift galaxies at $z \sim 2$ that show disk rotation rather merger features, from Survey in the near-Infrared of Galaxies with Multiple position Angles (SIGMA). Taken from Simons et al. [2016]

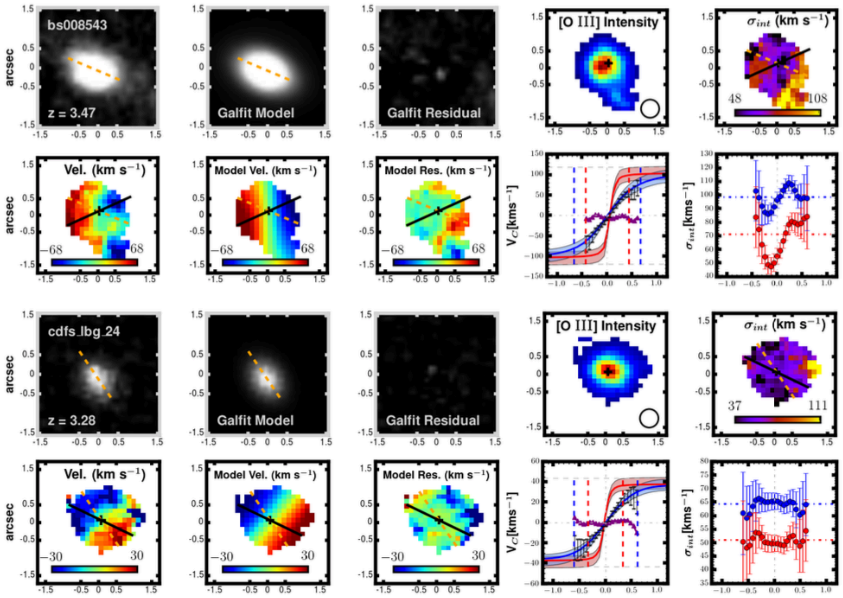

Figure 1.8: High redshift galaxies at $z \sim 3.5$ that show disk rotation, from the KMOS Deep Survey (KDS). Taken from Turner et al. [2017b]

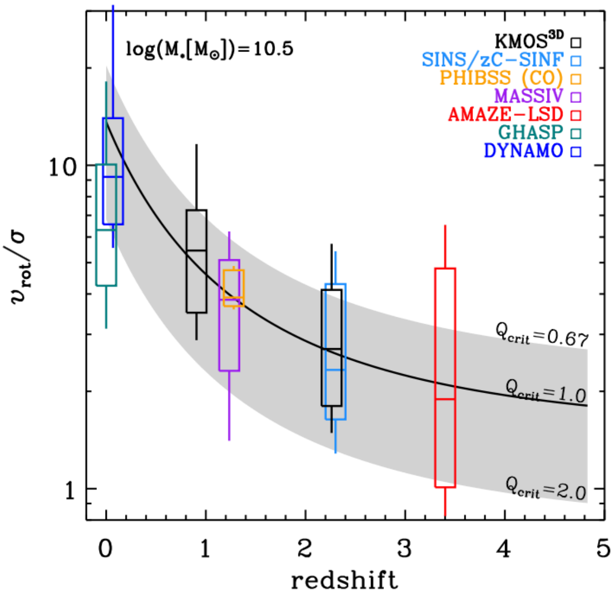

Figure 1.9: The evolution of $V_{\rm rot}/\sigma_0$ as a function of redshift. Taken from Wisnioski et al. [2015]

ies is that the galaxies are significantly supported by pressure rather than a rotation (e.g., Flores et al. [2006]; Weiner et al. [2006]; Kassin et al. [2007]; Förster Schreiber et al. [2006, 2009, 2011]; Gnerucci et al. [2011]; Kassin et al. [2012]; Epinat et al. [2012]; Magdis et al. [2016]; Wisnioski et al. [2015]; Simons et al. [2016, 2017]; Turner et al. [2017b], Fig 1.9). Also, the evolution of the relative role of rotation to turbulence (or pressure), which are traced by the rational velocity, $V_{\rm rot}$, and intrinsic velocity dispersion, σ_0, respectively, is well explained by the evolution of gas fraction (e.g., Wisnioski et al. [2015]); the shaded area and the solid line in Fig 1.9 show the expected $V_{\rm rot}/\sigma_0$ evolution by considering the evolution of gas fraction and several Toomre Q parameters of a disk, i.e., a marginally stable disk with $Q = 1$ shown as the solid line, and the shaded area for the range of $Q = [0.67, 2.0]$. Again, these are findings for the field population.

How about the galaxies in denser regions? Surveys to probe the kinematic properties of galaxies have also been carried out mostly for field population, and not for protocluster main sequence galaxies. Probing kinematic properties of (proto)cluster galaxies can provide the information regarding how similarly or differently cluster populations are formed. As it will be addressed in Sec 1.4.1, local clusters are often dominated by the early-type galaxies (ETGs), while general fields are dominated by spiral galaxies, or the late-type galaxies (LTGs) (e.g. Dressler [1980]).

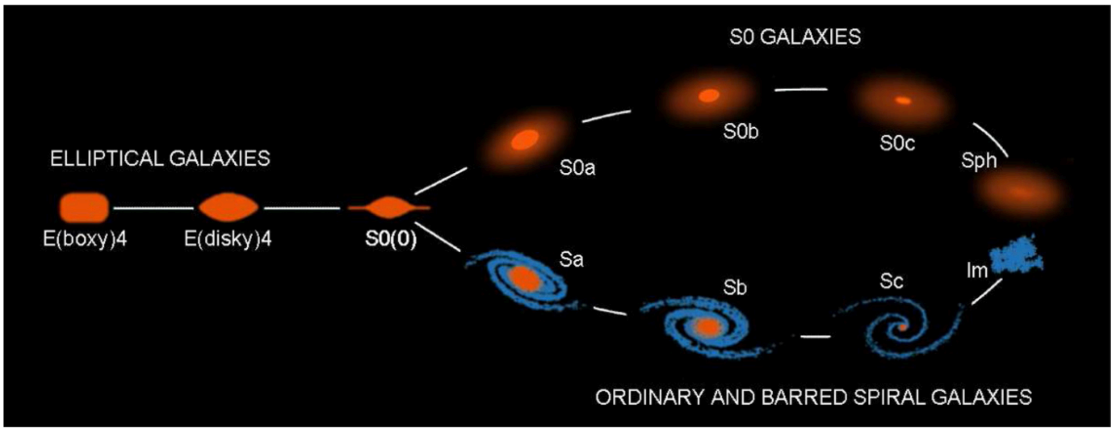

Figure 1.10: Modern view of the Hubble sequence. Taken from Kormendy & Ho [2013]

1.3 Morphological classification of galaxies : the Hubble sequence

As early as the work of Hubble [1926, 1936], the galaxy morphology is one of the fundamental parameters that classify galaxy populations (Fig 1.10). In Hubble's tuning fork (or the Hubble sequence), elliptical galaxies are spheroidal systems which are supported by the random motions of the stars. Spiral galaxies on the other side are composed of a rotation-supported disk and a central spheroidal bulge component. We find S0, or lenticular, galaxies in the middle of the Hubble sequence. Further refinements to this classification have included irregular galaxies (e.g. Kormendy & Ho [2013]). The Hubble Sequence seems to be existing up to $z \sim 2$ (e.g., Wuyts et al. [2011]).

Despite the long history of the Hubble sequence, the origin of the Hubble sequence remains one of the key unresolved questions in astronomy; the physical mechanism that shapes galaxies differently is still unconstrained. In a recent decade, however, new information on the physical properties of galaxies is increasing and allows us to revisit the problem deeper than ever.

1.3.1 Size

The size of galaxy is one of the quantitative measures for galaxy morphology. Furthermore, the size can be used to infer the build-up of angular momentum in galaxies. In the framework of the ΛCDM model, a disk galaxy (or morphologically spiral in most cases) is formed by the conservation of angular momentum (e.g., Mo et al. [1998]), after the pristine gas has fallen, and is shocked and cooled through radiative processes. On the other hand, the formation of ellip-

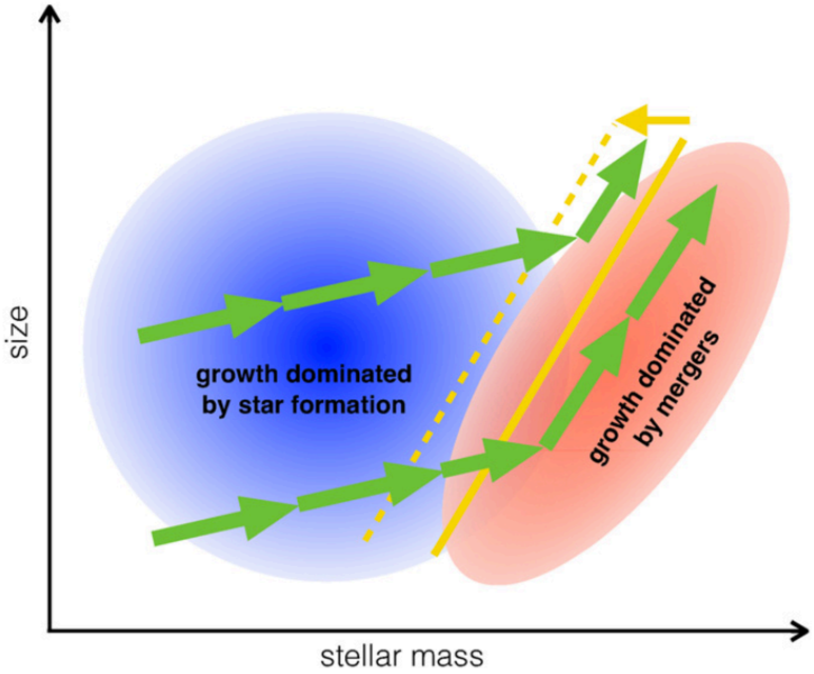

Figure 1.11: The evolution of size along the mass. Taken from van Dokkum et al. [2015]

tical galaxies is accompanied by the intensive star forming activity that is driven by mergers. During the course of mergers, the angular momentum of galaxies is dissipated efficiently (e.g., Toomre & Toomre [1972]; Toomre [1977]). From such point-of-view, the size provides information on the halo properties and the transferred amount of angular momentum from dark matter to baryons, and hence, it helps us to understand the origin of the Hubble sequence.

Galaxies experience several internal and external processes in the course of their evolution, and this produces another empirical relation, the relation between the galaxy size and its stellar mass (hereafter, the mass-size relation, Fig 1.11). The mass-size relation has been used to infer different evolutionary histories of galaxies. The size evolution of galaxies, at least on the massive end, is affected by the recent accretion of gas, which is accompanied by the star formation and the occurrence of mergers (e.g., Buitrago et al. [2008]; van Dokkum et al. [2010, 2015], see Fig 1.11); (massive) galaxies have larger sizes that have experienced recent gas accretion and mergers.

Light distribution of galaxies

Here, we give a description of the radial light profile in a galaxy in order to argue the properties of the galactic structure and the size. The light distribution in elliptical galaxies is often explained by the de Vaucouleurs's profile (de Vaucouleurs [1948]), which is expressed as follows.

$$\log_e[\frac{I(r)}{I(r_e)}] = -7.6692[(\frac{r}{r_e})^{1/4} - 1] \tag{1.1}$$

The light profile of disk galaxies can be expressed by

$$I(r) = I_0 \exp{(-r/h)}, \tag{1.2}$$

where h is called a disk scale length (Freeman [1970]).

These two profiles are generally combined to the Sersic profile (Sersic [1968]) parameterized with the Sérsic index, n, and the effective radius, r_e, which is expressed by

$$\log_{10}[\frac{I(r)}{I(r_e)}] = -b_n[(\frac{r}{r_e})^{\frac{1}{n}} - 1], \tag{1.3}$$

n=4 is for the de Vaucouleurs' $r^{1/4}$ law and n=1 for the exponential profile of a disk. In the course of mass assembly, the Sérsic index of galaxies changes mostly from n=1 to n=4; blue (young) star-forming galaxies on the main sequence are mostly disk-dominated galaxies with n=1, while red and quiescent galaxies are explained as bulge-dominated galaxies with n=4 (e.g, Wuyts et al. [2011], Fig 1.5). Therefore, both the Sérsic index itself as one of key structural parameters and star forming activity are necessary to understand the origin of the Hubble sequence.

1.4 Galaxy quenching and its origin

Two main agents, i.e., environment and galaxy mass, are often considered as the drivers of galaxy evolution and quenching, phenomenologically. The concept to explain the individual and the relative roles of the agents is often referred as 'nature (mass)' or 'nurture (environment)' paradigm. Understanding the physical ground for the paradigm is important to investigate galaxy evolution in different environments. It seems that the roles of mass and environment are independently separated up to $z \sim 1$ (Peng et al. [2010], see also Weigel et al. [2017] for a minor role for merger quenching). In the following sections, we review these two aspects about galaxy quenching.

1.4.1 Environmental process : nurture

The dependence of galaxy properties on their environment has been studied for four decades (e.g., Oemler [1974]; Davis & Geller [1976]; Dressler [1980]). For example, the relative fraction of different morphological types of galaxies changes with environment and the observational fact is called as the morphology - density relation (Dressler [1980]). The fractions of elliptical and S0 galaxies (i.e., early-type galaxies) are increasing with increasing local density, while the spirals dominate the low-density environments (Fig 1.12).

Kinematically, early-type galaxies are subcategorized by two types; i.e., slow rotators (SRs) and fast rotators (FRs). Slow rotators are less rotation-dominated systems with small ellipticity, i.e., a rounder structure, while fast rotators have ranges of the ellipticity with dominant rotating component.

Less than a half of the early type galaxies are SRs, and the fraction of SRs seems to rapidly increase in the densest regions (e.g., Cappellari [2013]; D'Eugenio et al. [2013]; Scott et al. [2014]). On the other hand, the fraction of the FRs is *gradually* increasing toward denser regions. Such trend, which we call as the kinematic morphology-density relation, is similar to the classical morphology-density relation; the number of elliptical galaxies grows in the densest region (like SRs) and that the fraction of S0s gradually increases toward the denser regions (like FRs). The morphology– and the kinematic morphology–density relations imply different formation mechanisms to form SRs (elliptical galaxies) and FRs (S0), though the observational studies need further investigation.

Finally, we summarize the physical mechanisms under which morphologies and kinematical

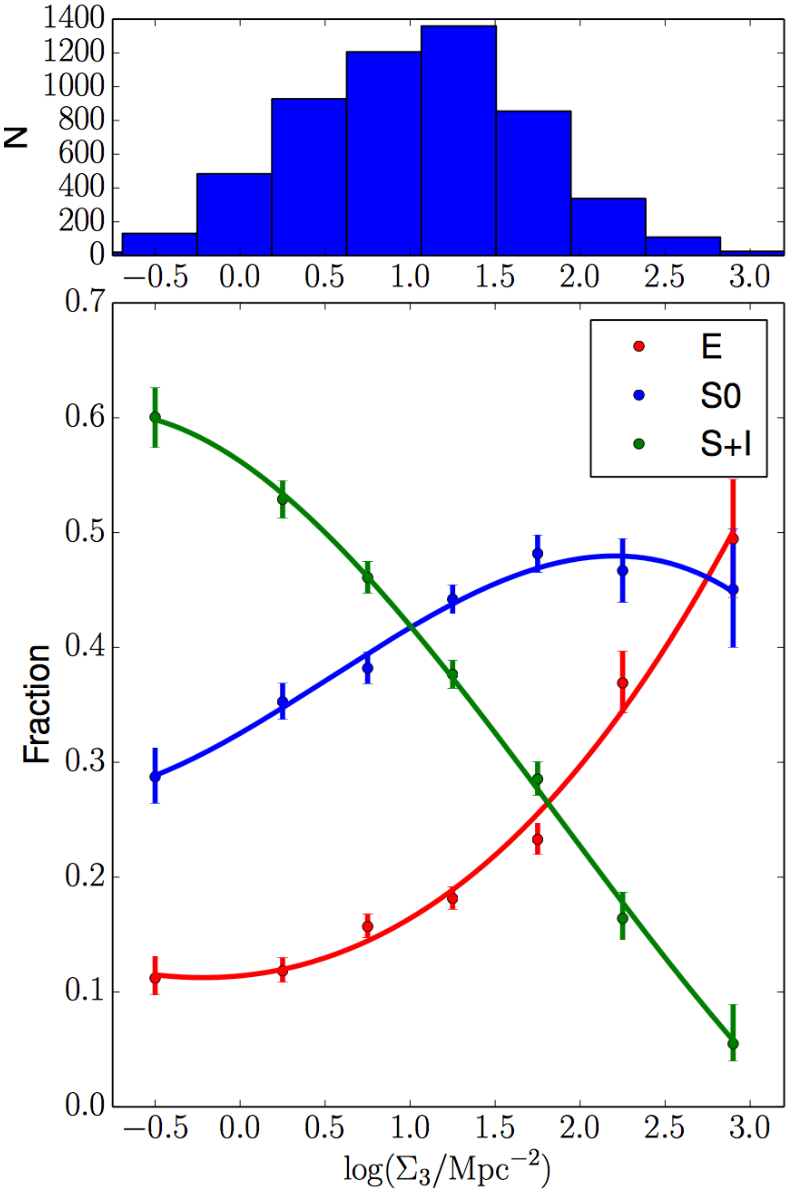

Figure 1.12: The revised version of morphology–density using up-to-date information, e.g., redshift, local density, completeness, which is 'qualitatively' similar to findings four decades ago. Further discussions are provided within Houghton [2015] from which this figure is also taken. E stands for elliptical, S0 for lenticular galaxies and S+I for spiral and irregular galaxies.

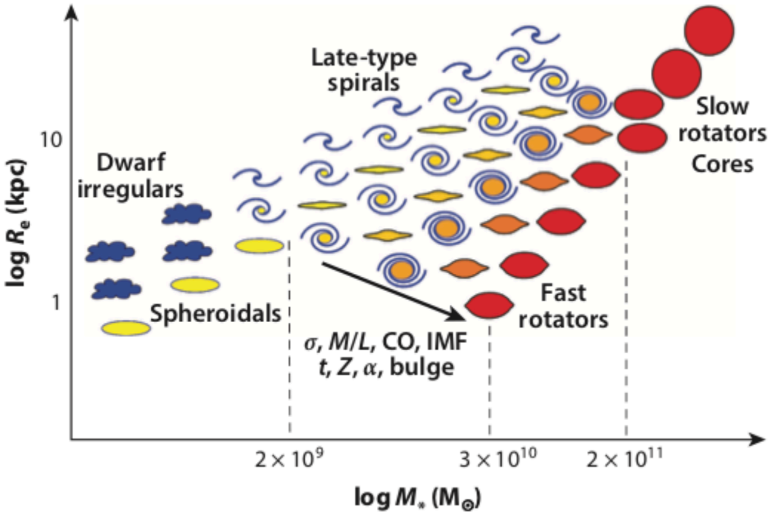

Figure 1.13: The size-mass relation considering the relation to morphological classifiaction. Taken from Cappellari [2016]

signatures (or natures) of galaxies in dense environments are influenced and defined. They are globally grouped into two, which are (i) gravitational interactions and (ii) gas-dynamic effects. The former case includes tidal encounters (Icke [1985]; Moore et al. [1999]), galaxy harassment (Moore et al. [1996, 1998]) and mergers including both major (e.g., Toomre [1977]) and minor (e.g., Bekki [1998]) mergers. The latter includes ram pressure stripping (Gunn & Gott [1972]), starvation (Larson et al. [1980]) and thermal evaporation (Nipoti & Binney [2007]).

1.5 Secular evolution : nature

The other main driver of galaxy evolution is the galaxy mass or the internal (or secular) processes driven by its stellar mass. Above a certain value of galaxy mass, the star formation is halted (Bundy et al. [2006]). Massive galaxies tend to be red with little star formation than less massive galaxies. This fact is closely related to the sub-linear nature of (phenomological) main sequence, and cosmological downsizing. The latter is the observational fact that more massive galaxies have stopped the star forming activity and become quiescent earlier than the less massive ones (Cowie et al. [1996]; Bell et al. [2005]; Bundy et al. [2005]). Accordingly, the age is older for a more massive galaxy. In the massive regime, the quenching of star formation can be occurred due to a hot halo after it is virialized and shock heated (e.g., Rees & Ostriker [1977];

White & Rees [1978]; White & Frenk [1991]). No more cool gas is accreted then and the current gas reservoir cannot be sufficiently cooled to form stars within a considerable time.

1.5.1 Galaxy co-evolution with supermassive blackhole

An additional important question related to galaxy evolution is on the connection between the galaxy assembly (and quenching) and the growth of central supermassive black hole. While the physical scales of galaxies and blackholes are different by more than three orders of magnitude, observational studies have shown that there is a tight correlation between the supermassive black hole mass in the center of the galaxy and the bulge mass (e.g., Kormendy & Ho [2013]). This suggests a possible physical link between the BH growth and galaxy evolution.

In galaxy evolutionary models, feedback mechanisms are necessary to explain the non-monotonic relation between the expected halo mass and the observed stellar mass (e.g., Bower et al. [2012]). The AGN feedback seems to help to explain the discrepancy between the halo mass function and the stellar mass function of galaxies, at least on the massive-end, though the detailed recipes are still unconstrained in both observations and simulations; the term of feedback indicates all the possible solutions related to the injection of energy into the ISM and haloes through jets, winds and radiation that can affect on various scales of time and space. Such feedbacks from the AGNs can prevent the cooling of baryons that can lead to a (rapid) quenching of galaxies. If they are strong enough, they can change the physical conditions of broader regions of the Universe.

1.6 **Dissertation outline**

The Dissertation presented herein focuses on revealing the physical properties of star forming galaxies associated to one of the indentified protoclusters at z=2.5, the protocluster 4C23.56. We expect that the protocluster may evolve into a massive cluster ($> 10^{14}$ $M_{\odot}$) at $z = 0$. We study the normal galaxy population on the main sequence, to give a broader context of galaxy evolution within high redshift overdense regions. We emphasize that the study presented here is one of the first systematic surveys to reveal the cold gas properties of typical star forming galaxies in the protoclusters and the probed redshift is the highest among the published literature (as of the submission date).

We summarize the parameter spaces in Table 1.1 to show the progress to date, of the studies toward field regions (unbiased, non-overdense region) and (proto)clusters, together with the missing pieces of parameters to present the motivation of studies in the Dissertation. The most well studied population is the massive, main-sequence galaxies. The properties of both less massive and less luminous (less star forming galaxies) populations are barely probed so far. Compared to field studies, very limited number of (proto)clusters are investigated in terms of gas content and kinematics. On each parameter space in the table, we add symbols to indicate the relative number of studies to provide qualitative impression. We note that the symbols does not provide quantitative definition; roughly speaking, a double circle (◎) indicates the number of investigated galaxies (in the designated item) is above $\sim$ 50, so it allows a systematic study; a circle (○) is used to indicate the number of the probed galaxies is above $\sim$ 10, and the studies are mostly done for individual galaxies; a triangle (△) indicates the number of galaxies less than $\sim$ 10 or the number of literature is less than a handful that targeted a small fraction of galaxies in the considering system; an X mark (×) is used to indicate that none of the galaxies are probed so far, or uncertain with undefined environment. In the table, we show the main targets and the parameters of our study in bold faces, which are the massive, main-sequence galaxies that are associated to the protoclusters and we investigate their properties of gas content and gas kinematics.

Table 1.1: Summary of previous observational studies done for star forming galaxies at z=1-3 in each item, together with studies in this dissertation.

	field	(proto)cluster
massive ($> 10^{10}\,M_\odot$)	◎	△ **: this dissertation** + a few literatures
less massive ($< 10^{10}\,M_\odot$)	△	△
high sSFR	○	△
on the main sequence	◎	△ **: this dissertation** + a few literatures
low sSFR	△	×?
gas content	◎	△ : **this dissertation**+ a few literatures
gas kinematics	◎	× : **this dissertation**

To probe the massive main-sequence galaxies, we take Hα emitters (HAEs) that were previously identified as relatively secure members in one of the high-z overdense structures at $z = 2.5$, by using the narrow band technique.

This dissertation aims to clarify the following things :

1. What is the gas fraction of the star forming galaxies in the protoclusters?

2. In relation to the gas content, is there a difference between the comparable field galaxies at the same redshift? If so, why would that be? If not, why would not?

3. Are star forming galaxies associated to the protoclsuters mostly mergers or disks?

4. For disk galaxies, is there any kinematic difference between the comparable field galaxies at the same redshift?

This dissertation is organized as follows. Chapter 2 presents a brief introduction of the selection of the protocluster and the target that are investigated throughout the dissertation and explains how we define the environment. In Chapter 3, we investigate the global gas content from the observations of CO lines and dust continuum and discuss the implication of the observed results. Chapter 4 presents the information of gas kinematics and we discuss the properties of disks and mergers. In Chapter 5, the summary and the conclusions of all of the measurements are provided. In Appendix C, we report the multi-band observations of continuum emission in cm-to-mm wavelengths, to provide the current limits on the number of continuum detection.

Throughout this paper, we assume $H_0 = 67.8\ \mathrm{km\,s^{-1}\,Mpc^{-1}}$, $\Omega_0 = 0.308$ and $\Omega_\Lambda = 0.692$ [Planck Collaboration et al., 2015]. The adopted initial mass fuction (IMF) is Chabrier IMF in the mass range 0.1 - 100 $\mathrm{M_\odot}$.

Pluralitas non est ponenda sine neccesitate

Occam's razor

Chapter 2

Protocluster 4C23.56 at z=2.49

A part of this chapter is published as Lee et al. [2017].

2.1 Sample selection and target field

2.1.1 Hα emitters

We targeted Hα emitters (HAEs) to study typical star forming population in the protocluster. They were originally detected by using the narrow band (NB) technique (Tanaka et al. [2011], I. Tanaka et al., in preparation) with MOIRCS/Subaru (Ichikawa et al. [2006]). The parent sample are 25 HAEs in total that are detected within the field of view (FoV) of MOIRCS/Subaru ($\sim$ 28 arcmin^2, corresponding to $\sim$ 84 co-moving Mpc^2). The narrow band filter technique can effectively choose galaxies that are located in a specific redshift range. Given the width of the NB filter, which is $\Delta\lambda = 0.023$ μm with a central wavelength of 2.288 μm, the Hα emission can be traced within $2.469 < z < 2.503$ ($\sim$40 comoving Mpc). The redshift range corresponds to the velocity width of ±1500 km s^{-1}, which is sufficiently large to trace the non-virialized protocluster members. For reference, the velocity dispersion of Hα ranges between 41 and 717 km s^{-1} as a whole, which are found in $z = 2.2$ and $z = 2.5$ protoclusters (Shimakawa et al. [2014]). For Lyman α emitters, it is $\sim 200 - 1000$ km s^{-1} (Venemans et al. [2007]; Chiang et al. [2015]). The expected size (R_e[*]) of high-z protoclusters near $z = 2 - 3$ is $R_e \sim 5 - 10$ comoving Mpc depending on the size at $z = 0$ (Chiang et al. [2013], but see also Muldrew et al. [2015]).

The stellar mass and star formation rate of the parent HAE samples spans three orders of magnitude and two orders of magnitude, respectively (Fig. 2.1, I. Tanaka et al., in preparation, and see next section for a brief description for the estimation of SFR and $M_\star$). In sSFR, the range is $0.2 < \mathrm{sSFR}(\mathrm{Gyr}^{-1}) < 301.0$. On the massive-end, the sSFR is consistent with the typical sSFR of the main sequence, which is $\sim 1 - 3$ (Gyr^{-1}) (e.g., Whitaker et al. [2012]; Speagle et al. [2014]). Provided this, we use the (NB-selected) HAEs as a probe for investigating the nature of typical (massive) star-forming galaxies on the main sequence. As such, HAEs have been used for understanding massive main-sequence galaxies (e.g., Geach et al. [2008]; Sobral et al. [2009]; Koyama et al. [2013]; Tadaki et al. [2013]; Oteo et al. [2015]).

---

[*] Based on Chiang et al. [2013], the definition of R_e is a radius within which a significant fraction (40%) of the total mass is included.

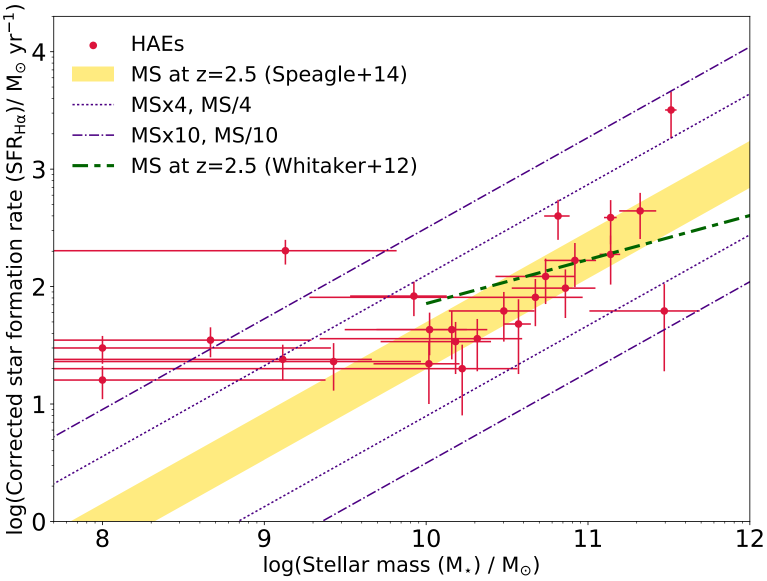

Figure 2.1: Distribution of galaxies in the SFR–$M_\star$ plane of the parent samples of HAEs in 4C23.56 (I. Tanaka et al., in preparation). The stellar mass is derived from the J and Ks bands and SFR is derived from the (continuum subtracted) NB flux by considering dust extinction and [NII] contribution (see also Sec 2.1.3 for a short description). We also plot lines for galaxies above ($\times 4$, $\times 10$, dotted) and below (1/4, 1/10, dashed dot) the main sequence at z=2.5. We used formulae presented in Speagle et al. [2014] (yellow band) and Whitaker et al. [2012] (green solid line and dashed lines for ± 0.3 dex) to show the z$\sim$2.5 main sequence galaxies. Most HAEs with stellar mass of M$\star$ $> 10^{10}$ M$_\odot$ are on the main sequence within the scatter of the main-sequence galaxies (± 0.3 dex), which will be the main targets discussed in the Dissertation.

2.1.2 Protocluster 4C23.56

Protocluster 4C23.56 was identified as an overdense region of the NB-selected HAEs that was a part of the MAHALO-Subaru (MApping HAlpha and Lines of Oxygen with Subaru) survey (Kodama et al. [2015]). The protocluster is close to radio galaxy 4C23.56 (HAE1) at z = 2.483 ± 0.003 (Roettgering et al. [1997]); it is one of the identified protoclusters with the searching method of using radio galaxies, as reviewed in the Introduction.

Protocluster 4C23.56 is known to have overdensities of differently selected galaxy populations besides HAEs (Tanaka et al. [2011]), including the populations of mass-selected distant red galaxies (DRGs) (Kajisawa et al. [2006]), extremely red objects (EROs, Knopp & Chambers [1997]), IRAC (Mayo et al. [2012]), MIPS (Galametz et al. [2012]) sources and SMGs observed at 1.1 mm with the Atacama Submillimeter Experiment (ASTE; K. Suzuki 2013 PhD thesis; M. Zeballos et al. in preparation). In other words, there are ancillary data sets to probe different galaxy populations, which makes the protocluster as one of the best targets to study

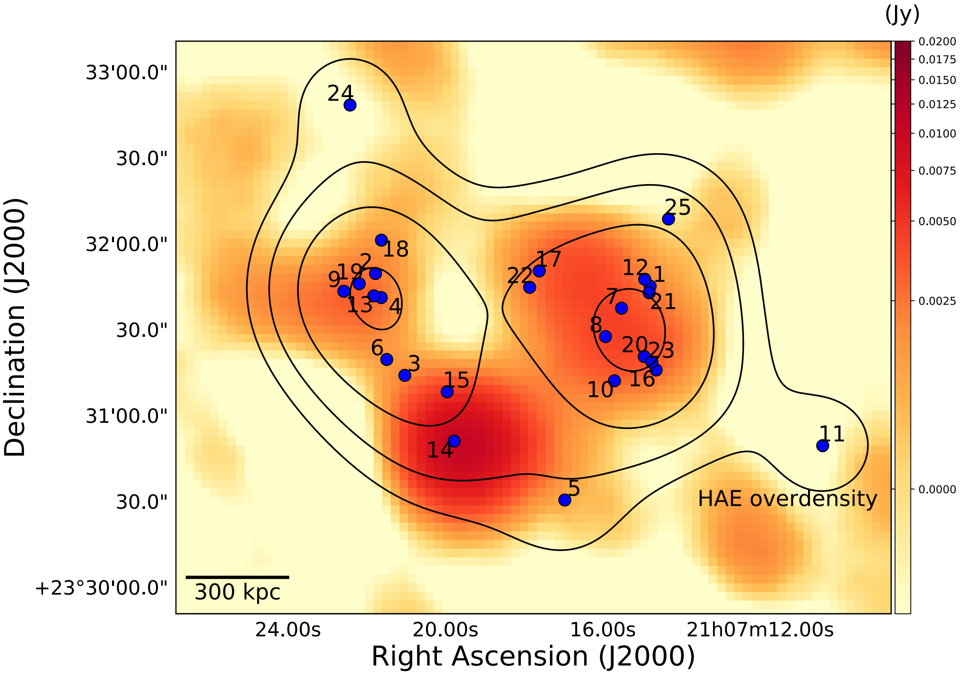

Figure 2.2: The distribution of HAEs in blue circles tagged by the source ID in 4C23.56, overlaid on the AzTEC/ASTE 1.1 mm single dish image (background color, K. Suzuki 2013 PhD thesis; M. Zeballos et al. in preparation). Multiple SMGs are overlapped with HAEs suggesting that HAEs are undergoing a dusty star formation. The brightest SMG (4C23-AzTEC 1) detected with AzTEC/ASTE at 1.1 mm, near HAE14, is not associated to the protocluster (Suzuki et al., in preparation). Thus, relatively moderate star forming galaxies on the main sequence are associated to the protocluster. The color bar shows the flux density observed by AzTEC in the unit of Jy. We also plot a HAE surface overdensity map in black contours that is estimated by assuming a Gaussian kernel with a FWHM of $0'.8$.

galaxy evolution in the high redshift protoclusters. Here, we only focus on HAEs because the observed populations other than HAEs have only rough (e.g., lower limit) or no redshift constraints in most cases; the redshifts of HAEs are relatively well-defined by the narrow-band selection ($\Delta z = 0.03$).

Related to HAEs, three SMGs discovered with ASTE overlap with the position of all of our HAEs except for HAE5, 11, 24 and 25. Further, the positions of three SMGs are roughly coincident with the peak overdensity of the HAEs (Fig. 2.2). This has prompted an idea that HAEs associated to the protocluster are experiencing dusty star forming phases and the SMGs are associated to the protocluster. Due to the coarse resolution of the submm single dish telescope, which is $\sim 30''$, a strong request for high resolution imaging has emerged. With this background, our case study of the protocluster region has started.

2.1.3 Ancillary data

MOIRCS/Subaru NIR data : Mstar and SFR

The stellar masses ($M_\star$) and SFRs of the HAEs are derived from the broad-band emissions in J and Ks bands and the Hα emissions within the NB-filter, respectively. The observations are executed under the seeing limited condition, i.e., $0.7''$. We note that 8 broad/intermediate/narrow-band images are existing in the optical-to-near infrared (NIR) range by using Subaru, i.e., B, IA427, r', z', J, H, Ks, and NB2288 (which is called as the 'CO'-filter). However, we use only the above three bands instead, because the data quality (i.e., the depth and the resolution) is not as good as that obtained in the longer-wavelengths (I. Tanaka et al., in preparation).

We present a brief summary of the derivation of physical parameters, which will be used in the thesis, and the full description of the data reduction and analysis for the NIR observations will be presented in I. Tanaka et al. (in preparation). The stellar mass is derived using $[J - Ks]$ color and Ks magnitude and calibrated from empirical fitting between Bruzual & Charlot [2003] (BC03) population synthesis model and the spectral energy distribution (SED) fitting with the FAST code[†]. The SFR is converted using the method described in Kennicutt & Evans [2012] from the Hα flux that is measured from the NB filter excess. We corrected for dust extinction in estimating the SFR, by taking into account the extinction term which is described in Garn & Best [2010]. This employs mass-dependent extinction correction. This correction method seems to hold up to z $\sim$ 1.5 (Sobral et al. [2012]; Domínguez et al. [2013]; Ibar et al. [2013]) and is often used for distant galaxies (z$\sim$2) as a proxy for dust extinction (e.g., Sobral et al. [2014]). We will discuss later the effect of the adopted dust correction method (Sec 3.3.2).

The massive ($M_\star > 10^{10}\ M_\odot$) HAEs are, in general, located near the main sequence defined at $z = 2.5$ (Speagle et al. [2014]; Whitaker et al. [2012, 2014]; Lee et al. [2015]) as shown in Fig. 2.1, though there are several outliers. The outliers on the massive-end are (potential) AGNs such as HAE1 (which is the radio galaxy 4C23.56) and HAE5 (Tanaka et al. [2011]). The SFR$_{\mathrm{H}\alpha}$ values of them are probably overestimated owing to the AGN contamination The other outlier is HAE7 with lower sSFR, which might be close to quenching or becoming passive.

Low-mass galaxies have large uncertainties than the massive ones. The primary reason of large errors is due to the low S/N in the photometry of both the Ks and J bands. We tentatively find a signature of enhanced star formation at a given stellar mass. Such signature as an intrin-

---

[†] http://w.astro.berkeley.edu/ mariska/FAST.html

sic elevation of star formation has been reported in other protocluster members (Hayashi et al. [2016]; I. Tanaka et al., in preparation). While the SFRs might be overestimated for the less massive galaxies (e.g., see Fig 8 in Shivaei et al. [2016]), further investigation is beyond the scope of the Dissertation. Since the galaxies detected in the ALMA observations, which will be presented in the following Chapters, are massive enough, the uncertainties in less massive galaxies would not critically affect our discussion.

Additionally,the adaptive optics (AO)-supported observations are recently conducted with IRCS/ Subaru in K' band at a resolution of $0.2''$ for several HAEs, where a natural guide star is available (Y. Koyama et al., in preparation; M. Lee et al., in preparation). The AO images will be shown in the next Chapter, only to provide some visual hints for understanding the nature of the galaxies. We defer the full description and detailed analysis of the AO observations in the future papers.

MIPS/Spitzer 24 μm

The MIPS/*Spitzer* 24 μm archival data (PI: A. Stockton ; Program ID 30240) is retrieved from the Spitzer Heritage Archive (SHA) interface[‡]. We used the MOPEX software package for image processing. The detailed analysis of MIPS is not presented in this dissertation, since the 24 μm image is only to show the visual characteristics, i.e., whether a galaxy is detected or not at 24 μm, of the HAEs in the following discussions in Chap 3.

2.2 Local environment

There are many different methods to measure the galaxy environment. Broadly, they are subdivided into two groups of those that use a ‘distance parameter’ of neighboring galaxies to define the density, and of the others that measure the galaxy density at a fixed aperture. This section introduces two measures of one each from the two groups to define the quantitative *environment* of protocluster 4C23.56.

[‡] http://sha.ipac.caltech.edu/applications/Spitzer/SHA/

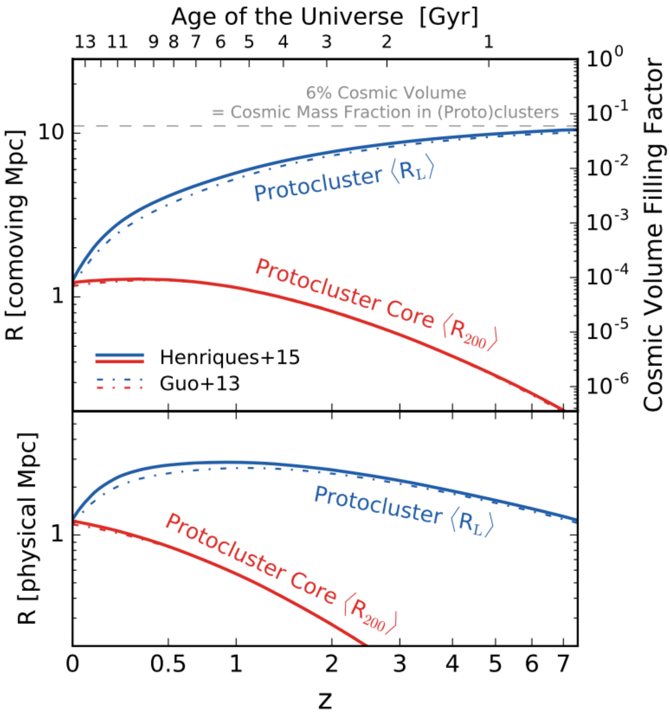

Figure 2.3: Evolution of size of the protocluster. Adopted from Chiang et al. [2017]

Fixed aperture

First, we measure a galaxy number density in a fixed aperture by assuming a typical size of high-z protocluster. We use a fixed aperture of Gaussian kernel with a FWHM of $0.'8$, which corresponds to a physical size of 200 kpc in radius (or $\sim$ 0.74 comoving Mpc in radius). The adopted aperture is reasonable, given the distribution of HAEs in the protocluster (see the physical scale shown in Fig 2.2) and the typical size of the protocluster core at $z \sim 2$ in simulations (Fig 2.3). The estimated (relative) scales of the overdensity based on the fixed-aperture, are shown in Fig 2.2 and Fig 2.4 as solid line contours. We also note that the evolution of the size of protoclusters is dramatic that the assumed size does not represent the typical size of (proto)clusters at different redshift; the volume which encompass the whole structure of protoclusters at $z = 6$ is expected to be roughly 6% of the cosmic volume, while the filling factor of protoclusters decreases significantly toward the local universe (Fig 2.3).

N-th nearest neighbor

Another method to define the environment is to use the distance to the N-th nearest neighbor. It is based on the idea that galaxies with closer neighbors are in denser environments. The projected surface density, σ_N, is defined by the equation as follows:

$$\sigma_N = \frac{N+1}{\pi r_N^2} \tag{2.1}$$

where (N+1) is the number of galaxy within r_N, defined by the distance to the N-th nearest neighbor. Since the distance information is not of sufficient accuracy without spectroscopic redshifts, we use the projected 2D measures onto the sky (but see a preliminary "3D"-distribution in Sec 4.2.2). Nevertheless, we implicitly impose a velocity cut of ±1500 $\mathrm{km\,s^{-1}}$, given the width of the NB filter (see Section 2.1.1).

Hereafter, we refer to the local density as that defined by the distance to the 5th nearest HAEs, if otherwise specified. In fact, the local density from the 5th-nearest HAEs is broadly consistent with the density estimated by the fixed aperture (Fig 2.4). Qualitatively speaking, the 5th nearest distance seems to be more sensitive to local densities than the fixed aperture.

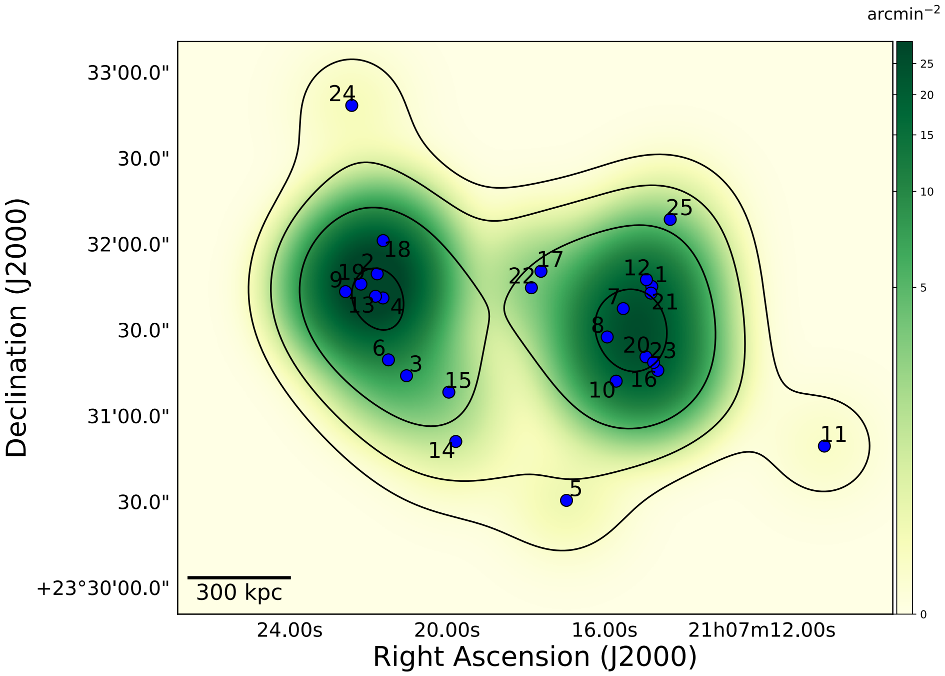

Figure 2.4: Overdensity estimated by the distance of 5th nearest HAEs in green color scale. The contour is the overdensity estimated from a fixed aperture. See text for details.

The most remarkable discovery in all of astronomy is that the stars are made of atoms of the same kind as those on the earth.

Richard Feynman

Chapter 3

Global gas content

This chapter is based on the published paper Lee et al. [2017].

This chapter reveals the gas content of star forming galaxies that are associated to one of the identified high redshift protoclusters. The term "gas" hereafter refers to the molecular gas as the measurement is. It can be regarded *effectively* as the total gas mass at the considered resolution (∼a few kpc) because the atomic gas content might be negligible (within the effective radius) with higher ISM pressure at high redshift, particularly at the massive-end (e.g., Obreschkow & Rawlings [2009]; Lagos et al. [2012]).

3.1 ALMA observations and analysis

3.1.1 CO (3–2) at Band 3 and 1.1 mm at Band 6

We observed the HAEs with Atacama Large Millimeter/submillimeter Array (ALMA). The Band 3 CO (3–2) observations have been performed to cover 22 HAEs, and the Band 6 1.1 mm observations have been performed to cover 19 HAEs (See Fig. 3.1). We have listed ALMA-targeted samples in Table 3.1, 3.2 and 3.3. The IDs in the first column are revised versions of those in Tanaka et al. [2011], and the reference IDs from Tanaka et al. [2011] are shown in the last column.

ALMA 1.1 mm observations were performed in Cycle 1 and CO (3–2) observations were performed in Cycle 2 (ALMA#2012.1.00242.S, PI: K. Suzuki).

The Band 6 continuum observations at 1.1 mm were observed typically $\sim$ 4 mins per pointing direction for 8-pointing target observations, covering 19 out of 25 HAEs (Fig. 3.1). The correlator is set to target four spectral windows with an effective bandwidth of $\sim$ 1.875 GHz each that is taken in the time division mode (TDM) (channel widths of 15.6 MHz or $\sim$ 18 km s^{-1}). The central frequencies of the four spectral windows are 256.0, 258.0, 272.0, and 273.8 GHz. The noise level (1σ) is $\sim$ 0.08 mJy beam^{-1} per field, except for one field with $\sim$ 0.12 mJy beam^{-1}. The field is where a bright SMG 4C23 AzTEC1 SMG ($S_{1.1\,\mathrm{mm,\,single\,dish}} = 10$ mJy) is detected (K. Suzuki 2013 PhD thesis; M. Zeballos et al. in preparation). The baseline lengths were between 17 and 462 m. We observed J2148+0657, Neptune, and J2025+3343 as a bandpass, flux, and phase calibrator, respectively.

The Band 3 CO(3-2) observations were executed for targeting 22 HAEs. The total on-source time was 4 hours for 4-pointing (thus $\sim$ 1 hr per pointing direction). The correlator is set to target four spectral windows (SPWs) with effective bandwidth of $\sim$ 1.875 GHz each. One SPW centered at 99.3 GHz, is taken in the frequency division mode (FDM) (channel widths of 0.49

MHz or $\sim$ 1.5 km s^{-1}), to trace the redshifted CO(3–2) line ($\nu_{\rm rest}$ = 345.79599 GHz) at $z = 2.5$. The remaining three spectral windows are taken in the time division mode (TDM) (a channel width of 15.6 MHz or 47 km s^{-1}) and are centered at 101.1, 111.3 and 113.2 GHz. The velocity coverage of the CO observations is $\sim$ 6400 km s^{-1}, corresponding to a redshift coverage of $2.385 < z < 2.516$ in the lower side band and $2.031 < z < 2.134$ in the upper side band. This is sufficient to cover the expected redshift range of the 22 HAEs detected by the NB technique ($z = 2.486 \pm 0.017$). Larger field of view and sufficient pointing allowed for all 19 HAEs covered by the 1.1 mm observations to be fully covered by the Band 3 observations (Fig. 3.1). The typical noise (1σ) level is $\sim$ 0.17 mJy for the spectral resolution of 100 km s^{-1}. In general, we estimate the signal-to-noise ratio (S/N) with a spectral resolution of 100 km s^{-1}, except for a case in which we needed a higher velocity resolution. For example, HAE5 is analyzed in higher spectral resolution, since strong emission in a single channel are found with S/N $>$ 6.5. The noise level in this case became worse, i.e., $\sim$ 0.3 mJy, but it was sufficient in that the detection of this galaxy satisfied our detection criteria (see Section 3.1.2). The flux calibrator was Titan for Band 3. J1751+0939 and J2148+0657 were chosen as bandpass calibrators and J2025+3343 as a phase calibrator. The minimum baseline was 43 m, and the maximum baseline was 1574 m for Band 3.

We applied the CLEAN algorithm to the calibrated visibilities with natural weighting to produce images for both observations by using the Common Astronomy Software Applications package (CASA, used 4.2.2 version for calibration and imaged with 4.6.0 version). The absolute flux uncertainties for both bands were estimated as $\sim 15 - 18\%$, which were not taken into account for the flux error throughout this paper. The synthesized beam sizes are $0''.91 \times 0''.66$ (PA = 23.5°) for Band 3 and $0''.78 \times 0''.68$ (PA = 0.4°) for Band 6. The sub-arcsec resolution is sufficient to pin down SMGs detected by ASTE (with its typical beam size of $\sim 30''$) and to search for counterparts detected at other wavelengths, e.g., images obtained in NIR/optical bands.

3.1.2 Detection and flux measurement

Detection criteria

Searching area for detection is within a radius of $r = 1''$ around the position of the HAEs. We set a following detection criteria for detection.

We regarded a galaxy as detected in ALMA Band 6 (1.1 mm continuum) if a peak flux density

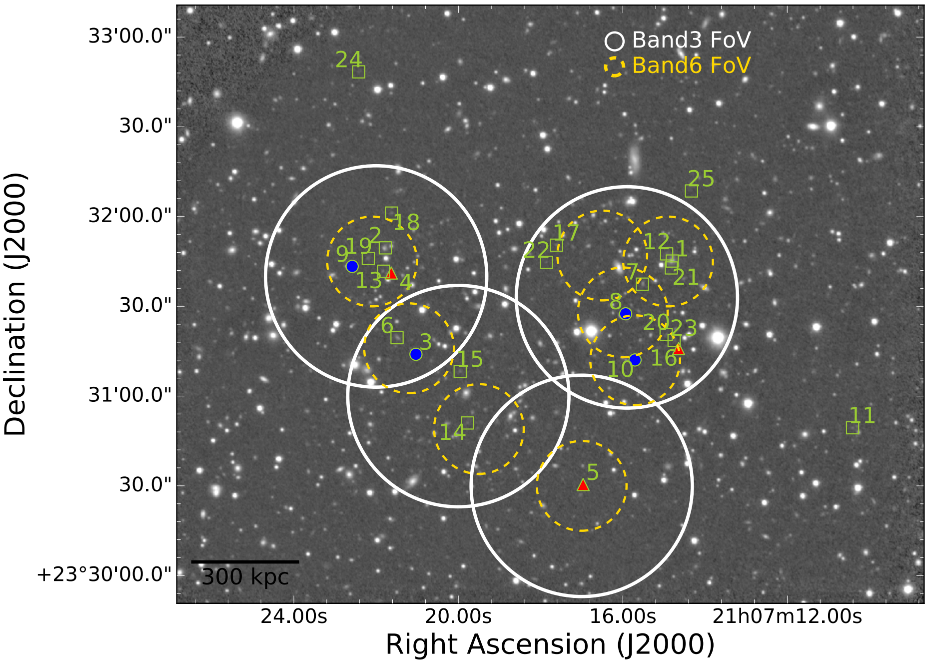

Figure 3.1: The distribution of HAEs. We show the source ID near the position of the HAEs. The background image is the Subaru/MOIRCS Ks band image (I. Tanaka et al., in preparation). The blue filled circles indicate galaxies detected simulataneously in CO (3–2) and 1.1 mm, red triangles indicate galaxies only in CO (3–2). Green open squares show the remainder of HAEs detected with the NB filter technique. The fields of view (FoVs) of ALMA Band 3 CO (3–2) (white open circles) and Band 6 1.1 mm (yellow dashed circles) observations are shown on the map. The total number of pointing is 4 and 8 for Band 3 and Band 6, respectively. A scale bar is shown at the bottom left corner to represent a physical size of 300 kpc.

is above 4 σ. A CO (3–2) line was regarded as detected if at least two among three criteria (a-c) are satisfied : (a) a peak flux $>$ 4 σ, (b) at least two continuous channels including a maximum peak flux channel have flux $>$ 3.5 σ, and (c) (spatially smoothed) velocity-integrated peak flux S/N is above 5 before the primary beam correction. All galaxies except HAE4 (=6/7) satisfy all the conditions. HAE4 has two distinct but not continuous peaks ($>$ 4 σ) that are 100 km s^{-1} (one channel) apart (Fig. 3.2). We show CO (3–2) spectra in Fig. 3.2-3.5.

The CO (3–2) redshift is broadly consistent with other current available detections including CO (4–3) (see Chap 4) and the NIR spectroscopy (Tanaka et al. in prep.). For the definition of the CO (3–2) redshift, we choose the median velocity component due to the broad nature of spectrum for many of the galaxies and relatively low S/N.

Flux

The flux measurement is based on the measurement of the peak flux and the peak integrated flux which were measured after the map is smoothed to get high S/N. We measured the flux after primary beam correction. All of the sources are within a good sensitivity region ; thus, the measured flux was not changed significantly by the primary beam correction (within $\sim$ 10%).

For the estimate of the noise level in the CO (3–2) line cube, we measured by averaging five line-free channels in the primary-beam-corrected-image. Small scale data cubes were cut out around the source (with a size of 15 $\times$ 15″) using `immath` from the original map with FoV of $\sim$ 74″ and then masked (with a radius of 1.5 times the beam size) for the known bright sources (including HAEs). The noise level in Band 6 was derived from the sliced image around the source with a size of 6″ $\times$ 6″ from a larger image with FoV $\sim$ 30″ and then masked for the detected known sources.

We smoothed images using the CASA command `imsmooth`. The main reason for this is to neglect a galaxy structure for the measurement of global gas content. The S/N increased by collecting diffuse, extended emissions from the outskirts of a galaxy that could be missed with the sub-arcsec ($\sim$ 6 kpc at $z = 2.5$) beam size. We used image-based smoothing instead of uv-visibility based tapering since smoothing on the image gives a better S/N than tapering the uv visibilities. Smoothing also allowed us to avoid the divergence of 1-component Gaussian spectrum fitting for a disturbed galaxy, which likely constitute roughly a half of the detected HAEs. The images in Band 3 for CO (3–2) were smoothed channel by channel.

Table 3.1: Source information for detection

Source ID	RA$_{\mathrm{CO32}}$ (J2000)	Dec$_{CO32}$ (J2000)	$M_{\star}$ $\times$ 10^{10} M$_{\odot}$	SFR(H-alpha, corr) M$_{\odot}$ yr^{-1}	I$_{\mathrm{CO}\ (3-2)}$ Jy km s^{-1}	S$_{1.1\mathrm{mm}}$ mJy	ID in T11
HAE3	316.837650	23.520500	13.0±1.9	176±78	0.352±0.06	0.53±0.14	354
HAE4	316.840213	23.527986	19.7±5.1	414±175	0.246±0.03	<0.54	479
HAE5	316.820742	23.508458	6.1±1.1	374±140	0.09±0.02	<0.33	153
HAE8	316.816433	23.524292	7.8±2.7	156±63	0.263±0.03	0.75±0.12	431
HAE9	316.844121	23.528694	6.8±3.6	90±40	0.542±0.06	1.21±0.21	511
HAE10	316.815525	23.520000	5.1±2.6	115±47	0.362±0.06	0.44±0.12	356
HAE16	316.811025	23.520958	4.4±4.3	76±32	0.493±0.07	<1.1	–

The adopted size of smoothing Gaussian kernel is $0''.8 \times 0''.8$ for Band 6 and $0''.6 \times 0''.6$ for Band 3. A detailed analysis on the choice of Gaussian kernels is presented in Appendix A.1. To summarize the method, we investigated S/N as a function of the smoothing kernel. This is effectively equivalent to considering the growth curve of galaxy emission as a function of aperture size. By using the smoothing kernel sizes, images in different bands are with a similar smoothed beam size of $1''.1 \times 0''.9$ for Band 3 and $1''.1 \times 1''.0$ for Band 6. The adopted sizes give the maximum S/N, and the flux is $\sim 50 - 90\%$ of the maximum flux measured up to $4''.0$ (physical size of ~ 33 kpc at $z = 2.5$) smoothing kernel. The beam sizes correspond to $\sim$ 8.5 kpc in physical scale for both 1.1 mm and CO (3–2) and are sufficient to recover the total flux given the typical size of a star-forming galaxy at high z ($r_{1/2,\mathrm{CO}} \sim 5$ kpc, e.g., Bolatto et al. [2015]).

We compute and choose an integrating range for CO (3–2) instead of performing a Gaussian fit for CO (3–2), following the description in Seko et al. [2016]. The map was checked by eye afterward for unexpected cases, such as extremely broad line widths to integrate, because some galaxies have unusual spectra that are not well-fitted with a single gaussian, in addition to inhomogeneous spatial distributions and the velocity gradients (see Fig. 3.2-3.5 for the morphology and spectrum)

We detect seven and four HAEs in CO (3–2) and dust continuum out of 22 and 19 HAEs, respectively, from our detection processes in our targeted fields (see also Fig. 3.2-3.5 for a gallery of detected sources). We summarize flux values for detected sources in Table 3.1, and for non-detection in Table 3.3. The detected sources have stellar mass $> 4 \times 10^{10}$ M$_{\odot}$, and two of them have stellar masses exceeding $\sim$ 10^{11} M$_{\odot}$ (HAE3, HAE4).

3.2 Gas mass

Total gas mass is measured from the estimated flux (Sec 3.1.2) of dust continuum and CO (3–2) line emission. In the following two sections, we address how the gas mass is estimated.

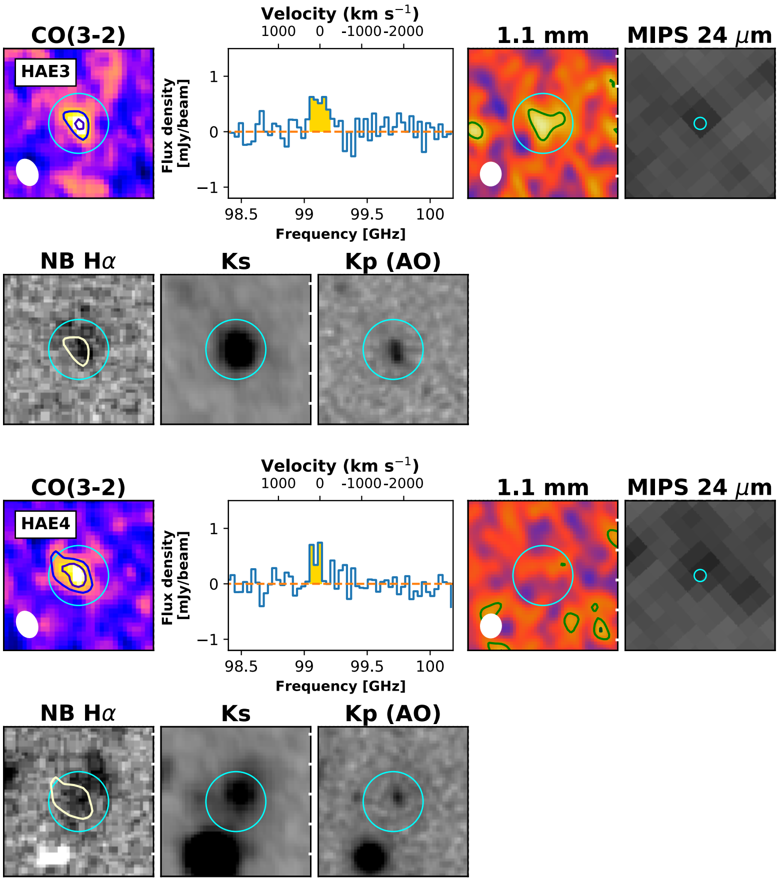

Figure 3.2: Multi-band images of sources detected using ALMA with having either CO (3–2) or 1.1 mm detection for HAE3 (top two rows) and HAE4 (bottom two rows). From left to right (upper row of each target) : CO (3–2) integrated intensity, CO (3–2) spectrum at the peak, 1.1 mm, MIPS 24 μm, (lower row ; continuum-subtracted NB Hα, Ks, and Kp (AO). The center of each panel is set by the CO (3–2) peak position. We plot contours of CO (3–2) and 1.1 mm emission in steps of 2σ starting from 3σ since the color scales of the panels are is slightly different. The beams of CO (3–2) ($0''.91\times0''.66$, PA = 23.5°) and 1.1 mm ($0''.78\times0''.68$, PA = 0.4°) are shown on the bottom left. The CO (3–2) spectrum is shown for the range between 98.4 and 100.2 GHz into which the redshifted CO(3-2) at z$\sim$2.5 would fall. The velocity resolution is set to 100 km s^{-1} in general, but it is set to 30 km s^{-1} for HAE5 (see Fig. 3.3). The yellow region of each spectrum is the integrating velocity range that delivers the highest S/N (Sec. 3.1.2). The 3σ for the CO (3–2) contour is also overlaid on each NB Hα image for comparing the distribution. In the AO images, we find compact components for the most massive galaxies among those detected (HAE3 and 4), while the rest are marginally visible, suggesting the relatively diffuse nature of the stellar component. We also plot a cyan circle with a radius of $1''$, which is also centered on the peak position of CO(3-2), to show the scale of the panel and to point out that the counterpart at different wavelengths is located near the CO(3-2) position or within $2''$ in general (see also Appendix A.2). As the MIPS/Spitzer observations at 24 μm have a coarse resolution compared to those of other bands, we zoom out images to clearly show the detection.

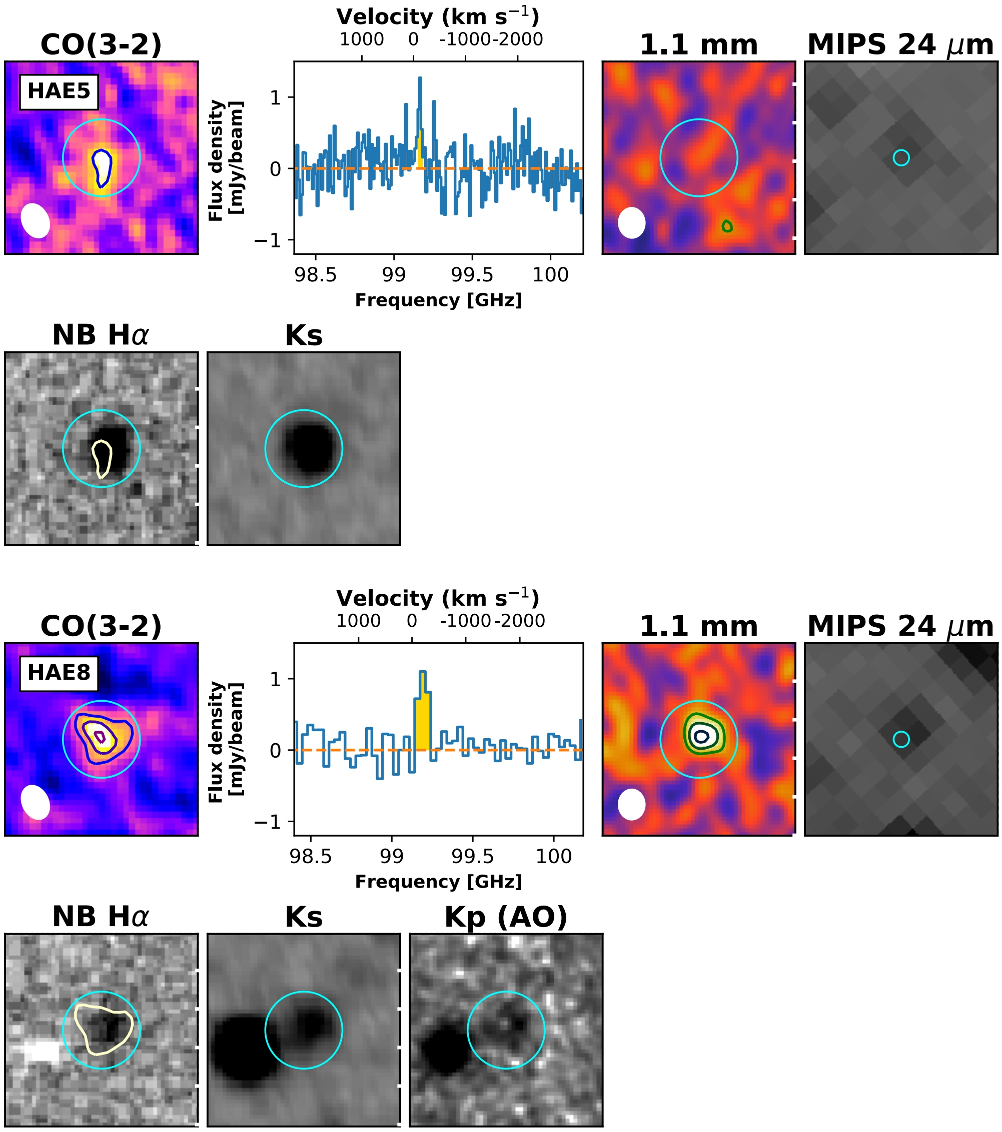

Figure 3.3: Multi-band images for the galaxies having either CO (3–2) or 1.1 mm detection (continued) : HAE5 (top two rows) and HAE8 (bottom two rows). Refer to Fig. 3.2 for the description of each panel and symbols. There was no coverage of the AO observation in Kp for HAE5. Since the line width for HAE5 is narrow (see also the text and Table 3.2), we show the spectrum with a velocity resolution of 30 km s^{-1}, as opposed to other galaxies, which are shown with a resolution of 100 km s^{-1}.

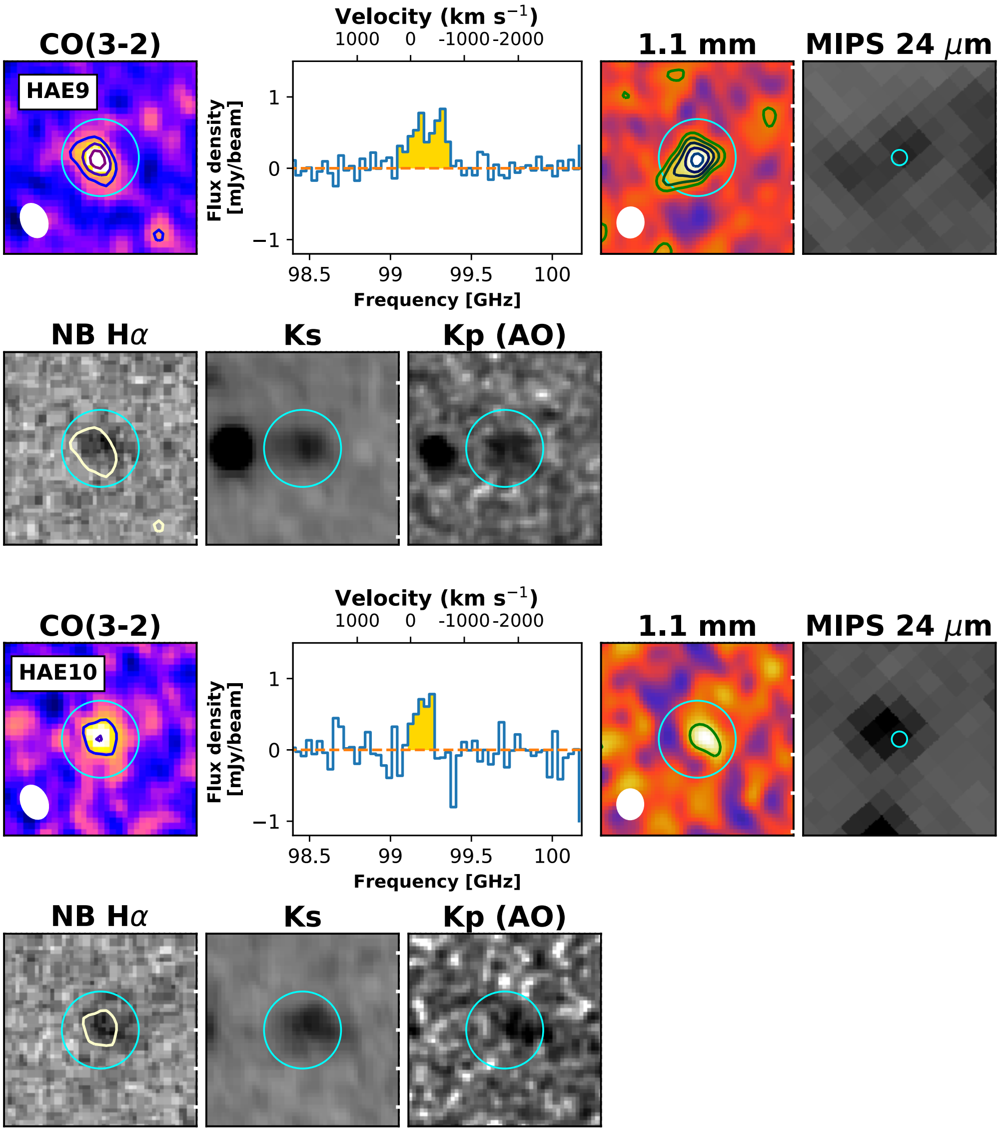

Figure 3.4: Multi-band for the galaxies having either CO (3–2) or 1.1 mm detection (continued) : HAE9 (top two rows) and HAE10 (bottom two rows). Refer to Fig. 3.2 for the description of each panel and symbols.

Table 3.2: The estimates of physical parameters for detection

Source ID	$z_{\mathrm{CO}\ (3-2)}$	line width km s^{-1}	$\mathrm{M}_{\mathrm{gas,\,CO32}}$ $\times\,10^{10}\ \mathrm{M}_{\odot}$	$\mathrm{M}_{\mathrm{gas,\,dust}}$ $\times\,10^{10}\ \mathrm{M}_{\odot}$	SFE Gyr^{-1}	$\mathrm{f}_{\mathrm{gas,\,CO}}$
HAE3	2.4861	500	10.55 ± 1.8	5.9 ± 2.16	1.68	0.45
HAE4	2.478	300	6.86 ± 0.84	<6.22	6.04	0.26
HAE5	2.4873	100	3.14 ± 0.7	<3.96	11.95	0.34
HAE8	2.4861	300	8.69 ± 0.99	8.35 ± 2.51	1.81	0.53
HAE9	2.4861	1000	18.43 ± 2.04	13.48 ± 4.14	0.49	0.73
HAE10	2.4861	500	13.15 ± 2.18	4.9 ± 1.83	0.88	0.72
HAE16	2.4826	600	18.52 ± 2.63	<12.5	0.41	0.81

Table 3.3: Information for undetected sources

Source ID	$\mathrm{RA}_{\mathrm{H}_{\alpha}}$ (J2000)	Dec_{α} (J2000)	S_{CO32} mJy	$\mathrm{S}_{1.1\mathrm{mm}}$ mJy	$\mathrm{M}_{\mathrm{gas,\,CO32}}$ $\times\,10^{10}\ \mathrm{M}_{\odot}$	$\mathrm{M}_{\mathrm{gas,\,dust}}$ $\times\,10^{10}\ \mathrm{M}_{\odot}$	ID in T11
HAE1	316.811658	23.529211	< 0.67	< 0.32	< 11.07	< 3.54	491
HAE2	316.840738	23.530434	< 0.52	< 0.50	< 8.61	< 5.60	526
HAE6	316.839548	23.522090	< 0.95	< 0.46	< 15.66	< 5.08	393
HAE7	316.814680	23.527065	< 0.52	< 0.86	< 8.52	< 9.56	–
HAE12	316.812222	23.529876	< 0.67	< 0.32	< 11.12	< 3.56	–
HAE13	316.840917	23.528263	< 0.49	< 0.43	< 8.02	< 4.79	500
HAE14	316.832414	23.514173	< 0.53	< 0.70	< 8.68	< 7.79	–
HAE15	316.833151	23.518959	< 0.52	–	< 8.56	–	–
HAE17	316.823395	23.530683	< 1.02	< 1.07	< 16.92	< 11.93	543
HAE18	316.840110	23.533663	< 0.7	–	< 11.54	–	–
HAE19	316.842465	23.529443	< 0.5	< 0.37	< 8.21	< 4.12	–
HAE20	316.812277	23.522381	< 0.65	< 1.01	< 10.67	< 11.20	–
HAE21	316.811748	23.528571	< 0.63	< 0.33	< 10.45	< 3.67	–
HAE22	316.824409	23.529090	< 1.03	–	< 17.09	–	–
HAE23	316.811469	23.521843	< 0.71	< 1.10	< 11.71	< 12.27	–

3.2.1 CO (3–2) to gas mass

While being only a fraction of the total gas content, the CO line emission has been one of the most successful observing methods in measuring the gas. The strategy of using the optically thick CO line emission in the total gas mass has been established around the time millimeter observation became available in the late 1980s [Dickman et al., 1986; Solomon et al., 1987]. Lower-J ($J < 4$) lines are a good probe for the total cold gas mass (e.g., Carilli & Walter [2013]), and the lower-J CO lines have been used for several pioneering works on high-z star-forming galaxies as well as SMGs (e.g. Magdis et al. [2012]; Tacconi et al. [2013]; Daddi et al. [2015]). Compared to this, higher-J rotational transitions of CO have large uncertainty for the unknown excitation.

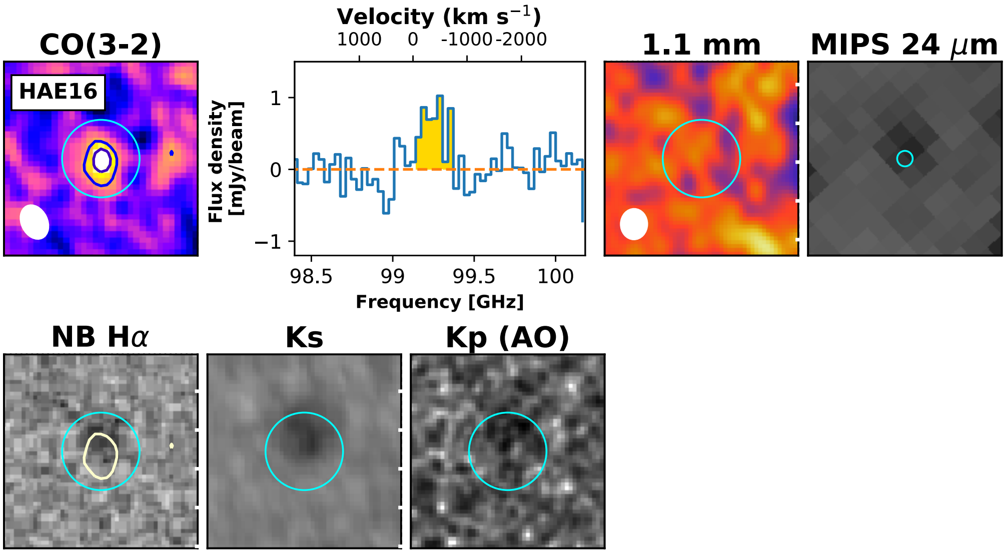

Figure 3.5: Multi-band images for the galaxies having either CO (3–2) or 1.1 mm detection (continued) for HAE16. Refer to Fig. 3.2 for the description of each panel and symbols.

The gas mass from CO (3–2) emission is derived by following the prescription presented in Genzel et al. [2015]. To the first order, it uses a typical conversion factor $\alpha_{\rm MW} = 4.36\ M_\odot\ ({\rm K\,km\,s^{-1}\,pc^2})^{-1}$. We use this recipe since the massive HAEs are on the main-sequence. Then the metallicity (Z) dependence of the conversion factor, i.e., $\alpha_{\rm CO\,1} = \alpha_{\rm MW} \times A(Z)$, is considered. A(Z) corresponds to the metallicity dependence of the conversion factor calculated by taking the geometric mean of Bolatto et al. [2013] (the equation (6) in G15) and Genzel et al. [2012] (the equation (7) in G15). For the metallicity, we adopted the galaxy's metallicity derived from an empirical mass-metallicity relation, as presented in Genzel et al. [2015] (equation (12a), which uses a fitting function of Wuyts et al. [2014]). It is because, we have yet incomplete metallicity measurements for all the samples; only a fraction of [NII] and Hα spectroscopic data are obtained and some have low S/N. The adopted metallicity-dependent conversion factor is in the range of $\alpha_{\rm CO,1} = [4.4, 5.9]$. The metallicity varies within a modest range ([8.50, 8.65]) for the massive-end, which is robust to the adopted recipe for metallicity; for example, the one described in Mannucci et al. [2010] would yield a value lower by < 0.02 dex, which results in a conversion factor that does not vary by more than a factor of 2. There might be a tendency of lower metallicity in high-z overdense region (e.g., Valentino et al. [2015]), where a pristine gas is likely being accreted from the cosmic web particularly at high redshift. However, this statement is controversial at this moment that no consensus has been delivered, e.g., higher metallicity (e.g., Steidel et al. [2014]; Shimakawa et al. [2015]), a flat mass-metallicity relation (thus, higher metallicity in lower mass regime e.g., Kulas et al. [2013]), and the same mass-metallicity relation as fields (e.g., Tran et al. [2015]) at $z \sim 2$. Therefore, we choose to use the general description of the stellar mass–metallicity relation. We discuss later the validity of the choice of conversion factor in Section 3.3.3

For measuring gas mass, we need to assume the luminosity (brightness temperature) line ratio to estimate the lowest J=1–0 emission. We use the typical value $R_{13} = 1.9$, which can be applied to both high-z typical star-forming galaxies and SMGs (e.g., Tacconi et al. [2008, 2013]; Carilli & Walter [2013]; Daddi et al. [2015]).

We then compute the gas mass as expressed by Eq. 3.1 at a given luminosity $L'_{\mathrm{CO}\,J}$ by using a conversion factor $\alpha_{\mathrm{CO}\,1}$, CO $J \rightarrow J-1$ line flux $F_{\mathrm{CO\,J}}$, source luminosity distance D_L , redshift z, and observed line wavelength $\lambda_{\mathrm{obs}\,J} = \lambda_{\mathrm{rest}\,J}(1+z)$ (Solomon et al. [1997]; Bolatto et al. [2013]), where $J = 3$ in our case.

$$\begin{aligned} M_{\mathrm{gas\,,CO}}\,[M_\odot] &= \alpha_{\mathrm{CO}\,1} \times L'_{\mathrm{CO}\,1} \\ &= 1.57 \times 10^9 \left(\frac{\alpha_{\mathrm{CO}\,1} \times R_{1\,3}}{\alpha_{MW}}\right) \\ &\quad \times \left(\frac{F_{CO\,3}}{\mathrm{Jy\,km\,s^{-1}}}\right) \times (1+z)^{-3} \\ &\quad \times \left(\frac{\lambda_{\mathrm{obs}\,3}}{\mathrm{mm}}\right)^2 \times \left(\frac{D_L}{\mathrm{Gpc}}\right)^2 \end{aligned} \tag{3.1}$$

Since the main aim for this study is to compare our survey with other high-z field[*] surveys based on either CO and/or dust continuum, we apply the same analysis for the available data set.

In comparing CO measurement, we refer to the PHIBBS-I sample presented in Tacconi et al. [2013]. The PHIBBS-I surveys targeted galaxies located in several fields including the Great Observatories Origins Deep Survey-North (GOODS-N) field, Q1623, Q1700, Q2343, and Extended Groth Strip (EGS) field. This is a CO(3-2) line survey targeting massive galaxies ($\log(M_\star/M_\odot) \geqslant 9.5$) and those mostly on the main-sequence star-forming galaxies between $1 < z < 3$. Later, we select PHIBBS-I galaxies within the main sequence (±0.3 dex using Whitaker et al. [2012]) at $2 < z < 3$ above $\log(M_\star/M_\odot) > 10.6$ which are unfortunately only 7 in number, and its stellar

---

[*] We assume that the compared galaxies are in 'general' fields, which may have probed a presumably large volume (i.e., a relatively wide redshift range to cover the large scale structure); thus, cosmic variance may not significantly affect the comparison.

mass range is $10.6 \leqslant \log(M(M_\star)) \leqslant 11.2$, which is almost the same stellar mass range as that detected in CO(3-2) (i.e., $10.6 \leqslant \log(M(M_\star)) \leqslant 11.3$). We apply the same gas recipe for the PHIBBS-I galaxies, while the values of $M_\star$ and SFR are simply adopted from Table 2 in Tacconi et al. [2013], which is derived from SED fitting.

The measured CO line flux and the derived total molecular gas masses for individual HAEs are summarized in Table 3.1 and Table 3.2, respectively. The derived molecular mass ranges between $(0.3 - 1.9) \times 10^{11}$ $\mathrm{M}_\odot$. The upper limit of molecular gas mass is set to 3 σ assuming a velocity width of ~ 300 km s^{-1}, i.e., a typical galactic disk rotation, as presented in Table 3.3.

3.2.2 1.1 mm dust to gas mass

Another method to measure total gas mass is by using dust continuum. We use a method presented in Scoville et al. [2016]. Since the flux around the peak of the dust SED is no longer optically thin, the dust mass fitted with the FIR-only SED (i.e. using a SED model that is fitted only around the FIR peak with Herschel) would yield significant uncertainties in measuring total gas mass (Scoville et al. [2016]; Berta et al. [2016]). The dust (and gas) mass fitted by the SED model is a rather luminosity-weighted value. To compensate this, Scoville et al. [2014] presented a locally calibrated luminosity-mass relation for measuring gas content by assuming the global mass-weighted dust temperature. We assume a dust temperature of 25 K as suggested in Scoville et al. [2014, 2016].

The gas mass is calculated as follows :

$$\begin{aligned} M_{\text{gas ,dust}}\,[M_\odot] &= \frac{1.78\times10^{10}}{(1+z)^{4.8}}\left(\frac{\Gamma_{\mathrm{RJ}}}{\Gamma_0}\right)^{-1}\frac{6.7\times10^{19}}{\alpha_{850}} \\ &\times\left(\frac{S_\nu}{\mathrm{mJy}}\right)\left(\frac{\nu}{353\mathrm{GHz}}\right)^{-3.8}\left(\frac{D_{\mathrm{L}}}{\mathrm{Gpc}}\right)^2 \end{aligned} \tag{3.2}$$

where S_ν is the observed dust continuum flux in mJy, α_{850} is a constant for calibrating luminosity to gas mass, and $\frac{\Gamma_{\mathrm{RJ}}}{\Gamma_0}$ is the RJ correction factor with $\Gamma_0 = \Gamma_{\mathrm{RJ}}(0, T_d, \nu_{850}) = 0.71$ and Γ_{RJ} given by

$$\Gamma_{\mathrm{RJ}}(T_d, \nu_{\mathrm{obs}}, z) = \frac{h\nu_{obs}(1+z)/kT_d}{e^{h\nu_{obs}(1+z)/kT_d} - 1} \tag{3.3}$$

There might be some metallicity dependence, but would not affect our discussion, because the stellar mass range of the detected sources are sufficiently large. However, we note that the dust-based measurement may yield a systematically lower value than the CO-based measurements (e.g., Genzel et al. [2015]; Decarli et al. [2016b]; see also some discussions in section 3.3.3 and Fig. 3.6).

The calculated results for 1.1 mm are also summarized in Table 3.1 and 3.2, and images are shown in Fig. 3.2-3.5. We find the gas mass derived from 1.1 mm is in the range of $(0.5-1.4)\times 10^{11}$ $\mathrm{M}_{\odot}$ for four objects.

For the comparison with field galaxies, we refer to the study of Scoville et al. [2016], which targeted galaxies extensively in the Cosmic Evolution Survey (COSMOS) field within the redshift range $1 < z < 6$. The same analysis is applied for ALMA LABOCA Extended Chandra Deep Field-South Survey (ECDF-S) Submm Survey (ALESS) SMGs which are partly covered in GOODS-S. Since our prime focus is on the galaixes on the main sequence, we choose the main-sequence SMGs within a redshift range of $2 < z < 3$, the stellar mass of which is restricted to $\log(M_{\star}/M_{\odot}) > 10.6$; therefore, $10.4 \leqslant \log(M(M_{\star})) \leqslant 11.7$. The gas mass is calculated from 870 μm as listed in Hodge et al. [2013] (primary beam corrected flux, column 8 in Table 3) and by combining it with the information (i.e., $M_{\star}$, SFR, redshift) from another SED fitting (i.e., MAGPHYS) presented in da Cunha et al. [2015]. Since the ALESS SMGs are observed at 870-μm, we limit the redshifts of SMGs to < 3. The 870-μm no longer traces the RJ tail above the redshift, and it may produce large uncertainties in the estimation of gas mass when Scoville et al. [2016] recipe adopted.

3.2.3 Combined results of SFR vs M_{gas}

The gas masses derived from different estimators of CO (3–2) and 1.1 mm are roughly consistent with each other; three HAEs (HAE3, HAE8, and HAE9) are roughly consistent within errors, and the $M_{\mathrm{gas,\,dust}}$ of HAE10 is less than $M_{\mathrm{gas,\,CO}}$. The latter case might be related to the variation of dust-to-gas ratio (thus metallicity) and optically thin CO emissions, while it is difficult to constrain the reason with the given data (see Sec. 3.3.3 for discussion).

However, there may be some cautions for this. Typically the gas mass from the 1.1 mm emission is systematically smaller for all four cases, even though the sensitivity limit of the 1.1 mm observations is deeper in terms of the gas content with the prescription of Scoville et al. [2016]

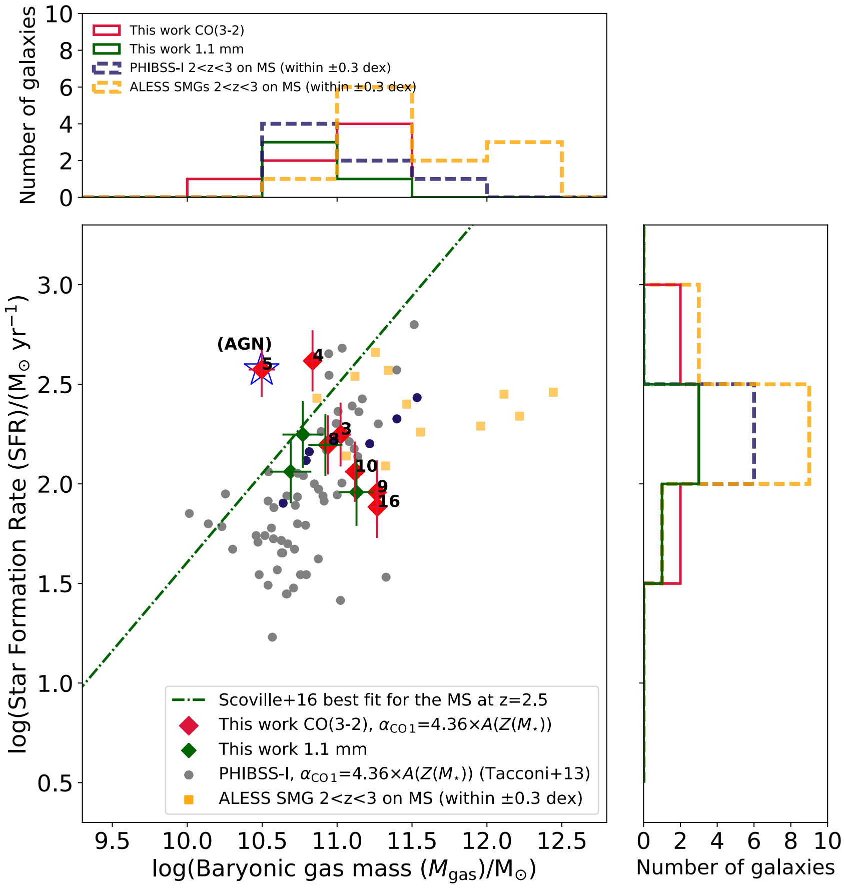

Figure 3.6: Derived molecular mass distribution with respect to SFR. The molecular mass is derived from CO (3–2) (red diamonds) or dust continuum (green diamonds) detection (see Section 3.2 for details). HAE5 is indicated with a star symbol to clarify the existence of AGN, the SFR of which derived from the Hα emission may be overestimated. We also plot other high-z molecular and dust continuum survey results from PHIBBS-I (Tacconi et al. 2013), galaxies in the COSMOS field (Scoville et al. 2016) and ALESS (Hodge et al. 2013; da Cunha et al. 2015) by applying the same analysis on $M_{\rm gas}$ (but not for SFR or $M_\star$). The PHIBBS-I survey (grey circles) is based on the CO(3-2) measurements for star-forming galaxies on the main sequence. We indicated in dark blue the PHIBSS-I galaxies that are massive ($M_\star > 4 \times 10^{10}$ M$_\odot$) on the main sequence (±0.3 dex) within $2 < z < 3$. Scoville et al. [2016] (dashed green line) is based on the dust continuum (Band 7 at 870 μm) observation. The ALESS survey is also observed at the 870 μm continuum by using ALMA, but the observation was made toward LESS SMGs found in the ECDF-S field. Yellow squares are massive ($M_\star > 4 \times 10^{10}$ M$_\odot$) SMGs on the main sequence within $2 < z < 3$. At a given SFR, the gas content is roughly consistent with PHIBBS-I, while ALESS SMGs on the main sequence have a higher gas content, perhaps because of the nature of its selection.

(see also Sec. 3.3.3).

Hereafter, we focus on the results of CO (3–2) since the number of galaxies that are detected is larger. For this, our main comparison sample is mainly the results of Genzel et al. [2015] and Tacconi et al. [2017], in which the scaling relation of gas depletion time and molecular gas fractions in general fields was derived, using CO (3–2) measurements.

Apparently, a systematically different correlation (anti-correlation with Pearson's correlation coefficient $r = -0.85$ with a p-value of 0.01) between SFR and $M_{\rm gas}$ is found in protocluster members. Nevertheless, the median SFE is consistent with the average value of PHIBBS samples at similar sSFR values ($\langle$SFE$\rangle \sim 1.8$ Gyr^{-1}) (Fig. 3.6). Further discussions related to this are presented in Sec 3.3.2, but the apparent anti-correlation may be mainly due to two populations : (i) AGN-dominated HAE5 and (ii) less massive galaxies among the detected galaxies, i.e., HAE9 and HAE16 with large velocity widths, in which the uncertainties of SFR from Hα is expectedly larger than those in other cases. Additionally, such anti-correlation (or no correlation) is observed in the ALESS SMGs on the main sequence with less significance ($r = -0.43$ with p-value=0.13). While it is hard to conclude, if this is real, the difference might hint at an environmental effect of galaxy evolution during cluster formation.

Interestingly, all galaxies in CO (3–2) detection are also detected in MIPS 24 μm (Fig. 3.2-3.5). It may be understood by the natural correlation between the total ISM content (traced by CO (3–2)) and star-forming activity (traced by 24 μm) (= KS relation). The MIPS 24 μm emission at this redshift traces the rest-frame 7.7 μm and 6.2 μm polycyclic aromatic hydrocarbon (PAH) features (for the main sequence galaxies) which trace the star forming activity of the galaxy (Lagache et al. [2004]). However, the 24 μm flux might be also tracing the warm dust component heated by an AGN (Rigby et al. [2008]). HAE5 with a broad-line AGN signature (Tanaka et al. [2011]) is an example for this. In a place of intense radiation field, for example, the (compact) galaxies with high IR luminosity (i.e., starbursts) may weaken the reliability of 24 μ for tracing star forming activity (e.g., Elbaz et al. [2011]). Also, low metallicity environment may weaken the 24 μm flux where a hard radiating field exist (e.g., Shivaei et al. [2017]).

3.2.4 Gas fraction

By combining the gas measurement and stellar content, we derive the gas fraction ($f_{\rm gas} = {\rm M}_{\rm gas}$ / (${\rm M}_{\rm gas}$+${\rm M}_\star$)) of the galaxies. The average value of the gas fraction is $\langle f_{\rm gas}\rangle = 0.55 \pm 0.07$ for

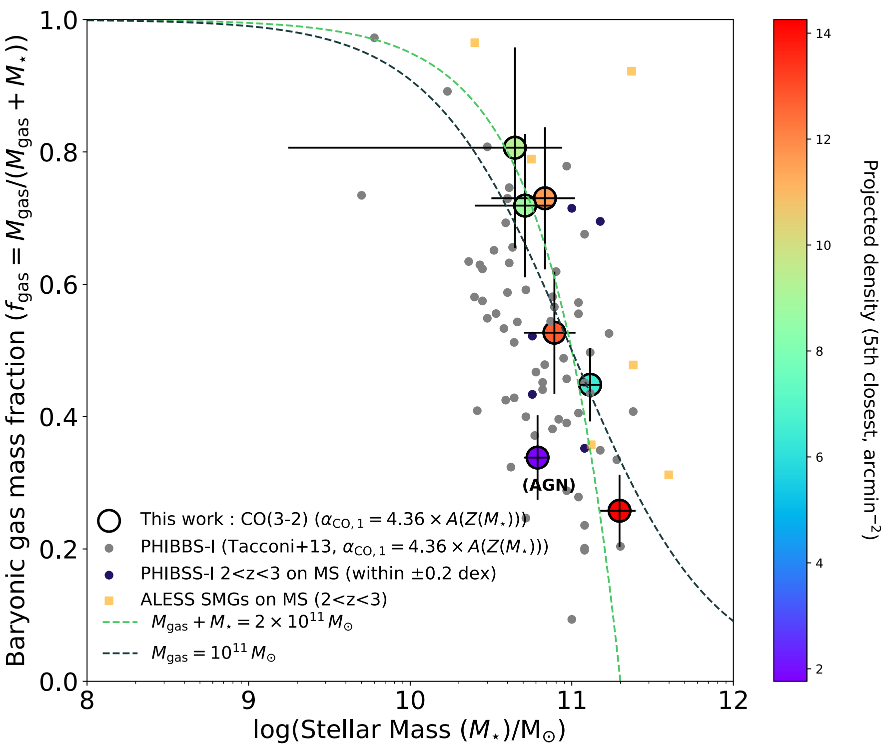

Figure 3.7: Gas fraction ($f_{\rm gas} = M_{\rm gas}/(M_{\rm gas} + M_\star)$) as a function of stellar mass ($M_\star$) colored by local density (defined by the distance from the 5th closest HAEs). Modified from Lee et al. [2017]. The average gas fraction is consistent with field main-sequence (MS) galaxies (e.g., PHIBBS-I from Tacconi et al. [2013], ALESS from Hodge et al. [2013]) with a marginally large scatter (see also Fig 3.8). The trend in gas fraction with increasing stellar mass is similar to field galaxies. Galaxies without a signature of AGN show a tentative trend of decreasing gas fraction with increasing local density which needs to be confirmed with larger samples.

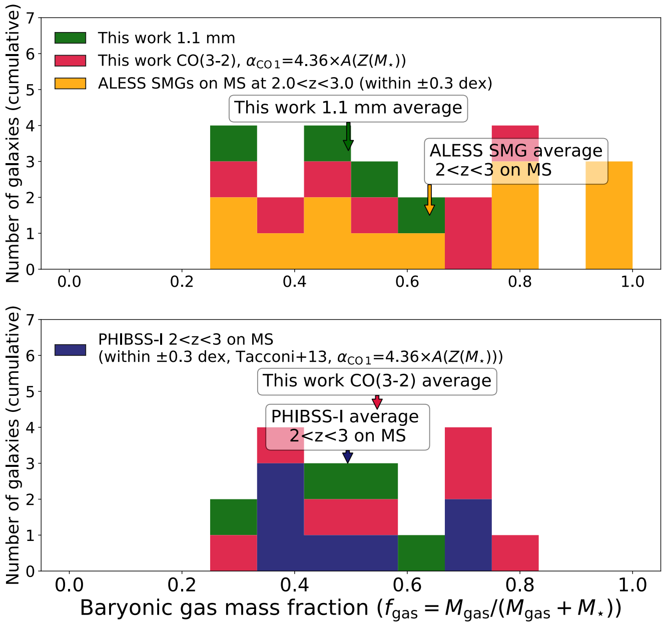

Figure 3.8: Histogram of gas mass fraction for the massive ($> 4 \times 10^{10}\, M_\odot$) main-sequence galaxies at $2 < z < 3$. We plot the distribution of the ALESS SMGs on the top panel and that of PHIBSS-I on the bottom. In general, the distribution of gas fraction (scatter $\sigma_f = 0.20$ for CO (3–2) and $\sigma_f = 0.12$ for 1.1 mm) and the average ($\langle f_{\rm gas} \rangle = 0.55 \pm 0.07$ for CO (3–2) and 0.50 ± 0.06 for 1.1 mm) of the protocluster galaxies are consistent with PHIBBS-I ($\langle f_{\rm gas} \rangle = 0.49 \pm 0.05$, $\sigma_f = 0.14$). The ALESS SMGs on the main sequence have a slightly larger scatter ($\sigma_f = 0.24$) and average ($\langle f_{\rm gas} \rangle = 0.64 \pm 0.07$). SMGs have such slightly high values, perhaps because of the selection effect.

CO (3–2) and 0.50 ± 0.06 for 1.1 mm, and the values are roughly consistent with each other.

The gas fraction strongly depends on the stellar mass, which is also found in the PHIBBS-I sample (Fig. 3.7). Such a mass dependency of gas fraction may be explained by the gas regulation by the mass dependent feedback and/or the gas accretion efficiency as previously addressed in cosmological hydrodynamical simulations (e.g., Fig.11 in Tacconi et al. [2013] which uses Davé et al. [2011]). However, Fig. 3.7 is also consistent with the gas mass fraction spanning the entire range, which may be originated from the stochastic nature of inflow and star formation; after all, the gas depletion time is short for any coherent evolutionary scenario.

For further discussion, we apply the mass and redshift cut for the sample of PHIBSS-I and ALESS SMGs particularly for those on the massive ($> 4 \times 10^{10}\,M_\odot$) main sequence at $2 < z < 3$. The restriction gives only 7 galaxies for comparison in the PHIBBS-I sample, we find that the average gas fraction does not differ ($\langle f_{\rm gas,PHIBBS-I,MS} \rangle = 0.49 \pm 0.05$) (bottom of Fig. 3.8). The PHIBBS-I results are consistent with other studies on the main-sequence galaxies (e.g., Magdis et al. [2012]; Saintonge et al. [2013]; Sargent et al. [2014]; Scoville et al. [2014, 2016]; Decarli et al. [2016a]; Schinnerer et al. [2016]). ALESS SMGs on the massive main sequence at $2 < z < 3$ (total number of 13) appear to have a slightly higher mean value ($\langle f_{\rm gas} \rangle = 0.64 \pm 0.07$) (Fig. 3.8 top) but is nevertheless consistent within an error.

3.3 Discussions

3.3.1 Reasons for unexpected non-detection

There are several reasons that may apply for the non-detection. Galaxies without 1.1 mm, but with CO (3–2) detection, are HAE4, HAE5 and HAE16. Another sub-group for non-detection is galaxies with high SFR. This includes, massive galaxies with $M_\star > 10^{11}\,M_\odot$ (HAE1, HAE2) and less massive galaxies with high SFRs (HAE12, HAE13). If the normal KS-relation apply, they may have been detected. In contrast, recent observations that reported the detection of the massive main-sequence galaxies (e.g., Decarli et al. [2016b]; Tadaki et al. [2017]). We discuss as below for potential reasons for non-detection.

- AGN-dominated galaxies (HAE1 (radio galaxy 4C23.56) and HAE5) : there may be a significant contribution from AGN so that the intrinsic SFR may be smaller than the estimated SFR. The AGN-dominated galaxies may be intrinsically gas-poor systems because of the AGN feedback, i.e., energetic outflows blowing out the gas content (e.g., Cicone et al. [2014]). HAE5, detected only with CO(3-2), has one of the lowest gas contents and gas fractions. Since the radio galaxy has gigantic bipolar radio lobes associated with the X-ray emissions (Blundell & Fabian [2011]), another possibility is the lack of a 'cold' phase gas, such as that traced by cold dust (i.e., $T_{\rm d}$=25 K) and low-J CO emissions that we observed, owing to a strong radiation field heated by the central AGN.

- Intrinsically smaller $M_\star$ and SFR (HAE2) : from our newly obtained AO-data, we found that the galaxy may be gravitationally lensed. The intrinsic stellar mass (and SFR) may be much less than expected from the seeing-limited data (I. Tanaka et al. in preparation).
- Extended low surface brightness dust component (HAE4)? : the non-detection in 1.1 mm with CO(3-2) detection might suggest a lower surface brightness in the dust continuum, which is also discussed in Decarli et al. [2016b] for a galaxy that has no dust but is detected in CO. Because HAE4 has greatly extended Hα emission compared to CO (see Fig. 3.2), the dust might also be extended and diffuse. It is unlikely from a general point of view, however, that local U/LIRGs as high-z analogs (in terms of IR-luminosity) have a compact dust component with high surface brightness (e.g., Sakamoto et al. [2013]; Saito et al. [2015]) compared to CO emissions. Future observation is necessary to confirm such populations.
- The lack of sensitivity (HAE16) : HAE16 is observed at the edge of the FoV at Band 6, and the sensitivity was not sufficient to detect dust continuum, given the CO (3–2) detection.
- Lower metallicity for low stellar mass galaxies? : HAE12[†] and HAE13 have high SFR but in the relatively lower mass ($< 10^{10}\,M_\odot$) regime. The gas may be CO-dark in terms of the effect of photodissociation in the low-metallicity regime. The dust-based calibration might be no longer valid. Otherwise, they are gas-poor systems with high SFE.

All the potential possibilities listed above need to be checked with future observations with increased depth and higher resolution to confirm the diversity of cold gas properties of the protocluster members.

Our findings also present a caution regarding general expectations for the main-sequence galaxies. With the variety of potential reasons for unexpected non-detection of the protocluster galaxies on the main sequence, 'some universality' of the main sequence may have to be

---

[†] Additionally, we note the galaxy is in the close vicinity of the radio galaxy (offset $\sim$ 25 kpc physical size). The galaxy might have encountered a strong feedback from the AGN, for which we need additional observations.

carefully re-checked through observations. There is a wide range of gas content and SFR with different masses.

3.3.2 Additional adjustment in dust extinction?

For our prescription of the mass-dependent extinction correction (Garn & Best [2010]) on SFR, we need to carefully consider whether the corrected SFR from Hα is accurate.

We attempted to measure SFRs for HAEs using JVLA, where the radio flux can be used as an extinction-free measurement of SFR. It has resulted in only one secure detection (Appendix C)[‡]. The SFR estimate from the radio for HAE9, which has the most bright 1.1 mm component, is consistent with star formation rate derived from Hα, when we assume $\alpha = -0.7$ and typical radio/FIR correlation (Condon [1992]). This suggests the treatment of the dust extinction is well-behaved even for a galaxy that is affected by dust-extinction most significantly.

Nevertheless, the radio observations are also limited by the detection number and have a significant scatter with the uncertainty in the radio spectral index. Further investigation need to be conducted in future studies and is beyond the scope of the Dissertation.

Our best conjecture therefore, for the intrinsic star-formation rate within this paper is the use of SFR(Hα,corrected), while considering the potential uncertainty for the extinction correction.

3.3.3 Validity of using Galactic conversion factor

In high-mass regime of typical star forming galaxies (i.e., on the main sequence), the "Galactic" CO(1-0)-to-H_2 conversion factor (e.g., Dickman et al. [1986]; Daddi et al. [2008, 2010]; Tacconi et al. [2013]; Genzel et al. [2015]) has been often used for measuring gas from CO line. The U/LIRG-like conversion factor $\alpha_{\rm CO} = 0.8\,M_\odot\,(\rm K\,km\,s^{-1}\,pc^2)^{-1}$ is used for galaxies above the main sequence at a high redshift such as SMGs (e.g., Solomon & Vanden Bout [2005]; Yun et al. [2015]).

The mass consistency from dust continuum and CO (3–2) favors $\alpha_{\rm CO} = 4.36$ (M$_\odot$ (K km s^{-1} pc^2)$^{-1}$) as the first order for the protocluster galaxies on the main sequence. If we adopt the U/LIRG-like conversion factor, it yields larger inconsistencies between different estimators

---

[‡] We note that the arguments related to the detection of JVLA in Lee et al. [2017] was based on old calibration and imaging, which used `clean` without self-calibration, while here we re-analyzed the data by applying the updated VLA pipeline version, using `tclean` after self-calibration, which still need sophisticated analysis (see Appendix C).

since the gas mass derived from CO is smaller than dust measurement by a factor of 2-5. To compensate this, if real, this would require a dust temperature higher by a factor of 2-5 from the gas mass recipe of Scoville et al. [2014, 2016]. Such a high dust temperature is unlikely at the observed resolution which traces gas in global scale. Otherwise, it would be extremely compact (< 1 kpc) in size.

Future observations are necessary for larger number to test our findings, on the validity of adopting the "Galactic" conversion factor. This may be done with (i) larger samples (with a larger mass range) and (ii) different measurements (e.g., multiple-J CO line or a simpler optically thin line such as [CI]).

Before closing this section, we list several considerations for the adoption of the conversion factor.

- Large line width : we find that more than two-thirds of galaxies have velocity widths > 300 km s^{-1}, i.e., very disturbed similar to on-going mergers observed in local U/LIRG (see also Chapter 4). In this case, CO emission might be optically thin, requiring the conversion factor to be lower than the assumed value. We note, however, that in Daddi et al. [2010], six BzK galaxies detected with CO(2-1) have large FWHM (> 500 km s^{-1}), and the authors used the "Galactic" value ; one of the six galaxies is possibly a rotating disk in the velocity-position diagram, while the others cannot be directly tested to determine whether they are rotating.

- Uncertainties in the contribution of atomic content : our assumption is that the molecular gas is dominant in high-z galaxies since the mean H_2 column densities and ISM pressure are expectedly higher than the local values (e.g., Obreschkow et al. [2009]). Furthermore, as a protocluster is similar to a group-like environment (e.g. Toshikawa et al. [2014]), shock heating might prevent HI gas from accreting onto a galaxy (e.g., Appleton et al. [2013]) or the neutral gas may be stripped while galaxies form a common halo (e.g., Verdes-Montenegro et al. [2001]) leading to a lower HI content compared to that of the fields. In addition, the gas accreted particularly onto massive galaxies around high-z overdensities may be recycled gas (Emonts et al. [2016]).

- Gas mass from CO always higher than that derived from 1.1 mm : we find a systemic offset between CO-based and dust-based measurements, and a similar trend was previously reported from several studies (e.g., Genzel et al. [2015]; Decarli et al. [2016b]). Genzel et al. [2015] argued that referring to the true dust temperature (at least from two bands) and correcting for metallicity would improve the inconsistency. It might also be due to the more extended and diffuse nature in 1.1 mm, where the extended emission below the surface brightness limit is missed (see also Sec. 3.3.1).

3.3.4 Gas content in a protocluster

Our finding for the gas content on protocluster members is that galaxies on average, have similar gas fractions of main-sequence field galaxies (see Fig. 3.7 and 3.8). The ALESS SMGs on the main sequence may have slightly higher gas fractions, but they are consistent within errors. If the larger fraction is real for ALESS SMGs, this may be due to by its selection, i.e., being dusty therefore gas rich. In either case, the gas fractions for all of the high-z galaxies are higher than the local value (of star forming galaxies, $f_{\rm gas} \sim 0.08$) at a given stellar mass (e.g., Saintonge et al. [2013]; Tacconi et al. [2013]).

Next, we estimate the cosmic gas density of the protocluster (Fig. 3.9). The survey area is 14 comoving Mpc^2, and we adopted a ~20% sensitivity region (a radius of 37″) with our 4-pointing observations. If Δz is restricted only to the sources detected in CO (3–2), which results in the range of $2.478 < z < 2.487$ ($\sim$ 11 comoving Mpc), then the cosmic gas density is estimated as $\rho_{\rm gas,4C23.56} \sim 5 \times 10^9\, M_\odot\, {\rm Mpc}^{-3}$.

This is $\sim 22\times$ higher than the upper limit of the general field, i.e., HUDF at $z = \langle 2.6 \rangle$ (Decarli et al. [2016a]) or other previous surveys (Walter et al. [2014]; Keating et al. [2016]) and any other models (e.g. Obreschkow & Rawlings [2009]; Lagos et al. [2011]; Sargent et al. [2014]). Note that we applied the same $R_{13} = 2.38$ and the uniform conversion factor $\alpha_{CO\,1} = 3.6$ to compare with the result of Decarli et al. [2016a]. This effectively changes the total value of $\rho_{\rm gas,4C23.56}$ by ~15%.

Provided a recent simulation with an expected size of the protocluster (Chiang et al. [2013]), we could perform a more conservative derivation assuming a wider redshift range. We performed calculations by assuming the line-of-sight distance of the protocluster to be set by the narrow-band filter coverage ($\Delta z \sim 0.03$, ~40 comoving Mpc). The gas density becomes $1 \times 10^9\, M_\odot\, {\rm Mpc}^{-3}$, which is still a factor of six higher than the result of general fields. A more conservative method is to derive the gas density by applying a U/LIRG-like conversion factor for all detected sources, lowering the gas density by a factor of 4.5, which can be regarded as the *lower limit* of the gas density of the protocluster, close to the upper limit of the general field.

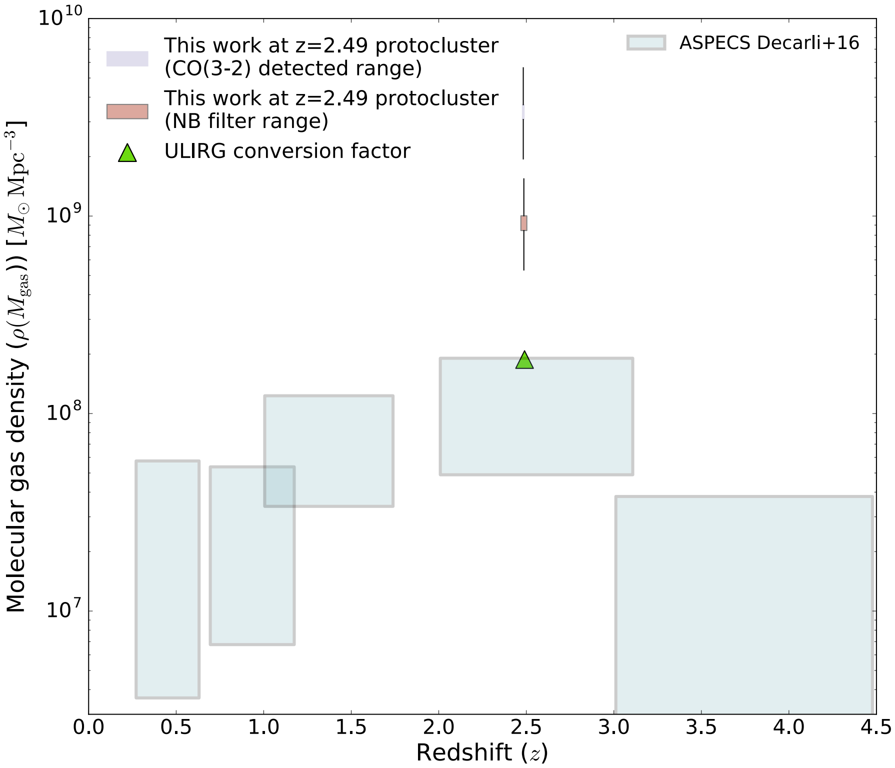

Figure 3.9: Cosmic gas density for the z=2.49 protocluster (this work) overlaid on the recent ALMA studies of general field, HUDF-S (Decarli et al. [2016a]) (see the text on details of the calculation to match both results). We plot three different estimations (i) using CO(3-2) redshift range ($\Delta z \sim 0.01$), (ii) using NB filter redshift range ($\Delta z \sim 0.03$) and (iii) applying U/LIRG conversion factor ($\alpha_{\rm CO} = 0.8$ for the case (ii). The black error bar is estimated by taking into account Poisson uncertainties (Gehrels [1986]).

Although it may not be fair to compare our results with the results of Subaru/MOIRCS, which has a different survey size ($\sim$ 3000 comoving Mpc^3), we note that protocluster 4C23.56 is also an order of magnitude higher in the cosmic star-formation-rate density (SFRD) and (3-9) times higher in the stellar mass density ($\rho_\star$) compared to the results presented in Madau & Dickinson [2014] with the detection of 25 HAEs.

We barely infer the causality of these observational results. The higher gas density may simply be due to the higher number density of the galaxies at a given volume, which is inferred from the high SFRD and $\rho_\star$. Alternatively, the reason for the galaxy overdensity in the protocluster might be the higher gas density within the volume. The former case can be simply explained by the number density of HAEs of protocluster being threefold higher than that of the field (Tanaka et al. [2011]) and the fact that the average gas fraction is similar to the field.

However, the estimated gas density is the lower limit since we only perform calculations for the detected sources. It is uncertain whether galaxies at a lower mass regime have a larger amount of gas, and this issue cannot be clarified with the current method (or current calibration). We did find an extremely large amount of gas ($f_{\rm gas} > 0.7$) in three of the galaxies, HAE9, HAE10 and HAE16, which are in the lower massive bin in our detected sample. While noting that statistical significance is not sufficiently high to reject the opposing case given the size, the scatter of the gas fraction (observed in CO (3–2)) is 13% higher than that of the PHIBBS-I sample. Further higher sensitivity observations or another tracer of the so-called CO-dark gas tracers would clarify this issue.

3.3.5 Environmental effect during the cluster-forming epoch?

Detection in the densest region

Among seven CO-detected galaxies, five HAEs are located in the region of highest surface density. The surface galaxy number density is measured by using the distance to the 5th nearest neighbor (Fig. 2.4 and see also the color trend for $f_{\rm gas}$ in the local density in Fig 3.7).

Given the overdensity of the protocluster, i.e., the number density of HAEs within the protocluster is three times larger than general fields (Tanaka et al. [2011], Tanaka et al., in preparation), this suggests that the CO (3–2) (or dust) detection of the galaxies might depend on (but not necessarily) the environment, which is nevertheless a very marginal trend. Umehata et al. [2015, 2017] argued that there is a concentration of the 1.1 mm continuum sources in the node of pro-

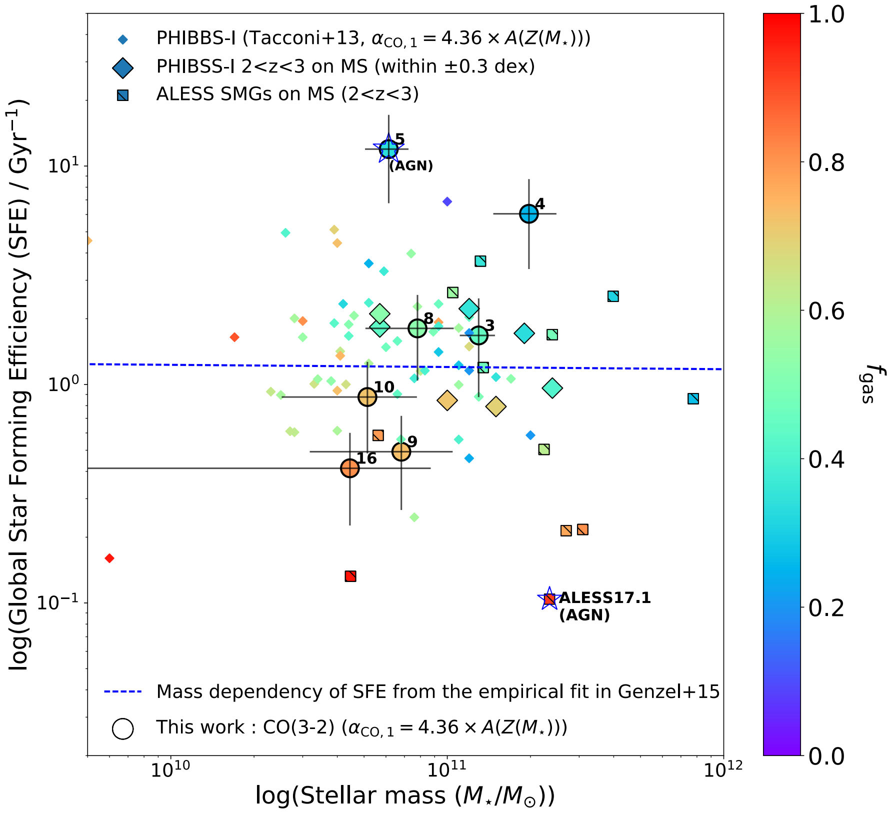

Figure 3.10: Stellar-mass dependency of global star forming efficiency. Although the probed range is still narrow, a positive correlation between M⋆ and SFE is found for the protocluster galaxies, in contrast to the result of Genzel et al. [2015] for the main-sequence galaxies. The empirical fitting formula presented in Genzel et al. [2015] shows a small dependency (with a power of 0.01) on stellar mass in the depletion time scale (i.e., a power of -0.01 for SFE indicated by the dashed line) compared to the larger contributions of the deviation from the main-sequence sSFR and the redshift evolution. The color scheme shows the f_{gas} for individual galaxies. A star symbol indicates the existence of AGN.

tocluster SSA22, where filamentary structures meet. If it also applies to our case, the detection in the region of highest surface density may be mirroring the preferential place of gas detection within certain large structures of the protocluster, e.g., projected filaments or the node, where the gas is infalling or being accreted. For further comparison, recent related surveys for a cluster at lower redshift of $z = 1.6$ pointed out that, CO lines are detected on the outer regions of the clusters, which might be related to gas stripping or mergers (Hayashi et al. [2017]). The different trend in different cosmic age may be arguing potential evolution that might work for the dense regions, within $\sim$ 2 Gyr (from $z = 3$ to $z = 1$). We may be witnessing the very intermediate stage of such transition at z=2.49, where an intensive accretion and gas stripping (or mergers) both contribute to shape galaxies in the protocluster; our finding shows the average gas fraction is consistent with field value with a (tentatively) larger scatter. Considering all, future mapping observations of gas content is necessary for larger surveys to confirm.

Compared to the averaged property of the protocluster, five galaxies detected in CO (3–2), those without significant evidence of AGN, are again divided into two populations : (i) a vast amount of gas with a relatively low mass ($f_{\rm gas} \gtrsim 0.7$, $4\times10^{10} < M_\star/M_\odot \lesssim 1\times10^{11}$) in relatively less dense regions (HAE9, HAE10, and HAE16) and (ii) more massive galaxies ($\gtrsim 1 \times 10^{11}$) with lower $f_{\rm gas} \lesssim 0.5$ in denser regions (HAE4 and HAE8).

Comparison with previous studies

To discuss further, we compare the star formation scaling relation of the field populations in Genzel et al. [2015], Scoville et al. [2016] and ALESS SMGs. We note that our targets and control samples (PHIBBS-I, ALESS SMGs on the main sequence) are within a narrow range near the main sequence.

From recent extensive studies, a scaling relation of the depletion time ($\tau_{\rm depl.}$) (or of the (global) SFE, which is the inverse of $\tau_{\rm depl.}$) is empirically derived. Here, we refer to the work in Genzel et al. [2015], which is one of the pioneering works that have been conducted. The gas depletion time can vary with the redshift (z), offset from the main sequence Δ(MS) and dependency of stellar mass ($M_\star$).

By excluding AGN (HAE5), our results give a positive correlation between $M_\star$ and SFE (Pearson's correlation coefficient (in log scale) = 0.89 with a p-value of 0.02). This is in contrast to the empirical fitting in Genzel et al. [2015] and Tacconi et al. [2017], and the PHIBBS-I galaxies that show a weak negative (or flat) correlation between $M_\star$ and SFE. One may argue that such an apparently different correlation from the general field is only due to the sample bias and is still explained within the scatter of the PHIBBS-I sample. We cannot reject such argument with the current data set. This issue can only be investigated through larger and deeper observations by collecting statistically large numbers.

Suggested picture and future aspects

The correlations shown in the previous sections suggest some insight into massive galaxy evolution and the properties of dark matter within a high-z protocluster.

As discussed in Genzel et al. [2015] (section 4.3), the global depletion time can be related to dark-matter properties in the framework of disk formation within a dark-matter-dominated universe (Mo et al. [1998] see also eq.(24) in G15); in other words, SFE can be expressed as a function of several parameters including the baryons' angular-momentum parameter (λ), galaxy's (local) star-formation efficiency (η), dark matter concentration parameter (C), and Hubble parameter ($H(z)$). The similarity of the averaged physical properties for the galaxies on the main sequence may be due to two dominant factors between the balance of $H(z)$, i.e., redshift dependency, and perhaps η, i.e., local star-forming activity. The mass dependency of SFE (at an almost constant sSFR) suggests that additional (or different) physical processes, which are perhaps related to the local environment, may be necessary to explain this phenomenon.

Halo concentration is higher in denser environments and increases in later times (Bullock et al. [2001]) and a (proto)cluster is a place where galaxy evolution proceeds earlier (e.g., having a quenched or passive population at the center in advance ; Kurk et al. [2009]; Strazzullo et al. [2013]; Koyama et al. [2014]; Cooke et al. [2016]). Considering the above, the halo concentration parameter of the most massive galaxies in denser regions might be higher than that of less massive galaxies in less dense regions such that related to the observed mass dependency, though the scenario should be tested with future observations.

Another test scenario is on the change of dark matter fraction (and angular momentum). The total baryonic mass seems to be almost constant for detected galaxies, a green dashed line shown in Fig. 3.7, and the massive galaxies tend to have narrower line widths (e.g., HAE16 (less massive) vs HAE8 (more massive), though, not convincing for all of the galaxies). It further needs additional investigation on the time scales of these changing parameters by both observations and simulations. A quantitative estimation of all of these contributions may not be simple, but it is certainly required in future observations for understanding the environmental effect in galaxy evolution at high z.

The proposed picture, however, may be different in galaxies with stellar mass less than 10^{10} $M_{\odot}$. We have no detection in less-massive galaxies that needs to be investigated via deeper observation. Thus far, there is little evidence that clarify the change of the scatter of the main sequence in a different environment (e.g., Peng et al. [2010]; Koyama et al. [2013]; Darvish et al. [2016]). But recently, Hayashi et al. [2016] reported a larger (upward) scatter of main-sequence galaxies in the low-mass galaxies ($< 10^{9.3}$ $M_{\odot}$) at the $z = 2.5$ protocluster, which is in fact similarly seen in our sample (I. Tanaka et al., in preparation; see Fig. 2.1).

3.4 Conclusion

In this chapter, we investigated the gas content of HAEs that are typical star-forming galaxies on the main sequence associated to protocluster 4C23.56 at z = 2.49. To derive the gas content, we conducted CO (3–2) (Band 3) and 1.1 mm ($\lambda_{\rm rest} \sim 385$ μm) dust continuum (Band 6) observations with ALMA toward the protoclusters for which panchromatic studies are available.

From the ALMA CO (3–2) and 1.1 mm observations, our results are as follows.

1. We obtained seven CO (3–2) and four 1.1 mm dust continuum detections. All four 1.1 mm detections are detectied in CO (3–2). While the parent galaxies have a stellar mass range greater than three orders of magnitude ($\log(M_{\star}/M_{\odot}) = [8, 11.5]$), the detected sources are all massive ($M_{\star} > 4 \times 10^{10}$ $M_{\odot}$) on the star-forming main sequence.

2. Gas mass was derived using the “Galactic” conversion factor with additional correction for the metallicity dependence of the CO conversion factor using the method described in Wuyts et al. [2014] and following the analysis presented in Genzel et al. [2015] for CO (3–2), which yields a consistent value derived from dust-based calibration using Scoville et al. [2016].

3. The HAEs detected in either CO (3–2) and 1.1 mm have on average, similar gas content to those of main-sequence galaxies in general fields. The massive HAEs ($M_{\star} > 4 \times 10^{10}$ $M_{\odot}$) have a gas content in the range of (0.3-1.8) $\times 10^{11}$ M$_{\odot}$ and a median gas fraction $\langle f_{\rm gas} \rangle = 0.53 \pm 0.07$ for CO (3–2) and 0.50 ± 0.06 for 1.1 mm measurement. Including our work, the high-z massive galaxies ($2 < z < 3$) on the main sequence that were considered (Tacconi et al. [2013]; Scoville et al. [2016]; Hodge et al. [2013]; da Cunha et al. [2015])

all possess a higher gas content than those of local star-forming galaxies, regardless of their environment.

4. The cosmic gas density of high-z protoclusters was measured for the first time. Using either the redshift range of CO (3–2) ($\Delta z \sim 0.01$) or NB filter ($\Delta z \sim 0.03$), which is comparable with the predicted size in simulations (e.g., Chiang et al. [2013]), and the survey area of Band 3, we found an enhancement of cosmic gas density, $\rho_{H_2} \sim (1-5) \times 10^9\, M_\odot\, \mathrm{Mpc}^{-3}$ that is already a factor of 6-22 higher value only with the detection than the upper limit set by the recent survey toward HUDF (Decarli et al. [2016a]) with the same assumption of conversion factor and line ratio.

5. We found that $f_{\rm gas}$ decreases with increasing stellar mass, as observed in control samples. However, $f_{\rm gas}$ might also change with surface galaxy number density which need future confirmation. Galaxies with a higher gas fraction ($f_{\rm gas} > 0.7$) are less massive ($4 \times 10^{10} < M_\star/M_\odot \lesssim 1 \times 10^{11}$) in regions with relatively low surface density, while galaxies with $f_{\rm gas} \lesssim 0.5$ are more massive ($\gtrsim 1 \times 10^{11}$) and in regions with higher surface density.

6. Massive main-sequence galaxies in the protocluster may be evolving under the effect of the specific environment. A systematically different correlation between SFE versus stellar mass might be the combined result of a higher gas volume density and the non-negligible contribution of dark matter imprinted in the surface number density (and CO line widths), but quantitative assessment should be performed in future studies to confirm this hypothesis.

The sample size is still small to discuss statistical significance as a general picture of galaxy evolution. And the different methods used in the derivation of parameters other than $\mathrm{M_{gas}}$, i.e., SFR and $M_\star$, when comparing field samples. Therefore, larger surveys are necessary to probe a wide range of characteristic environments (e.g., diverse galaxy number densities) and redshifts that can be constructed with the same analysis tools. Deeper observations are also necessary to investigate the evolution of less massive galaxies and their connection to the probed massive galaxies on the protocluster.

Galaxies themselves cannot close the Universe.

J. Richard Gott, III

Chapter 4

Gas kinematics of Hα emitters

A main discussion of this chapter regarding the gas kinematics of Hα emitters in the $z = 2.5$ protocluster will be submitted to ApJ.

In this Chapter, we investigate the gas kinematics in Hα emitters, i.e., actively star-forming galaxy population in $z = 2.5$ protocluster 4C23.56, using ALMA and address, for the first time, the kinematical properties and connection with local populations.

4.1 ALMA CO (4–3) observations

We performed CO (4–3) observations (ID : #2015.1.00152.S, PI : Minju Lee) at ALMA band 4 towards 16 HAEs (and we also targeted [CI] (1–0) under the same project ID, see Appendix C for the observation set-up). In total, 38 and 39 antennas were used with the baseline length $L_{\rm baseline}$ between 15 m and 3.1 km (C40-6) and total on-source time, $T_{\rm integ}$, was 2.7 hours with two-pointing observations of 16 HAEs (Figure 4.1). The set-up for the correlator was four spectral windows (SPW), two of which were set to each sideband. One SPW in which the redshifted CO (4–3) would be observed, was set to have a channel width of 7.82 MHz ($\sim$ 17.7 km s^{-1}) within the bandwidth of 1.875 GHz in the FDM. The remaining three SPWs were observed with a 2.0 GHz bandwidth and 15.6 MHz resolution in the TDM to cover the dust continuum at 2 mm. We observed J2148+0657 and J2025+3343 as a bandpass and flux calibrator, respectively. Phase calibrator was J2114+2832.

We used `CASA` (McMullin et al. 2007) version 4.7.0 and 5.1.0 for the calibration of visibility data and imaging, respectively. Calibration processes were firstly done with the pipeline with the script provided by EA-ARC. We flagged the visibility data additionally to improve the image quality after checking the obtained first images and re-imaged after re-calibrating the visibility data. Images were produced by `CASA` task, `tclean`. The typical noise level in the final image is 0.14 mJy beam^{-1} at 100 km s^{-1}, which is one of the deepest observations that have been obtained for high-z star forming galaxies. The size of synthesized beam is $0''.52 \times 0''.32$.

4.2 Results

4.2.1 Detection of CO (4–3)

Detection criteria

Basic criteria for CO (4–3) detection are similar to those for CO (3–2) detection. The revised criteria for CO (4–3) detection are as follows : (a) a peak flux $\geq$ 3.5 σ; (b) at least two continuous channels including a maximum peak flux channel to have flux $\geq$ 3 σ; (c) a peak integrated

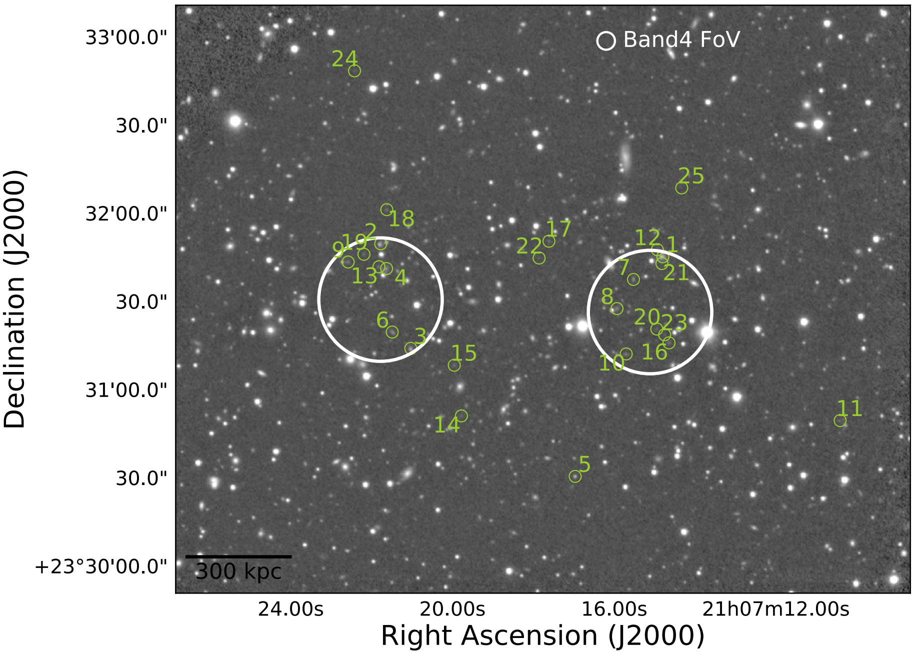

Figure 4.1: The FoVs of Band 4 observations in white circles, overlaid on the background image of the Subaru/MOIRCS Ks band (I. Tanaka et al., in preparation). We targeted 16 HAEs in the CO (4–3) observations using two FoVs; we covered seven HAEs including HAE 2, 3, 4, 6, 9, 13 and 19 in the east FoV, and nine HAEs including HAE 1, 7, 8, 10, 12, 16, 20, 21 and 23 in the west FoV.

intensity S/N $\geq$ 4.5. For the third criterion (c), we examined various channel widths to determine the integrating range that gives the largest S/N. If any two criteria out of three given above are satisfied, we regarded this as a detection. We checked the criteria for three sets of data cubes with different spectral resolutions, i.e., 40, 100 and 200 km/s. We then list the (semi-final) candidates of detection when at least two data cubes in different spectral resolutions satisfy the detection criteria. We also explored the detection processes for the data sets with and without continuum subtraction[*]. The CO (4–3) line detection is confirmed finally after we perform visual inspection based on the 100-km-s^{-1}-resolution data cubes and spectrum fitting.

CO (4–3) line detection

Applying the addressed detecting processes, CO (4–3) lines were detected in 10 HAEs out of 16 targeted. Five HAEs among the total ten were detected in CO (3–2) line as shown in Figure 3.2-3.5, i.e., HAE 3, 7, 8, 9 and 16[†]. The remaining five HAEs are the first detection ever occurred in any CO lines, i.e., non-detection in CO (3–2) and detected in CO (4–3). We explore the nature of the latter five galaxies in the next sections. Figure 4.2 shows the intensity maps and the CO (4–3) spectra (in a velocity bin at 100 km s^{-1}) for detected sources. The reference velocity ($v = 0$) of each spectrum is set to a nominal value of $z = 2.486$ to take it as a representative center of the protocluster.

HAE 8 and HAE 16 are detected very clearly in CO (4–3) line satisfying all the criteria, and their S/Ns of the peak intensity are larger than 8. We make and fit kinematic models of these galaxies, as explained in the following section. The rest of detection satisfies two criteria, i.e., (a) + (c) in the most cases. We "CLEAN" the visibility data down to 2 σ (using `tclean`) for HAE 8 and HAE 16, where the CO (4–3) structure can be easily identified by eye on the "dirty" data cube. Other galaxies are analyzed based on the dirty map.

We measure a flux by taking an aperture radius of $0''.5$, which corresponds to a major axis of the beam. We estimate a line width and a CO (4–3) redshift by fitting the spectrum with a Gaussian model. The estimated FWHM is roughly consistent with the integrating velocity width that gives the highest S/N for each galaxy.

---

[*] By doing so, we can robustly confirm the detection as well as the channel to fit the continuum (within a spectral window) for subtracting the continuum.

[†] Among seven HAEs detected in CO (3–2) line (see Chapter 3), two HAEs are not detected in CO (4–3) line for individual reasons; one galaxy (HAE 4) is undetected perhaps due to the low S/N in CO (4–3) and the other (HAE 5) is located outside of two FoVs of CO (4–3) observations.

We find a few sub-components resolved either in the spectrum or in the velocity-integrated intensity map, for HAE 3, 9 and 23. Such sub-components are detected with the peak integrated flux S/N < 6, or they satisfy only one of the detection criteria, thus, they are "undetected". We also explore the possibility of mergers for these galaxies in later discussions. For galaxies having sub-components, the name with "a" denotes a main (=highest S/N) component (i.e., HAE 9a). The name of sub-components with low S/N but still satisfying the detection criteria is expressed as HAE ID+"b", i.e., HAE 9b. For sub-components without the satisfaction of detection criteria, we assign the name of such sub-component as red or blue (i.e., HAE 3 red).

Consistency between redshifts derived from CO (3–2) and CO (4–3)

We check the redshift consistency determined by using the CO (3-2) and CO (4–3) lines for simultaneous detection (i.e., five HAEs). Except for HAE10, the redshifts are consistent within $\Delta z \simeq \pm 0.003$ (corresponding to $\pm$ 300 km s^{-1} at $z = 2.5$) between the two CO lines, though redshifts are defined as differently in those lines[‡]. The redshifts from the CO (4–3) line in HAE 3, 8 and 16 are almost consistent within a velocity offset of $\Delta v = \pm 200$ km s^{-1}. For HAE 9, CO (4–3) spectrum is blue-shifted by $\sim$ 300 km s^{-1} with respect to its known redshift defined by CO (3–2) and we explore the possibility of a merger of this galaxy. The CO (4–3) line detection of HAE 10 is occurred in low S/N and the inconsistency in the CO redshifts (by $\sim$500 km s^{-1} in velocity) is perhaps owing to the low sensitivity, which need the confirmation.

4.2.2 3D structure and halo mass

We derive a 3D structure of the protocluster, i.e., 2D distribution and velocity offset from to the reference velocity of the protocluster center, to measure the halo mass of the protocluster. Ideally, the whole 3D structure can be drawn from deep spectroscopic follow-up observations. From CO (4–3) and CO (3–2) observations, we have twelve (CO-line) spectroscopic redshifts for HAEs in total. We add additional redshift information from our Hα spectroscopy campaign carried out with Subaru telescope (Tanaka et al. in prep.), although the measured S/Ns of Hα emission in the spectra so far, are low. By combining all of these measurements, we obtain 20

[‡] In our CO (3–2)-based redshift measurement, we used the median frequency of integrating range (to derive the CO (3–2) intensity map), instead of the mean value from fitting with a Gaussian model, in order to consider the unique appearance in spectrum found in the sub-samples of detection, i.e., a double peak or a non-Gaussian spectral distribution that resulted in a failure of (single) Gaussian curve fitting and partly due to low S/N in CO (3–2). See Chapter 3 for more details.

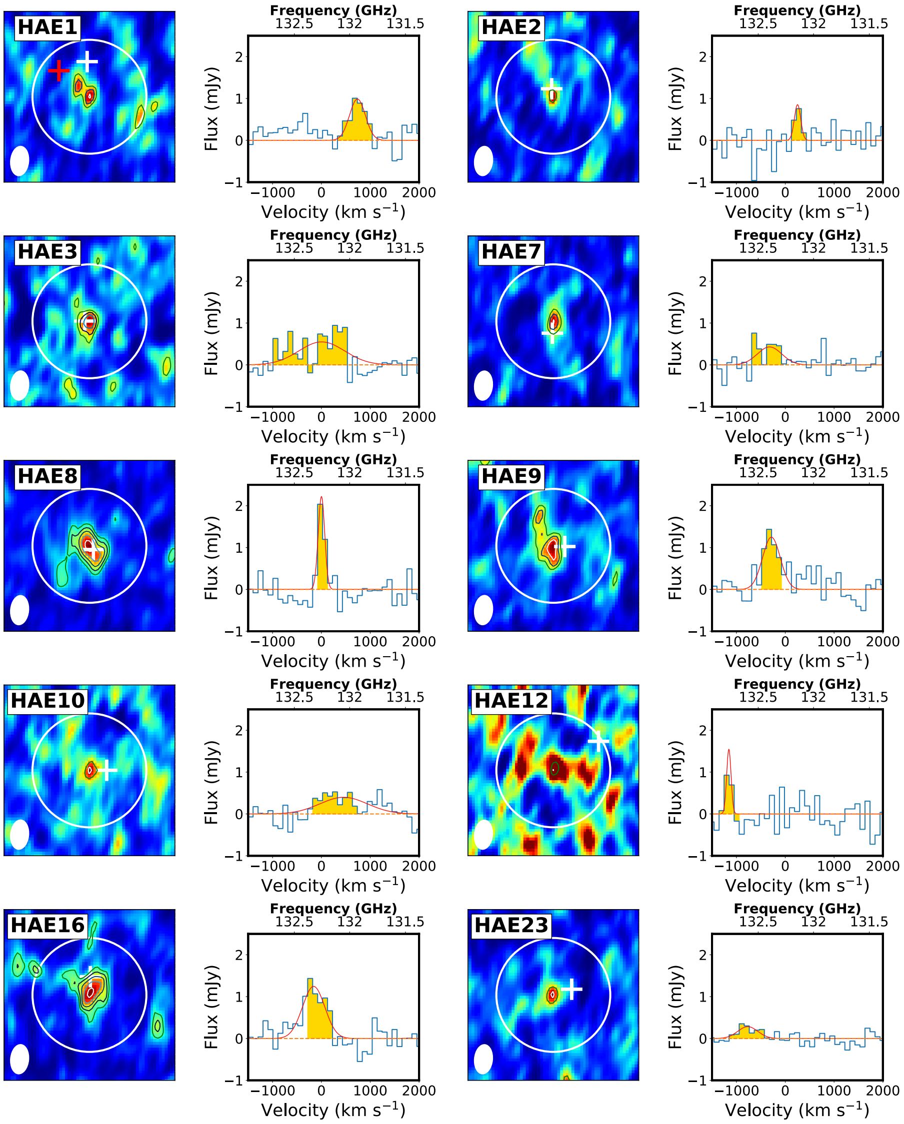

Figure 4.2: A gallery of HAEs with CO (4–3) detection. We show the velocity-integrated intensity map on the left and spectrum on the right for each galaxy. The panel size of the moment 0 (the velocity-integrated intensity map) is 3 arcsec in width and white open circles is with a radius of $1''$. The white filled ellipses indicate the beam size ($0''.52 \times 0''.32$) of CO (4–3) observations. The contours of CO (4–3) intensity are shown in steps of 2σ starting from 4σ, i.e., 4σ, 6σ, 8σ, ... We plot the positions of HAEs in white cross symbols to indicate the consistency between the positions determined by Hα emission and those by CO (4–3) line. For HAE1, we plot the positions of the radio core and Hα emission as crosses in red and white, respectively; the position of the radio core is determined by the JVLA observations in S and C bands, i.e., observing frequencies of 3 GHz and 6 GHz respectively, as presented in Appendix C. The flux shown in the spectrum is in the unit of mJy that is measured within a circle with a radius of 0.5 arcsec, which corresponds to a major axis of the synthesized beam. The yellow region of each spectrum is the integrating velocity range that delivers the highest S/N. We fit the spectrum with a Gaussian model, which is shown in red line. The reference velocity of the galaxy is set by assuming the protocluster redshift $z = 2.486$.

spectroscopic redshifts out of 25 HAEs. A preliminary version of the 3D structure of the protocluster is shown in Fig 4.3. We find two clumps in the east and the west sides of the protocluster that may be loosely connected.

Estimated dark matter halo

We estimate the mass of a dark matter halo of the protocluster by assuming spherically virialized substructures of the protocluster; two clumps in the east and the west sides are shown as large circles with the black solid lines in Fig 4.3. Both regions are two of the densest sections seen in the 2D local density fields (Fig 2.2 and 2.4). We measure the velocity dispersion of the structure based on the redshift information. The east clump includes HAE 2, 4, 9, 13 and 18, while the west clump includes HAE 8, 10, 16, and 23. We adopt the formula used in Finn et al. [2005] that derives the cluster mass from the line-of-sight velocity dispersion ($\sigma_{\rm los}$) and cosmological parameters.

$$M_{\rm cl} = 1.2 \times 10^{15} (\frac{\sigma_{\rm los}}{1000\ {\rm km\,s^{-1}}})^3 \frac{1}{\sqrt{\Omega_\Lambda + \Omega_0 (1+z)^3}} h_{100}^{-1} M_\odot \tag{4.1}$$

We estimate the velocity dispersion, by defining the protocluster redshift z, from the biweight average (Beers et al. [1990]). We find the redshift of the protocluster to be $z = 2.4869$. We can then define a proper velocity of a member galaxy, v_i, from the redshift z_i by using $v_i = c(z_i - z)/(1+z)$ (Danese et al. [1980], see also Ruel et al. [2014] and references therein).

The measured velocity dispersion is $\sigma_{\rm los} = 645 \pm 136$ km s^{-1} as a whole structure of the protocluster. For galaxies with secure detection in both CO (3–2) and CO (4–3), we find $\sigma_{\rm los} = 402 \pm 214$ km s^{-1}. The measured values of velocity dispersion are $\sigma_{\rm los,CE} = 517 \pm 343$ km s^{-1} and $\sigma_{\rm los,CW} = 474 \pm 343$ km s^{-1} for the clump east (CE) and the clump west (CW), respectively. The velocity dispersion of the CW is barely constrained because the number of galaxies is only four.

The estimated dark matter halo mass of the protocluster ($M_{\rm pcl}$) from Eq. 4.1 is an order of $M_{\rm pcl} \sim 10^{14}$ M$_\odot$. For galaxies with both CO (3–2) and CO (4–3) detection, the halo mass is $M_{\rm pcl} = 0.3 \times 10^{14}$ M$_\odot$. We used the redshifts from CO (4–3) and the differences in CO redshifts do not affect the order estimate of the halo mass. The halo masses of CW and CE are $10^{13} - 10^{14}$ M$_\odot$. Based on the theoretical expectation, the progenitors of Virgo-like clusters ($M_{\rm cl} = (3-10) \times 10^{14}\ M_\odot$) or the most massive clusters like the Coma cluster ($M_{\rm cl} > 10^{15}\ M_\odot$) at $z \sim 2.5$

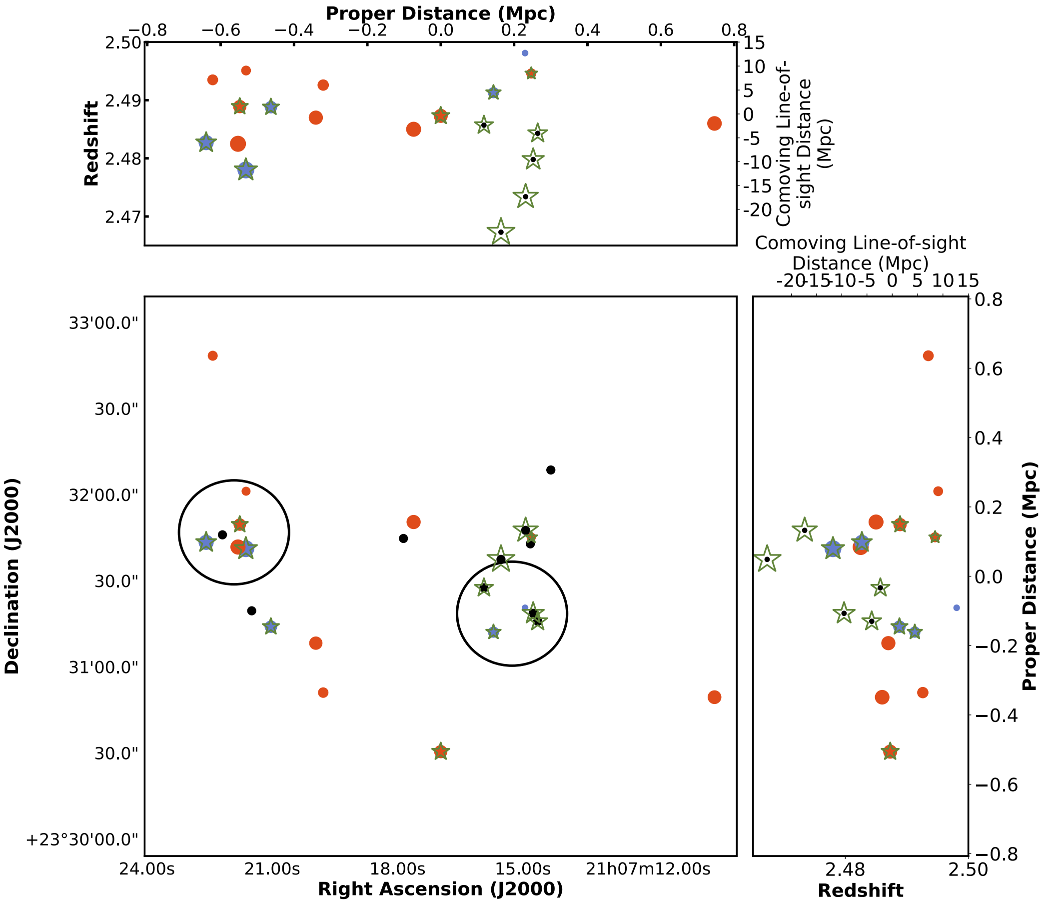

Figure 4.3: Three-dimensional distribution of HAEs obtained by combining the redshift information of CO lines from ALMA observations and Hα emission from Subaru grism spectroscopy. We indicate star markers, red filled circles and blue filled circles for indicating CO (3-2) or CO (4-3) line detection, high S/N spectroscopic Hα emission and low S/N spectroscopic Hα emission, respectively. The remainder of HAEs are plotted in black circles. Different sizes are showing the relative redshift distribution, i.e., a larger symbol indicates a lower redshift galaxy (thus it is 'closer' to us).

have the halo mass higher than 10^{13} $M_\odot$ (Chiang et al. [2013]). Therefore, if the protocluster follows the typical evolutionary track of clusters as expected in simulations, it would become at least a Virgo-like, intermediate mass cluster at $z = 0$ or a more massive one.

Finally, we note that the velocity information should be taken cautiously, keeping in mind that the S/Ns of the Hα spectroscopic data are quite low and some HAEs are also detected marginally in CO (4–3) lines. We add another note of caution related to the assumption for the structure. Although we estimate the halo mass based on the virial theorem and the size of each clump is roughly consistent to the size of the virial radius, the substructure and the protocluster itself may not be virialized yet. Observational studies have shown that the highest redshift young 'virialized' cluster to date is at $z \sim 2.5$ (Wang et al. [2016]), and most overdense regions found near this redshift show no X-ray detection, i.e., no hot halo created by the virial shock. Therefore, the measured mass of the halo is crude estimation to characterize the identified protocluster using the current available data.

4.2.3 Gas disk modeling with GalPaK^{3D}

We model the observed data cubes of HAE 8 and HAE 16 that show the highest S/Ns (>8) in the CO (4–3) intensity maps. These galaxies have relatively smooth velocity gradients, suggesting that they are disk-like galaxies (see Figure 4.4 and 4.5 for moment 1 maps, i.e., the velocity gradient maps of CO (4–3) and Figure B3 and B4 for channel maps in the Appendix B). For these disk-like galaxies, we use public resource of GalPaK^{3D} (Bouché et al. [2015][§]) to estimate the kinematic parameters, for instance, the maximum velocity rotation ($V_{\rm rot}$) and the intrinsic velocity dispersion (σ_0). The code parameterizes 10 free parameters and estimates them by the Bayesian-based Markov-Chain Monte Carlo (MCMC) calculation to fit the data cube. The parameters are the positions, x_c, y_c and z_c , the disk half-light radius, r_e, the total flux, $f_{\rm tot}$, the inclination, i, the position angle, PA, the turnover radius, $r_{\rm t}$, the maximum circular velocity, $V_{\rm max}$, and the one-dimensional intrinsic dispersion, σ_0. We assumed the galaxy structure to be an exponential disk (i.e., the Sérsic profile of $n = 1$), which is a general assumption for the main sequence galaxies, and the velocity structure to be an arctan profile. The simulated galaxy is convolved (in 3D) with the PSF (or the beam size) and the instrumental line-spread function (LSF), corresponding to a spectral resolution.

[§] `http://galpak.irap.omp.eu/index.html`

We show the fitting results using GalPaK^{3D} in Appendix B (Figure B1 and B2). The fitting results are also summarized in Table 4.1. We use these parameters to discuss on HAE 8 and HAE 16.

Table 4.1: Galactic parameters of disk galaxies (HAE 8 and HAE 16)
(Errors include the 68th percentile ranges of the estimated parameters)

	HAE 8	HAE 16
RA (J2000)	21:07:15.936	21:07:14.645
Dec (J2000)	+23:31:27.592	+23:31:15.543
$\log(M_\star)$ [$M_\odot$]	$10.89^{+0.13}_{-0.18}$	$10.64^{+0.30}_{-1.64}$
$\log(M_{\rm gas})$ [$M_\odot$]	$10.93^{+0.05}_{-0.05}$	$11.27^{+0.06}_{-0.07}$
$\log(M_{\rm bar})$ [$M_\odot$]	11.22 ± 0.19	11.36 ± 1.64
SFR (Hα) [$M_\odot$ yr^{-1}]	156±63	76 ± 32
z(from CO (4–3))	2.4855	2.4843
FWHM(CO (4–3)) [km s^{-1}]	146 ± 20	587 ± 40
	Parameters from GalPAK^{3D}	
r_e [kpc]	4.90 ± 0.10	4.23 ± 0.11
$v_{\rm rot,max}$ [km s^{-1}]	251 ± 33	275 ± 19
σ_0 [km s^{-1}]	26 ± 4	119 ± 6
$v_{\rm rot,max}/\sigma_0$	9.65 ± 1.95	2.31 ± 0.20
$v_{\rm circ,max}$ [km s^{-1}]	254 ± 33	322 ± 17
i [degree]	27 ± 4	61 ± 4
PA [degree]	-165 ± 2	12 ± 3

4.3 New CO detection from CO (4–3) observations

We present five HAEs detected in CO (4–3) line, which are the first detection occurred in any CO lines. Most cases are difficult to interpret by one line detection (and without previous CO (3–2) detection), thus we need future follow-up observations to get a higher S/N.

- **HAE 1** : the CO (4–3) line is detected significantly with $\sim 6.5\sigma$, but the CO peak is offset from the radio core and the Hα peak by $\sim 0''.7$ and $\sim 0''.6$, respectively (see Fig 4.2). The direction of the CO (4–3) peak from the radio core is parallel to that of the radio lobes. The CO (4–3) line is also redshifted than the reference velocity defined from the redshift the radio galaxy, suggesting an association with a potential outflow or a radio jet. In this respect, the CO (4–3) emission may be associated with either a radio jet or a halo component of the radio galaxy. We need to observe this galaxy with higher sensitivity.

- **HAE 2** : the CO (4–3) line in HAE 2 is detected at 5 σ level in the intensity map. There is a signature of galaxy–galaxy lensing in our recent AO image, an arc-like structure (Tanaka et al., in prep.). The stellar mass of the galaxy may be less massive than the 'observed' mass. The follow-up observations of CO lines are desirable for more robust detection and comparison of such a unique (and less-massive) galaxy with other massive population.

- **HAE 7** : the CO (4–3) spectrum has a peak flux with S/N$\sim$ 3.5 and the integrated flux with S/N$\sim$ 6. The detection of CO (4–3) in HAE 7 is unique, since the galaxy is located well below the main sequence defined at $z = 2.5$, with a low value of sSFR $= 0.21$ Gyr^{-1}, and massive enough ($M_\star \sim 10^{11}$ M$_\odot$). In general, a galaxy with low sSFR has less gas to form stars. Low sSFR indicates that the amount of star-forming activity within the galaxy is little at given mass, so that the galaxy may be close to quench or have already quenched. Although the excitation condition should be taken into account, the detection of CO (4-3) may indicate existence of abundant cold gas in this galaxy. One of theories that can be considered as a quenching mechanism for this galaxy is morphological quenching (Martig et al. [2009]). This mechanism is based on the idea that the galaxy quenching is occurred by the gravitational stabilization of the disk owing to a stellar spheriod, instead of gas consumption, removal or termination of gas supply. It can explain the low sSFR for this galaxy with CO (4–3) detection. We note that the CO (3–2) line was not detected from the previous observations for HAE 7, perhaps due to the lack of sensitivity. The current upper limit of gas mass set by CO (3–2) is log $(M_{\rm gas}[M_\odot]) < 10.93$ $(3\,\sigma)$. We note that the galaxy was observed on the edge of the field of view in CO (3–2), which means that the upper limit does not give a strong constraint on the total gas mass. Another plausible explanation for the CO (4–3) detection is different gas excitation conditions for such low sSFR galaxies, compared to those of the main-sequence galaxies having similar stellar mass. We need to test the scenarios with deeper observations.

- **HAE 12** : the CO (4–3) line in HAE 12 is located at the edge of the frequency coverage, where the noise level of the spectrum increases. The peak position of CO (4–3) is offset from the that defined by Hα by $\sim 1''.0$. The S/N is one of the lowest values, thus we need deeper observations to confirm whether the detection is real or not, and its connection to the Hα emission.

- **HAE 23** : CO (4–3) line in HAE 23 is detected at 5 σ level with FWHM of $\sim$ 500 km s^{-1} in the Gaussian model fit. The offset from the Hα position is $\sim 0''.3$. In Sec 4.5, we discuss a potential merger scenario of this galaxy with HAE16.

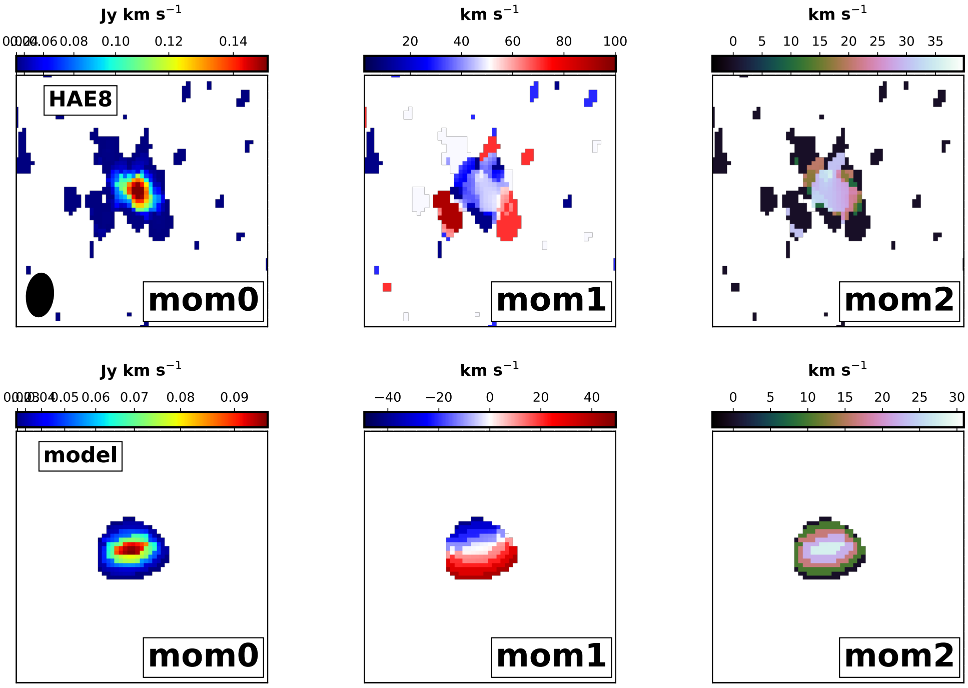

Figure 4.4: Top panels : moment maps for HAE 8 created from 20 km s^{-1} binned cube. From left to right : moment 0 (velocity-integrated intensity), moment 1 (velocity gradient) and moment 2 (velocity dispersion). We clipped the flux below $2.5\ \sigma$ for visibility. Note that the moment maps are integrated over the channel range that gives the highest S/N and the range is also used for GalPaK^{3D} modeling. Bottom panels : Model deconvolved maps for comparison. Clipped $2.5\ \sigma$.

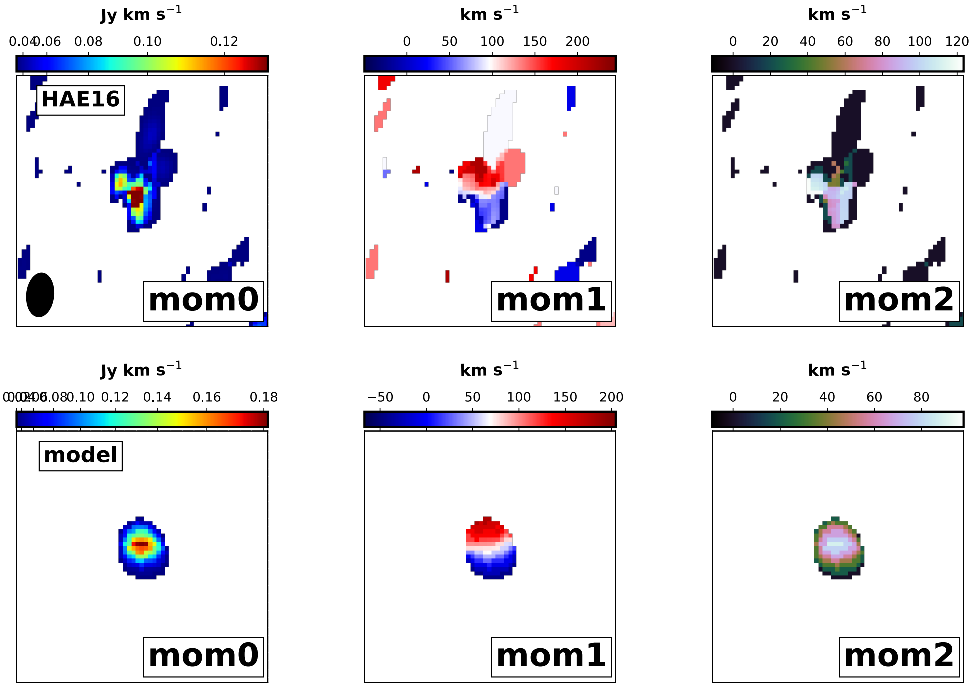

Figure 4.5: Moment maps for HAE 16 created from 40 km s^{-1} binned cube. See the description in Fig 4.4. For top panels, we clipped the flux below 2.8 σ for visibility. For bottom panels, the clipping threshold is set to 2.0 σ.

4.4 Disks in protoclsuter

4.4.1 V/σ evolution and disk settling

From the best-fit results of GalPaK^{3D} modeling, two galaxies show distinct kinematic properties. For a reference, typical star forming galaxies on the main sequence at $z \sim 2.3$ have a rotation velocity of $\sim$ 240 km s^{-1} and a velocity dispersion of $\sim$ 50 km s^{-1} (Übler et al. [2017]). The 64th percentile ranges are [160, 284] and [32, 68] for maximum rotational velocity and velocity dispersion, respectively in Übler et al. [2017]. The scatter of both values found in field galaxies does exist, mainly owing to the current observational limits on spatial resolution and to the limited number of galaxies that have been observed even in field studies. Considering such scatter, the estimated values of $V_{\rm rot}$ in two galaxies are consistent with that of the comparable population in fields, but σ_0 is lower in HAE 8 and higher in HAE 16, than the field value. While such differences in the velocity dispersion may be a signature of different evolutionary stages, we need higher angular resolution observations for further investigation to infer its physical meaning, if any.

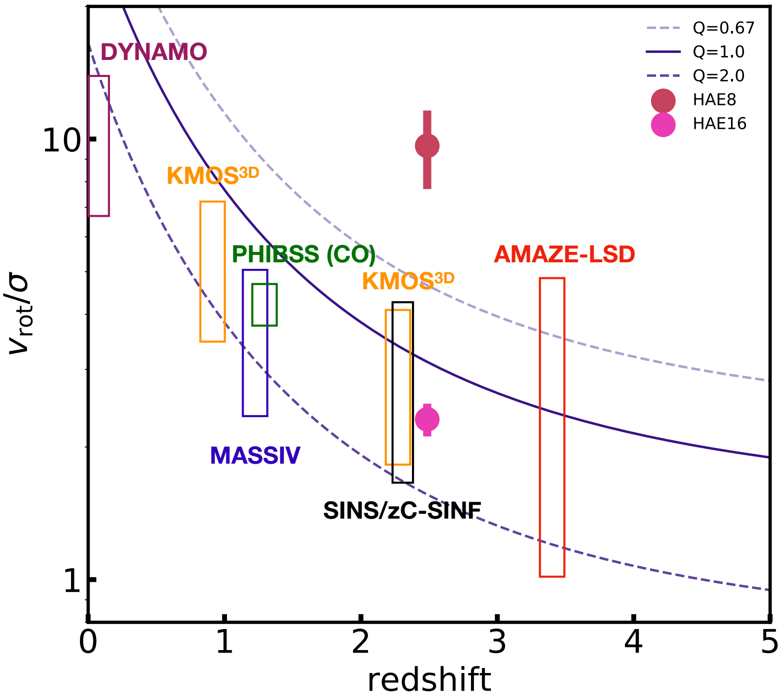

Figure 4.6: The evolution of V/σ for disk galaxies as a function of redshift. The estimates of V/σ for HAE 8 and HAE 16 are shown as filled circles. The data points are obtained from Wisnioski et al. [2015] and references therein. A solid line is the expected evolution of the V/σ by considering the marginally stable ($Q = 1$) disk and evolution of gas fraction. Other dashed lines are for $Q = 0.67$ (upper line) and $Q = 2.0$ (bottom line)

The ratio between rotational velocity ($V_{\rm rot}$) and intrinsic velocity dispersion (σ_0) provides information on the strength of galaxy rotation with respect to the random motion (or asymmetric drift). HAE 8 has a high value of $v_{\rm rot}/\sigma_0 \simeq 10$, suggesting that the galaxy is a rotation-dominated galaxy, though the observed velocity gradient in its moment 1 map is less clear than HAE 16. HAE 16 is more dispersion dominated with low $V_{\rm rot}/\sigma_0 \simeq 2$. The low value of HAE 16 still satisfies the criterion for a disk-like galaxy at high redshift (e.g., Tiley et al. [2016]). Considering the scatter of $V_{\rm rot}/\sigma_0$ found in the field observations and the small number of galaxies analyzed for the protocluster, which is only two, we conclude that the values of $V_{\rm rot}/\sigma_0$ for two of the protocluster members, which are disk-like galaxies, are broadly consistent with those of the field disk-like galaxies. Again, future observations are necessary to investigate whether there is a significant difference in the scatter of $V_{\rm rot}/\sigma_0$ between protocluster and field populations as an indicator of environmental effect.

Finally, we discuss the difference in the kinematic properties of two galaxies from the aspect of the measured gas fraction. As reviewed in the Introduction, the redshift evolution of the velocity dispersion is well-explained by the evolution of gas fraction and by assuming a marginally stable disk with the Toomre Q parameter of $Q = 1$ (Wisnioski et al. [2015]). The Toomre stability criterion (Toomre [1964]) is expressed as,

$$\frac{V_{\rm rot}}{\sigma_0(z)} = \frac{a}{f_{\rm gas}(z)\, Q_{\rm crit}} \tag{4.2}$$

where we take $Q_{\rm crit} = 1$ and $a = \sqrt{2}$ here. HAE 8 has a gas fraction of $f_{\rm gas} \sim 0.5$ (from our CO (3–2) observations), which is consistent with that of field galaxies. Considering the gas fraction, HAE 8 is kinematically more evolved, i.e., more rotation-dominated given its gas fraction. On the other hand, HAE 16 has a higher gas fraction ($f_{\rm gas} \sim 0.8$) and such a higher gas fraction of HAE 16 could make its disk component less stable, which is roughly consistent with the lower value of $V_{\rm rot}/\sigma$.

Before closing this section, we remark two issues related to the estimated parameters.

Parameter degeneracy, or physical origin?

Although the GalPaK$^{\rm 3D}$ code appears to successfully constrain the 10 free parameters from the 3D modeling with MCMC, some degeneracies between parameters remain. In particular, when the galaxy structure is not well resolved, inclination, velocity dispersion and maximum velocity can be all degenerated, which then affects our interpretation of $V_{\rm rot}/\sigma_0$ (see figures in Appendix B). The MCMC correlations for HAE 8 seems to show such degeneracies, i.e., a positive correlation between inclination and velocity dispersion for HAE 8 (see Figure B1 in Appendix B). Further, the systemic uncertainty for the modeling itself has not been taken into account for the error estimation. Low S/N per channel may be also problematic in constraining the parameters, even though two galaxies are detected as the highest S/N among the CO (4–3) detection (peak S/N = 8-10) and the best-fits of GalPaK$^{\rm 3D}$ seem to trace the velocity structure of individual galaxies in the data cube (see Figure B3 and B4). In this regard, we need deeper observations to investigate more on these galaxies.

We find that HAE 8 (observed at a face-on view) has a lower value of σ_0 than HAE 16 (observed at a edge-on view). Related to this, there is a report related to the anisotropy of velocity dispersion with respect to the inclination of the galaxy, using SINS data (therefore, some are observed in the AO mode, Genzel et al. [2011]). From this survey, the face-on galaxies had a higher $V_{\rm rot}/\sigma_0$ value by a factor of $\sim$ 1.4, than edge-on galaxies. They discussed if the trend can be physically originated from a clump-clump interaction in the disk, in a sense that the clump-clump interaction would enhance the turbulence in galactic plane larger than the perpendicular to it, but it was not convincing with the given data. Higher angular-resolution imaging observations is needed for a larger number of galaxies. Similarly, our current ALMA observations in CO (4–3) still lack in the resolving power. The resolution of $0''.5 \times 0''.3$, corresponding to $\sim$ 3.5 kpc, is still not sufficient to resolve the inner structure of the galaxy, given the typical size of $r_e = 4 - 5$ kpc for a star forming galaxy at high-z.

Mergers seen as disks?

There is a chance of misidentification of mergers as disk-like galaxies. For example, Hung et al. [2016] simulated local merging galaxies and showed that the known mergers found in the local universe could have the appearance of disk-like galaxies at high redshift without a sufficient resolution and sensitivity. With these results, they concluded that the merger rate at high redshift could be underestimated. Other simulation showed that the lower value of V/σ observed at high redshift can be contaminated by mergers (Susan Kassin in private communication, R. Simons et al. in prep.); at a specific point of encountering and from the specific viewing angle, mergers are observed as “disks” with a smooth velocity gradient; a simple criterion of $V_{\rm rot}/\sigma > 2$

as a disk galaxy would include such contamination. Of course, the encountering time for mergers is extremely short and the probability of such case would be small. However, such concerns can become a severe issue for a particular case, i.e., in overdense regions of protoclusters, where the merger rate is expected to be high.

Bearing in mind that we cannot exclude a possibility that potential mergers are seen as disks, we compare HAE 8 and HAE 16 with field disk-like galaxies at high and low redshifts in the following sections.

4.4.2 Tully-Fisher relation

We investigate the Tully-Fisher relation (TFR) to relate a galaxy with its embedded dark matter halo. The correlation between the luminosity and the rotation velocity for galaxies is well known for several decades (Tully & Fisher [1977]), placing it as one of the fundamental scaling relations for disk galaxies. The parameters for the TFR, i.e., the zero-point (b), slope (a) and scatter of the TFR have been used to constrain galaxy formation models (e.g., Cole & Kaiser [1989]; Mo & Mao [2004]). The existence of TFR implies that the growth of the luminous matter (traced by L) is closely connected with that of the dark matter (traced by $V_{\rm rot}$ or circular velocity $V_{\rm circ}$), which is scaled as $L \propto v^4/\Sigma(M/L)$. The TFR is usually expressed in mass-based forms, as $M \propto v^4$, or in log scale, $\log M = a \cdot \log v + b$. Here, we adopt the mass-based form in log scale to express the TFR.

We test the TFR for HAE 8 and HAE 16, given that they are rotation-dominated systems of $V_\sigma/\sigma > \sqrt{(}4.4)$ (Tiley et al. [2016]). As a probe of dark matter at given luminous mass budget, we need to estimate a circular velocity (v_c) of a galaxy. Provided that high-z galaxies are turbulent, i.e., large σ_0, (Förster Schreiber et al. [2006]; Swinbank et al. [2012]; Wisnioski et al. [2015]), we define a circular velocity by taking into account the effect of the turbulence on the rotational velocity. The circular velocity is expressed as follows, which is derived from the hydrostatic equation and by assuming a pressure-support term to be independent of the radius (r) and the scale-height (z) (e.g., Burkert et al. [2010]) :

$$v_{\rm cir}^2 = v_{\rm rot}^2 + 2\sigma^2 \frac{r}{r_d} \qquad (4.3)$$

where $r_{\rm d}$ is the disk scale length (Burkert et al. [2010]) and $r_{\rm d} = r_{\rm e}/1.68$ for a case of an exponential disk (Freeman [1970]). We assume the radius (r) where the turbulent motions reach the

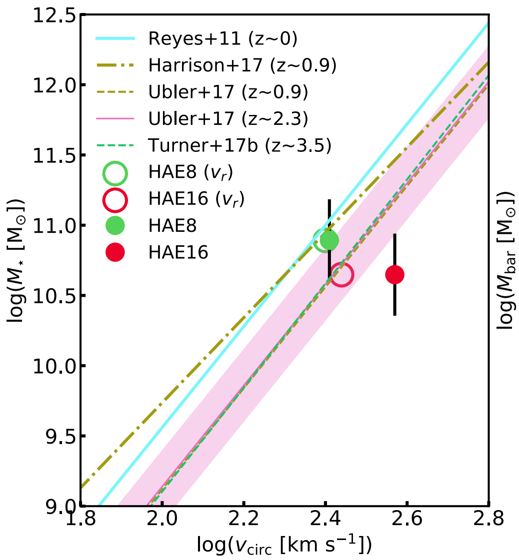

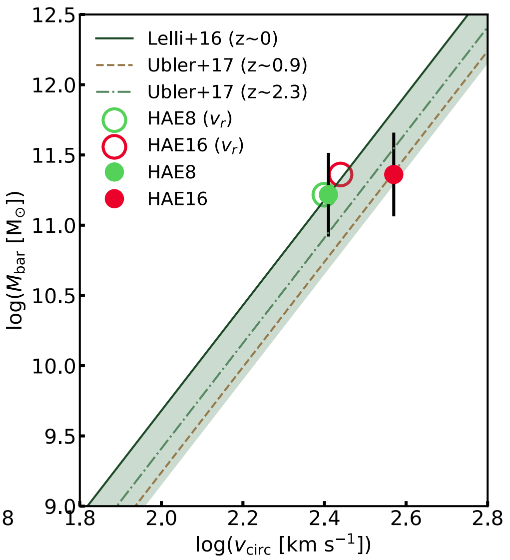

Figure 4.7: The TFR relation for HAE 8 and HAE 16. The filled circles indicate the estimate for a circular velocity by taking into account the pressure support (Eq. 4.3). Open circles show the measurements based on the case of $v_{\rm circ} = v_{\rm rot,max}$. We plot the best fit result from Übler et al. [2017] for local and high-z sTFR (left) and bTFR (right). The color band on each panel is to show the scatter (ξ) of the TFR at $z \sim 2.3, \xi = \pm 0.22$ for sTFR and $\xi = \pm 0.26$ for bTFR from Übler et al. [2017]. The local relations at $z \sim 0$ are calculated from Reyes et al. [2011] for sTRF and Lelli et al. [2016] for bTFR, by assuming the dynamical support from turbulent motion is negligible, i.e., $v_{\rm rot} \equiv v_{\rm circ}$. Other measurements are also plotted for sTFR from Harrison et al. [2017] at $z \sim 0.9$, Turner et al. [2017a] at $z \sim 3.5$. We note that for Harrison et al. [2017], the line fitting did not take into account the pressure support for the velocity component, hence $v_{\rm circ} = v_{\rm rot}$.

maximum value, which is approximately $r = 2.2r_d$. Hereafter, we use this definition otherwise it is specifically mentioned.

We investigate the TFR based on stellar mass (sTFR) and baryon mass (bTFR). Considering the error, the sTFR and bTFR for HAE 8 and HAE 16 are consistent with field comparable galaxies obtained at $z \sim 2.3$ (Übler et al. [2017]) as shown in Figure 4.7. HAE 8 lies on the upper limit of both sTFR and bTFR, i.e., smaller circular velocity at given mass. HAE 16 is the opposite case, which is located on the lower limit of the sTFR and bTFR, i.e., higher circular velocity at given mass.

While the evolution of TFR is still controversial with different definitions of circular velocity[¶],

---

[¶] Currently, the evolution of TFR has been investigated up to $z \sim 4$ (e.g., Puech et al. [2008]; Cresci et al. [2009]; Reyes et al. [2011]; Kassin et al. [2012]; Lelli et al. [2016]; Tiley et al. [2016]; Price et al. [2016]; Straatman et al. [2017]; Harrison et al. [2017]; Übler et al. [2017]; Turner et al. [2017a]). Unfortunately, many studies report a varying degree of evolution or no evolution on the normalization (zero-point offset) of the TFR. Related to this, there are ranges of the definition of circular velocity (e.g., Kassin et al. [2012]; Übler et al. [2017]; Turner et al. [2017a]).

at least one argument is in agreement that higher redshift disk-like galaxies are less likely to be rotation-dominated. At the highest redshift bin at $z \sim 3.5$, only 34% of galaxies are rotation supported ($V/\sigma > 1$) (Turner et al. [2017b]). At this redshift, both massive ($> 10^{10}\ M_\odot$) and less massive ($\sim 5 \times 10^9\ M_\odot$) galaxies are still in the early stage of the disk formation and have not been "settled" with lower rotation velocity (Gnerucci et al. [2011]; Turner et al. [2017a]). With the cosmic time, disks of massive galaxies are settled earlier, followed by less massive galaxies (i.e., kinematical downsizing, e.g., Kassin et al. [2012]; Simons et al. [2016]).

As discussed in Sec 4.4.1, there is a hint of different evolutionary stages inferred from the different the velocity dispersion between HAE 8 and HAE 16 that have almost similar rotational velocities. HAE 8 is more massive in stellar mass by a factor of ~ 2, more rotation-dominated ($V_{\rm rot}/\sigma_0 \simeq 10$) and less gas-rich ($f_{\rm gas} \simeq 0.5$) than HAE 16, though HAE 8 is still fairly gas-rich compared to local galaxies. In this regard, the evolutionary stage of HAE 8 may be the later one than that of HAE 16, if we consider the kinematical downsizing.

Given only two galaxies with a subtle difference of stellar mass and the uncertainties included in estimating the stellar mass, it is difficult to conclude that two galaxies are in kinematically different evolutionary stages, and to infer a model of galaxy evolution for disk-like galaxies associated to the protocluster. To infer such, we need to observe more galaxies to investigate a time scale of the disk settlement in protoclusters.

4.4.3 Specific angular momentum

We measure a specific angular momentum of two galaxies to explore potential local progenitors. We use a simple estimator of the specific angular momentum following Romanowsky & Fall [2012], by assuming an exponential disk model. The idea for the estimator is based on the assumption of axisymmetric density distribution for a galaxy, allowing us one-dimensional analysis (see for Appendix A in Romanowsky & Fall [2012] for more discussion and Obreschkow & Glazebrook [2014] for the potential limitations of the estimator). For an exponential disk, the specific angular momentum (j) is expressed as follows[1].

$$j = 2\, v_{\rm circ}\, r_d = 1.19\, v_{\rm circ}\, r_e \tag{4.4}$$

---

[1] We note that the specific angular momentum j defined in Romanowsky & Fall [2012] is specifically that of stellar component. Nevertheless, it assumes that gas and stellar kinematics are comparable with each other. Following this, we assume that the specific angular momentum calculated from cold gas component is similar to that of stars (for a disk-dominant galaxy).

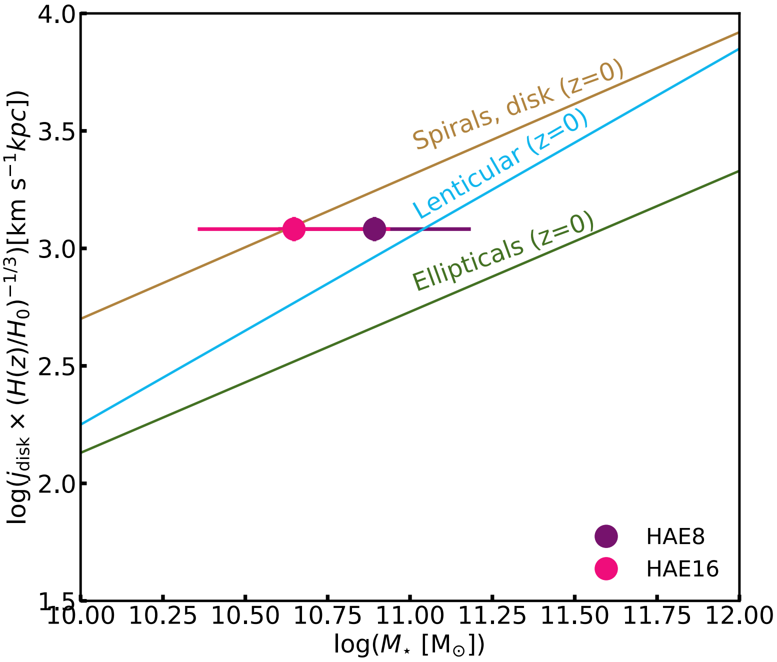

Figure 4.8: The specific angular momentum of HAE 8 and HAE 16.

Figure 4.8 shows that our estimates of specific angular momentum are broadly consistent with a value of disk galaxies found in the local universe. Two galaxies in the protocluster still have a significant amount of angular momentum, if the galaxies evolve into elliptical galaxies in massive clusters. It is worth to note that the positions of HAE 8 and HAE 16 are both near the 2D density peak of the protocluster and the proper velocity is close to zero, i.e., close to the nominal center of the protocluster, suggesting the likelihood for becoming elliptical galaxies would be high. Comparing two galaxies, HAE 8 which is more massive than HAE 16, have lost some amount of its angular momentum while building-up its mass, if they are born in the same halo (with same initial angular momentum). Or, HAE 8 might have formed in a halo with smaller angular momentum than HAE 16.

4.4.4 Disks in the densest region

Another interesting thing related to these two disk-like galaxies is that both are detected in the densest region of the protocluster. As Figure 2.2 and Figure 4.3 show, HAE 8 and HAE 16 are located in the densest region, i.e., in the CW, of the protocluster.

In the hierarchical structure formation described by the ΛCDM model, galaxies in denser regions have higher probability to experience major merger events, and some observational results present presumably higher rate of mergers at high redshift protoclusters (e.g., Hine et al. [2016]; Hayashi et al. [2017] and see also the following section 4.5).

The detection of disk-like galaxies in the densest region gives an insight on galaxy evolution within the protocluster, together with the measurements of the gas content. In a recent observational study of local merger remnants, Ueda et al. [2014] reported that the merger remnants detected in CO lines showed clear disk-like velocity gradients. The result suggested that a merger of gas-rich disk galaxies (detected in CO lines) can effectively form a disk-like structure, if they are gas-rich enough. The hydrodynamical simulations of gas-rich mergers is consistent with the result, indicating a survival of disk components after a merger event (Hopkins et al. [2009]). Recent simulations also report an increase of $j_\star$ by 10 per cent from wet merger, while a decrease by 30 per cent decrease from dry merger, on average (Lagos et al. [2018]). This suggests that gas-rich mergers cannot allow galaxies to lose the angular momentum effectively at high-redshift, and such occasion may happen more frequently in dense regions at high redshift. As a result, we may find disk-like galaxies easily in the densest regions of the protoclusters once they are gas-rich, even though they have experienced mergers.

In the Illustris simulation, early-type galaxies at $z = 0$ have been once located along the line of (high-z) spiral galaxy relation (in the $j_\star - M$ plane) at high redshift (Genel et al. [2015]). Genel et al. [2015] argued the necessity of feedback that lowers the specific angular momentum. In this point of view, two disk-like galaxies found in the protocluster may need to experience some form of feedbacks, not the gas-rich mergers, to become early-type galaxies located in the present-day clusters.

Good tests for tracing the evolutionary track of galaxies include observations of larger number of galaxies and of higher angular resolution imaging (with better sensitivity). As a case study of the latter exploration, it may be worth to probe whether HAE 8 (with high $V_{\rm rot}/\sigma_0$) has a denser bulge-like component in the central, which is hard to confirm with our data in hand (in low S/N and lower resolution), and to find a signature of gas inflow or outflow for probing the loss of angular momentum and of recent mergers by searching for diffuse structure, e.g., tidal tails, in its outer disk.

4.5 Potential mergers

In addition to 'disk-like' galaxies in the densest regions of the protocluster, we find three potential mergers. They have broad velocity components in the Gaussian-model fit (FWHM$\gtrsim$ 1000 km s^{-1}) where the broad nature might not be simply explained by the typical galactic rotation, and one of them is likely to have an interacting galaxy nearby. In the following, we present the details of three galaxies.

- HAE 9 : HAE 9 has sub-components when it is observed with the finer beam, improved by a factor of two, in the CO (4–3) observations (Fig 3.4). The CO (3–2) spectrum of the galaxy shows a double peak. In velocity, the peak of the main component in CO (4–3) is blue-shifted by $\sim$ 300 km s^{-1} than the reference velocity (or the redshift) determined by CO (3–2), which is roughly consistent with the velocity of the blue-ward peak of CO (3–2). After re-checking the velocity integration range and the image, we find an additional red-ward component, which still satisfies our detection criteria but with low S/N. The peak velocity of the redshifted component in CO (4–3) is corresponding to the red-ward peak of CO (3–2). We note that our detection methods are optimized to find a component integrated over a specific velocity range that gives the highest S/N. We show the identified blue (HAE 9a) and red (HAE 9b) sub-components in Figure 4.9. We measure a morphological position angle (mPA) from 1.1 mm where the emission is extended and marginally resolved. By applying `uvmodelfit`, the morphological PA (mPA= -60 ± 19 degree) of HAE 9 is different from the kinematical position angle (kPA) seen in CO (4–3) by more than 30 degree, if we assume that both blue and red components in CO (4–3) are originated from the same galaxy. For a reference, the KMOS^{3D} disk galaxies have consistent kPA and mPA within 30 degree in the 80% of the sample, though the fraction decreases with larger redshift (Wisnioski et al. [2015]). It is not conclusive whether HAE 9 is a merger or not, but a few other observational facts are raised as an indication of a merger. First, the peak is resolved into (at least) two components in the intensity map, when the integrating velocity range is taken over the blue and the red component channels. Second, the line width is too broad to consider it as a disk galaxy, FWHM $\sim$ 1000 km s^{-1}.

- HAE 3 : the velocity offset between CO (4–3) and CO (3–2) lines is subtle, within the uncertainty of the underlying velocity resolution. However, the CO (4–3) spectrum is broader than CO (3–2) by a factor of two. Both are detected in low S/N which we need confirmation of the FWHM. We plot the red-ward and blue-ward components of the CO (4–3) line, which are shown in red and blue contours, respectively, on the right top two panels in Figure 4.10. This case, only the red component is satisfying our detection

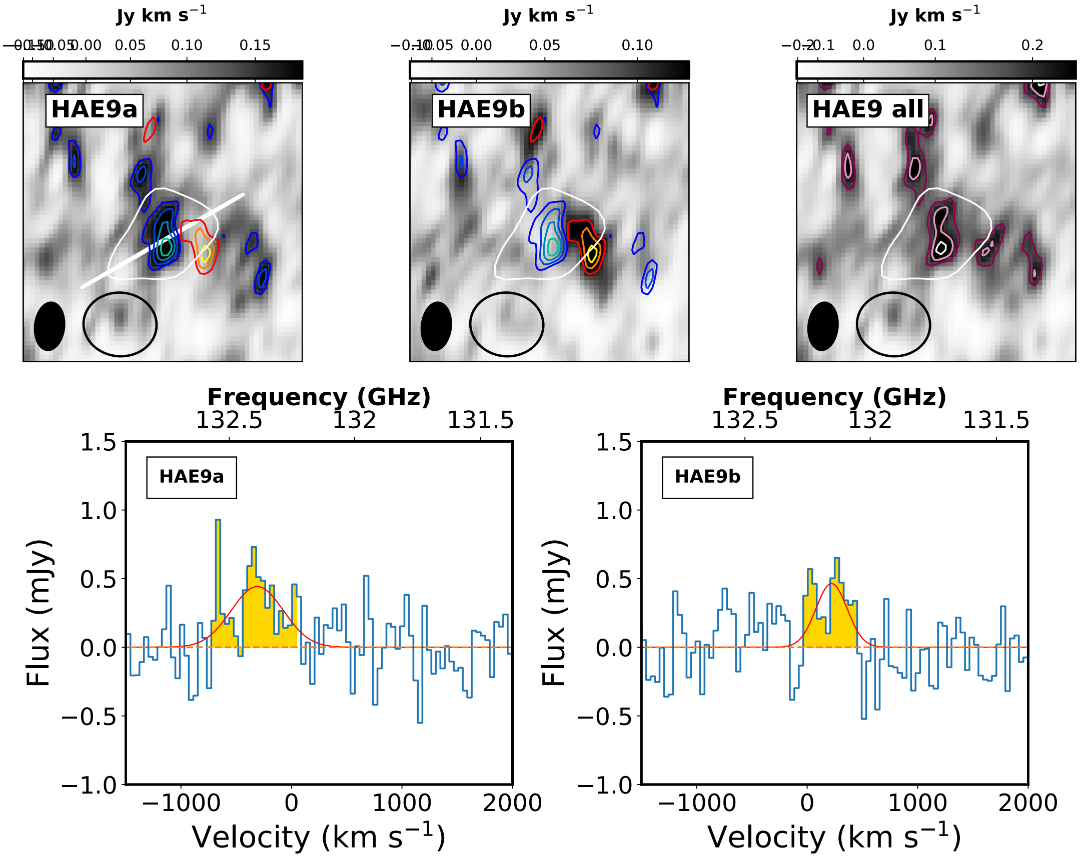

Figure 4.9: Top panels : velocity-integrated intensity map for HAE 9 sub-components. HAE 9a is the main component that has the highest S/N and HAE 9b is the additional component that still satisfies our detection criteria found near the main component. Blue contours are for HAE 9a and red contours are for HAE 9b. The top right panel is the moment 0 map that is obtained from integrating the whole channel range used to identify HAE 9a and HAE 9b. All contours are starting from 4σ in steps of 1σ, i.e., 4σ, 5σ, 6σ, ...White contour is the 4σ contour for 1.1 mm detection. The white solid line is the morphological position angle derived from 1.1 mm continuum, which is inconsistent with kinematical position angle, i.e., the line that connects the peak of the red and blue components. The peak position offset between HAE 9a and HAE 9b is larger than the minor axis of the beam, suggesting this is resolved. We show the beam size of CO (4−3) in filled black circle and that of 1.1 mm in an open ellipse. Bottom panels : the spectrum derived at the peak position and within a area of the beam (0.5×0.3) for HAE 9a and HAE 9b. The velocity resolution is set to 40 km s^{-1} since this resolution gives the higher peak S/N for each component.

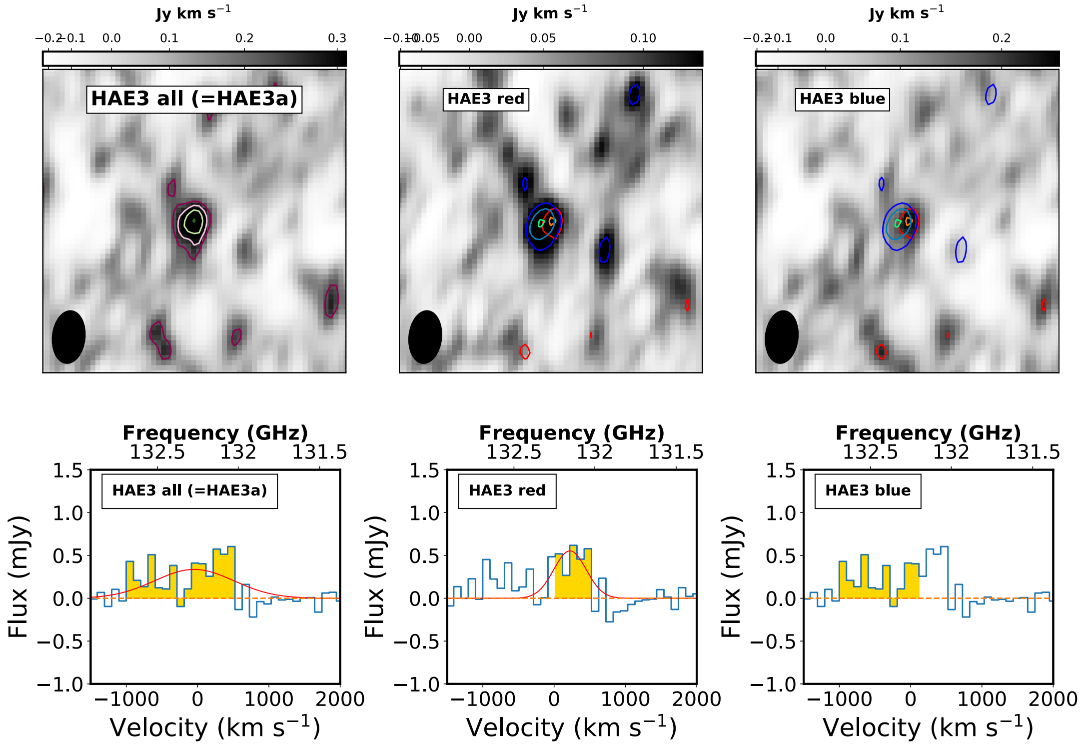

Figure 4.10: Top panels : velocity-integrated intensity map for HAE 3. The top left panel is the moment 0 map (HAE 3a), which is integrated over the range that delivers the highest S/N. On the top middle and right panel, we show blue and red components of HAE 3 all (=HAE 3a). We divide into two sub-components where the ranges are determined based on S/N (i.e., set to have high S/Ns in both components). Blue contours are for the blueward component and red contours are for redward component, where only HAE 3 blue component satisfies our detection criteria. All contours are starting from 4σ in steps of 1σ, i.e., 4σ, 5σ, 6σ, ... We show a beam size of CO (4–3) observations in a filled black circle. Bottom panels : the spectrum derived at the peak position and within an area of the beam (0.5×0.3) for HAE 3a, blue and red components. The velocity resolution is set to 100 km s^{-1} since this resolution gives the higher peak S/N for each component.

criteria. We have a AO-supported image of HAE 3 in Kp band (Fig 3.2), which show an elongated stellar structure in the north-south direction in the smoothed image. While it is tempting as a suggestive of a potential merger, the S/N for the AO image does not suffice to trust the GALFIT result. Hence, we need deeper and higher angular resolution observations in NIR.

- HAE23 : the galaxy is detected, although marginal, very close to HAE 16. The redshift difference between two galaxies are $\sim$ 1000 km s^{-1} in velocity and the projected distance is less than a few of tens kpc (∼25 kpc). While it is hard to conclude that HAE23 is a counterpart of merging galaxy with HAE 16, or an interacting galaxy, we note for HAE 16 that the galaxy manifests fairly high velocity dispersion in the best-fit model. The high gas fraction of HAE 16 can derive the high velocity dispersion, but the interaction with HAE23, if any, could also boost the effect.

If all of these are mergers, two of them are also located in the densest regions of the protocluster, where we also find disk-like galaxies as discussed in the previous section. Also, by simple calculation, $\sim$ 10% of the HAEs (3/25) are undergoing mergers within the protoclusters giving a crude lower limit of the merger fraction within the protocluster. The merger fraction itself is consistent or slightly lower compared to the value obtained by field studies at high redshift (e.g., Conselice [2014]), though the value is calculated without any considerations of completeness and false detection and the methods to define the merger fraction are different in literatures so that it is difficult to compare directly. For the confirmation of mergers, deeper and higher angular resolution observations in CO (or emission lines) are necessary.

4.6 Conclusion

We investigated gas kinematics from higher angular resolution in CO (4–3). Our findings are as follows.

1. We detected CO (4–3) lines from 10 HAEs. Among them, 5 HAEs are previously detected in CO (3–2) and the redshifts distinctively determined by the CO lines are roughly consistent with each other.

2. We presented the crude estimate for the halo mass of the protocluster, by combining the redshift information from Hα spectroscopy and CO detection. Assuming the substructures are virialized, we found that the protocluster would become a Virgo-like cluster

($> 10^{14} M_\odot$) at $z = 0$ at least, if the protocluster follows the typical halo growth as expected from simulations.

3. We modeled two galaxies, HAE 8 and HAE 16, which are detected clearly with S/N larger than 8. The appearance of two galaxies is disk-like with smooth velocity gradients. We used GalPAK^{3D} for modeling the data cubes. The results show that two galaxies are consistent with the properties of field disk-like galaxies, though there is a hint of the high value of the velocity dispersion for one of the galaxies, which need future observations.
4. We examined the Tully-Fisher relation and investigated the specific angular momentum for HAE 8 and HAE 16. The Tully-Fisher relation for these two is broadly consistent with that of field population within the observational errors, and the specific angular momentum is consistent with local spirals and high-z field disk-like population. If these two galaxies are the progenitors of low-z elliptical galaxies (or slow rotators), dynamical frictions by feedbacks or (dry) mergers are necessary to lose the angular momentum.
5. We searched for potential mergers within the protocluster that were detected in CO (4–3). We found signatures of mergers or interaction from the three HAEs besides the large line widths of them seen in CO (4–3); (1) the kinematical position angle is different from the morphological position angle by more than 30 degree (HAE 9), (2) one galaxy shows an elongated structure in the AO image with large CO (4-3) line widths (HAE 3) and (3) a potential interacting galaxy is found in the 3D map.

We find a diversity of kinematic properties for star forming galaxies within the protocluster, and the overall properties of cold gas are broadly consistent with field disk-like population. Future observations with improved sensitivity and higher resolution are inevitable to confirm a signature of any difference. Along with these, we also need to investigate what physical mechanisms derive such diversity and to track the evolutionary phases of them, to fully understand the evolution of galaxies within protoclusters.

Experience has shown, and a true philosophy will always show, that a vast, perhaps the larger portion of the truth arises from the seemingly irrelevant.

Edgar Allan Poe

Chapter 5

Conclusion

We set a goal to answer following key questions to reveal galaxy evolution in overdense regions at high redshift.

1. What is the gas fraction of the star forming galaxies in the protoclusters?
2. In relation to the gas content, is there a difference between the comparable field galaxies at the same redshift? If so, why would that be? If not, why would not?
3. Are star forming galaxies associated to protoclsuters mostly mergers or disks?
4. For disk galaxies, is there any kinematic difference between protocluster members and comparable field galaxies at the same redshift?

These questions are also raised to understand whether the environments at moderate density at high redshift can affect the early galaxy evolution occurred in denser regions and to understand the formation of cluster population in the local universe. The studies presented in the Dissertation, are one of the first systematic surveys that have been conducted toward the typical star forming galaxies associated to the (high-redshift) protoclusters.

5.1 Cold gas content of the star forming galaxies at high-z protocluster

In answering the top two questions, we investigated the cold gas content of the star forming galaxies that are associated to protocluster 4C23.56 at z=2.5. We targeted typical star forming galaxies traced by Hα emission that falls into a specific redshift range ($2.469 < z < 2.503$) using the narrow band filter. As a probe of the global gas content, we observed CO (3–2) line and 1.1 mm dust continuum with ALMA which are observed in a spatial resolution of $\sim 0''.7 - 0''.9$. We detected seven HAEs in CO (3–2) and four HAEs in the dust continuum among 22 and 19 HAEs covered within the ALMA FoVs, respectively. The detection is occurred in a massive stellar regime ($> 4 \times 10^{10}\, M_\odot$). Gas mass from CO (3–2) was derived using the "Galactic" conversion factor with additional correction for the metallicity dependence, which yields broadly consistent value derived from dust-based calibration. The gas fraction of the massive star-forming galaxies, with $f_{\rm gas} = 0.53 \pm 0.07$ from CO (3–2), is consistent with that of comparable field galaxies. We found a correlation between the gas fraction and stellar mass, and between the gas fraction and the local density, though the latter case is very marginal. Gas depletion time in a galactic scale ($\sim$10 kpc) is *on average* consistent with that obtained in field galaxies, but there is a signature of a positive correlation between the global star forming efficiency (i.e., the inverse of gas depletion time) and the stellar mass in the mass range of $\log M_\star = [10.64, 11.30]$, which has not been found in general field studies. Future observational studies are necessary for the confirmation of the correlations by observing a larger number of galaxies in a wider mass range and in different environments.

5.2 Gas kinematics

To address the third and the fourth questions, we investigated gas kinematics using higher resolution ($0''.3 \times 0''.5$) imaging of CO (4–3) line with ALMA. We detected CO (4–3) lines from 10 HAEs; five among them were detected in our previous CO (3–2) observations and the remaining five are the first detection in CO line. Two galaxies indicate smooth velocity gradients in their CO (4–3) images, a suggestive of disk-like components, and are detected in relatively high S/N ($\gtrsim 8$), which allows us to investigate more on these galaxies with kinematic modeling. The best-fit models from GalPaK$^{\rm 3D}$ suggest that the estimated values of $V_{\rm rot}$ and σ_0 are broadly consistent with those obtained in field galaxies, though there is a hint of a smaller value of σ_0 for one galaxy (HAE8), so the higher value in the ratio of $V_{\rm rot}/\sigma_0$, which need to be re-examined by higher angular resolution observations. We also found that these two galaxies are consistent with local spiral galaxies in terms of the specific angular momentum; they need to lose the angular momentum to evolve into elliptical galaxies. Also, they are located within the expected range of Tully-Fisher relation at high redshift ($z \sim 2$). In addition to disk-like population, we also find three candidates of mergers or interacting galaxies by investigating CO line widths and images in CO velocity channels together with a help of multi-band Opt/IR data sets, e.g., high spatial resolution Ks-band images. Finding both disk-like galaxies and mergers in the densest region of the protoclsuter may imply distinct dynamical processes for such a dense environment at high redshift for fast and more sensitive observations are necessary to constrain the physical mechanism.

In an attempt to finding any difference between protocluster and field populations, we find no significant difference on the cold gas content of galaxies and the kinematic properties, on average, at the massive-end above $10^{10}M_{\odot}$. By our limited sample size, it is difficult to provide a concrete paradigm for the galaxy evolution in the protocluster.

Our future prospects for the protocluster studies are to enlarge the sample size with observations of higher angular resolution and of higher depth. In addition to gas content and kinematics, probing gas excitation conditions at high angular resolution could be another window to constrain galaxy evolution in protoclusters.

References

Allen, S. W., Evrard, A. E., & Mantz, A. B. 2011, ARA&A, 49, 409

Appleton, P. N., Guillard, P., Boulanger, F., et al. 2013, ApJ, 777, 66

Bahcall, N. A., & Cen, R. 1993, ApJL, 407, L49

Beers, T. C., Flynn, K., & Gebhardt, K. 1990, AJ, 100, 32

Bekki, K. 1998, ApJL, 502, L133

Bell, E. F., Papovich, C., Wolf, C., et al. 2005, ApJ, 625, 23

Berta, S., Lutz, D., Genzel, R., Förster-Schreiber, N. M., & Tacconi, L. J. 2016, A&A, 587, A73

Best, P. N., Lehnert, M. D., Miley, G. K., & Röttgering, H. J. A. 2003, MNRAS, 343, 1

Binney, J., & Tremaine, S. 2008, Galactic Dynamics: Second Edition (Princeton University Press)

Blumenthal, G. R., Faber, S. M., Primack, J. R., & Rees, M. J. 1984, Nature, 311, 517

Blundell, K. M., & Fabian, A. C. 2011, MNRAS, 412, 705

Bolatto, A. D., Wolfire, M., & Leroy, A. K. 2013, ARA&A, 51, 207

Bolatto, A. D., Warren, S. R., Leroy, A. K., et al. 2015, ApJ, 809, 175

Bouché, N., Carfantan, H., Schroetter, I., Michel-Dansac, L., & Contini, T. 2015, AJ, 150, 92

REFERENCES

Bower, R. G., Benson, A. J., & Crain, R. A. 2012, MNRAS, 422, 2816

Brough, S., van de Sande, J., Owers, M. S., et al. 2017, ApJ, 844, 59

Bruzual, G., & Charlot, S. 2003, MNRAS, 344, 1000

Buitrago, F., Trujillo, I., Conselice, C. J., et al. 2008, ApJL, 687, L61

Bullock, J. S., Kolatt, T. S., Sigad, Y., et al. 2001, MNRAS, 321, 559

Bundy, K., Ellis, R. S., & Conselice, C. J. 2005, ApJ, 625, 621

Bundy, K., Ellis, R. S., Conselice, C. J., et al. 2006, ApJ, 651, 120

Burkert, A., Genzel, R., Bouché, N., et al. 2010, ApJ, 725, 2324

Cai, Z., Fan, X., Peirani, S., et al. 2016, ApJ, 833, 135

Cappellari, M. 2013, ApJL, 778, L2

—. 2016, ARA&A, 54, 597

Cappellari, M., Emsellem, E., Bacon, R., et al. 2007, MNRAS, 379, 418

Carilli, C. L., & Walter, F. 2013, ARA&A, 51, 105

Chiang, Y.-K., Overzier, R., & Gebhardt, K. 2013, ApJ, 779, 127

—. 2014, ApJL, 782, L3

Chiang, Y.-K., Overzier, R. A., Gebhardt, K., & Henriques, B. 2017, ApJL, 844, L23

Chiang, Y.-K., Overzier, R. A., Gebhardt, K., et al. 2015, ApJ, 808, 37

Cicone, C., Maiolino, R., Sturm, E., et al. 2014, A&A, 562, A21

Clements, D. L., Braglia, F. G., Hyde, A. K., et al. 2014, MNRAS, 439, 1193

Cole, S., & Kaiser, N. 1989, MNRAS, 237, 1127

Condon, J. J. 1992, ARA&A, 30, 575

Conselice, C. J. 2014, ARA&A, 52, 291

Cooke, E. A., Hatch, N. A., Muldrew, S. I., Rigby, E. E., & Kurk, J. D. 2014, MNRAS, 440, 3262

Cooke, E. A., Hatch, N. A., Stern, D., et al. 2016, ApJ, 816, 83

Cowie, L. L., Songaila, A., Hu, E. M., & Cohen, J. G. 1996, AJ, 112, 839

Cresci, G., Hicks, E. K. S., Genzel, R., et al. 2009, ApJ, 697, 115

da Cunha, E., Walter, F., Smail, I. R., et al. 2015, ApJ, 806, 110

Daddi, E., Dannerbauer, H., Elbaz, D., et al. 2008, ApJL, 673, L21

Daddi, E., Dickinson, M., Morrison, G., et al. 2007, ApJ, 670, 156

Daddi, E., Bournaud, F., Walter, F., et al. 2010, ApJ, 713, 686

Daddi, E., Dannerbauer, H., Liu, D., et al. 2015, A&A, 577, A46

Danese, L., de Zotti, G., & di Tullio, G. 1980, A&A, 82, 322

Darvish, B., Mobasher, B., Sobral, D., et al. 2016, ApJ, 825, 113

Davé, R., Finlator, K., & Oppenheimer, B. D. 2011, MNRAS, 416, 1354

Davis, M., & Geller, M. J. 1976, ApJ, 208, 13

De Breuck, C., Bertoldi, F., Carilli, C., et al. 2004, A&A, 424, 1

de Vaucouleurs, G. 1948, Annales d'Astrophysique, 11, 247

Decarli, R., Walter, F., Aravena, M., et al. 2016a, ApJ, 833, 69

—. 2016b, ApJ, 833, 70

D'Eugenio, F., Houghton, R. C. W., Davies, R. L., & Dalla Bontà, E. 2013, MNRAS, 429, 1258

Dickman, R. L., Snell, R. L., & Schloerb, F. P. 1986, ApJ, 309, 326

Djorgovski, S. G., Stern, D., Mahabal, A. A., & Brunner, R. 2003, ApJ, 596, 67

Domínguez, A., Siana, B., Henry, A. L., et al. 2013, ApJ, 763, 145

Dressler, A. 1980, ApJ, 236, 351

REFERENCES

Elbaz, D., Daddi, E., Le Borgne, D., et al. 2007, A&A, 468, 33

Elbaz, D., Dickinson, M., Hwang, H. S., et al. 2011, A&A, 533, A119

Emonts, B. H. C., Feain, I., Röttgering, H. J. A., et al. 2013, MNRAS, 430, 3465

Emonts, B. H. C., Lehnert, M. D., Villar-Martín, M., et al. 2016, Science, 354, 1128

Emsellem, E., Cappellari, M., Krajnović, D., et al. 2007, MNRAS, 379, 401

—. 2011, MNRAS, 414, 888

Epinat, B., Tasca, L., Amram, P., et al. 2012, A&A, 539, A92

Finn, R. A., Zaritsky, D., McCarthy, Jr., D. W., et al. 2005, ApJ, 630, 206

Flores, H., Hammer, F., Puech, M., Amram, P., & Balkowski, C. 2006, A&A, 455, 107

Förster Schreiber, N. M., Shapley, A. E., Erb, D. K., et al. 2011, ApJ, 731, 65

Förster Schreiber, N. M., Genzel, R., Lehnert, M. D., et al. 2006, ApJ, 645, 1062

Förster Schreiber, N. M., Genzel, R., Bouché, N., et al. 2009, ApJ, 706, 1364

Freeman, K. C. 1970, ApJ, 160, 811

Frye, B. L., Bowen, D. V., Hurley, M., et al. 2008, ApJL, 685, L5

Galametz, A., Stern, D., De Breuck, C., et al. 2012, ApJ, 749, 169

Garn, T., & Best, P. N. 2010, MNRAS, 409, 421

Geach, J. E., Smail, I., Best, P. N., et al. 2008, MNRAS, 388, 1473

Gehrels, N. 1986, ApJ, 303, 336

Genel, S., Fall, S. M., Hernquist, L., et al. 2015, ApJL, 804, L40

Genzel, R., Newman, S., Jones, T., et al. 2011, ApJ, 733, 101

Genzel, R., Tacconi, L. J., Combes, F., et al. 2012, ApJ, 746, 69

Genzel, R., Tacconi, L. J., Lutz, D., et al. 2015, ApJ, 800, 20

Gnerucci, A., Marconi, A., Cresci, G., et al. 2011, A&A, 528, A88

Greene, J. E., Leauthaud, A., Emsellem, E., et al. 2017, ApJL, 851, L33

Gunn, J. E., & Gott, III, J. R. 1972, ApJ, 176, 1

Harrison, C. M., Johnson, H. L., Swinbank, A. M., et al. 2017, MNRAS, 467, 1965

Hatch, N. A., Kurk, J. D., Pentericci, L., et al. 2011, MNRAS, 415, 2993

Hayashi, M., Kodama, T., Tadaki, K.-i., Koyama, Y., & Tanaka, I. 2012, ApJ, 757, 15

Hayashi, M., Kodama, T., Tanaka, I., et al. 2016, ApJL, 826, L28

Hayashi, M., Kodama, T., Kohno, K., et al. 2017, ApJL, 841, L21

Hine, N. K., Geach, J. E., Alexander, D. M., et al. 2016, MNRAS, 455, 2363

Hodge, J. A., Karim, A., Smail, I., et al. 2013, ApJ, 768, 91

Hopkins, P. F., Cox, T. J., Younger, J. D., & Hernquist, L. 2009, ApJ, 691, 1168

Houghton, R. C. W. 2015, MNRAS, 451, 3427

Hubble, E. P. 1926, ApJ, 64, doi:10.1086/143018

—. 1936, Realm of the Nebulae

Hung, C.-L., Casey, C. M., Chiang, Y.-K., et al. 2016, ApJ, 826, 130

Ibar, E., Sobral, D., Best, P. N., et al. 2013, MNRAS, 434, 3218

Ichikawa, T., Suzuki, R., Tokoku, C., et al. 2006, in Proc. SPIE, Vol. 6269, Society of Photo-Optical Instrumentation Engineers (SPIE) Conference Series, 626916

Icke, V. 1985, A&A, 144, 115

Jeans, J. H. 1902, Philosophical Transactions of the Royal Society of London Series A, 199, 1

Kajisawa, M., Kodama, T., Tanaka, I., Yamada, T., & Bower, R. 2006, MNRAS, 371, 577

Kashikawa, N., Kitayama, T., Doi, M., et al. 2007, ApJ, 663, 765

Kassin, S. A., Weiner, B. J., Faber, S. M., et al. 2007, ApJL, 660, L35

—. 2012, ApJ, 758, 106

Keating, G. K., Marrone, D. P., Bower, G. C., et al. 2016, ApJ, 830, 34

Kennicutt, R. C., & Evans, N. J. 2012, ARA&A, 50, 531

Kennicutt, Jr., R. C. 1998a, ARA&A, 36, 189

—. 1998b, ApJ, 498, 541

Knopp, G. P., & Chambers, K. C. 1997, ApJS, 109, 367

Kodama, T., Hayashi, M., Koyama, Y., et al. 2015, in IAU Symposium, Vol. 309, Galaxies in 3D across the Universe, ed. B. L. Ziegler, F. Combes, H. Dannerbauer, & M. Verdugo, 255–258

Kormendy, J., & Ho, L. C. 2013, ARA&A, 51, 511

Koyama, Y., Kodama, T., Tadaki, K.-i., et al. 2014, ApJ, 789, 18

Koyama, Y., Smail, I., Kurk, J., et al. 2013, MNRAS, 434, 423

Kulas, K. R., McLean, I. S., Shapley, A. E., et al. 2013, ApJ, 774, 130

Kurk, J., Cimatti, A., Zamorani, G., et al. 2009, A&A, 504, 331

Kurk, J. D., Röttgering, H. J. A., Pentericci, L., et al. 2000, A&A, 358, L1

Lagache, G., Dole, H., Puget, J.-L., et al. 2004, ApJS, 154, 112

Lagos, C. D. P., Baugh, C. M., Lacey, C. G., et al. 2011, MNRAS, 418, 1649

Lagos, C. d. P., Bayet, E., Baugh, C. M., et al. 2012, MNRAS, 426, 2142

Lagos, C. d. P., Stevens, A. R. H., Bower, R. G., et al. 2018, MNRAS, 473, 4956

Larson, R. B., Tinsley, B. M., & Caldwell, C. N. 1980, ApJ, 237, 692

Le Fevre, O., Deltorn, J. M., Crampton, D., & Dickinson, M. 1996, ApJL, 471, L11

Lee, K.-G., Hennawi, J. F., Stark, C., et al. 2014, ApJL, 795, L12

Lee, M. M., Tanaka, I., Kawabe, R., et al. 2017, ApJ, 842, 55

Lee, N., Sanders, D. B., Casey, C. M., et al. 2015, ApJ, 801, 80

Lelli, F., McGaugh, S. S., & Schombert, J. M. 2016, ApJL, 816, L14

Madau, P., & Dickinson, M. 2014, ARA&A, 52, 415

Madau, P., Ferguson, H. C., Dickinson, M. E., et al. 1996, MNRAS, 283, 1388

Magdis, G. E., Daddi, E., Béthermin, M., et al. 2012, ApJ, 760, 6

Magdis, G. E., Bureau, M., Stott, J. P., et al. 2016, MNRAS, 456, 4533

Mannucci, F., Cresci, G., Maiolino, R., Marconi, A., & Gnerucci, A. 2010, MNRAS, 408, 2115

Martig, M., Bournaud, F., Teyssier, R., & Dekel, A. 2009, ApJ, 707, 250

Matsuda, Y., Richard, J., Smail, I., et al. 2010, MNRAS, 403, L54

Matsuda, Y., Smail, I., Geach, J. E., et al. 2011, MNRAS, 416, 2041

Mayo, J. H., Vernet, J., De Breuck, C., et al. 2012, A&A, 539, A33

McMullin, J. P., Waters, B., Schiebel, D., Young, W., & Golap, K. 2007, in Astronomical Society of the Pacific Conference Series, Vol. 376, Astronomical Data Analysis Software and Systems XVI, ed. R. A. Shaw, F. Hill, & D. J. Bell, 127

Miller, T. B., Hayward, C. C., Chapman, S. C., & Behroozi, P. S. 2015, MNRAS, 452, 878

Mo, H. J., & Mao, S. 2004, MNRAS, 353, 829

Mo, H. J., Mao, S., & White, S. D. M. 1998, MNRAS, 295, 319

Moore, B., Katz, N., Lake, G., Dressler, A., & Oemler, A. 1996, Nature, 379, 613

Moore, B., Lake, G., & Katz, N. 1998, ApJ, 495, 139

Moore, B., Quinn, T., Governato, F., Stadel, J., & Lake, G. 1999, MNRAS, 310, 1147

Mortlock, A., Conselice, C. J., Bluck, A. F. L., et al. 2011, MNRAS, 413, 2845

Muldrew, S. I., Hatch, N. A., & Cooke, E. A. 2015, MNRAS, 452, 2528

Muldrew, S. I., Croton, D. J., Skibba, R. A., et al. 2012, MNRAS, 419, 2670

Nipoti, C., & Binney, J. 2007, MNRAS, 382, 1481

Noble, A. G., McDonald, M., Muzzin, A., et al. 2017, ApJL, 842, L21

Noeske, K. G., Weiner, B. J., Faber, S. M., et al. 2007, ApJL, 660, L43

Obreschkow, D., & Glazebrook, K. 2014, ApJ, 784, 26

Obreschkow, D., Heywood, I., Klöckner, H.-R., & Rawlings, S. 2009, ApJ, 702, 1321

Obreschkow, D., & Rawlings, S. 2009, ApJL, 696, L129

Oemler, Jr., A. 1974, ApJ, 194, 1

Orsi, Á. A., Fanidakis, N., Lacey, C. G., & Baugh, C. M. 2016, MNRAS, 456, 3827

Oteo, I., Sobral, D., Ivison, R. J., et al. 2015, MNRAS, 452, 2018

Ouchi, M., Shimasaku, K., Akiyama, M., et al. 2005, ApJL, 620, L1

Pascarelle, S. M., Windhorst, R. A., Driver, S. P., Ostrander, E. J., & Keel, W. C. 1996, ApJL, 456, L21

Peng, Y.-j., Lilly, S. J., Kovač, K., et al. 2010, ApJ, 721, 193

Perlmutter, S., Aldering, G., Goldhaber, G., et al. 1999, ApJ, 517, 565

Planck Collaboration, Ade, P. A. R., Aghanim, N., et al. 2015, A&A, 582, A29

—. 2016, A&A, 594, A13

Price, S. H., Kriek, M., Shapley, A. E., et al. 2016, ApJ, 819, 80

Puech, M., Flores, H., Hammer, F., et al. 2008, A&A, 484, 173

Rau, U., & Cornwell, T. J. 2011, A&A, 532, A71

Rees, M. J., & Ostriker, J. P. 1977, MNRAS, 179, 541

Reyes, R., Mandelbaum, R., Gunn, J. E., Pizagno, J., & Lackner, C. N. 2011, MNRAS, 417, 2347

Riechers, D. A., Capak, P. L., Carilli, C. L., et al. 2010, ApJL, 720, L131

Riess, A. G., Filippenko, A. V., Challis, P., et al. 1998, AJ, 116, 1009

Riess, A. G., Macri, L. M., Hoffmann, S. L., et al. 2016, ApJ, 826, 56

Rigby, J. R., Marcillac, D., Egami, E., et al. 2008, ApJ, 675, 262

Rocca-Volmerange, B., Le Borgne, D., De Breuck, C., Fioc, M., & Moy, E. 2004, A&A, 415, 931

Roettgering, H. J. A., van Ojik, R., Miley, G. K., et al. 1997, A&A, 326, 505

Romanowsky, A. J., & Fall, S. M. 2012, ApJS, 203, 17

Ruel, J., Bazin, G., Bayliss, M., et al. 2014, ApJ, 792, 45

Saintonge, A., Lutz, D., Genzel, R., et al. 2013, ApJ, 778, 2

Saito, T., Iono, D., Yun, M. S., et al. 2015, ApJ, 803, 60

Sakamoto, K., Aalto, S., Costagliola, F., et al. 2013, ApJ, 764, 42

Santini, P., Fontana, A., Grazian, A., et al. 2009, A&A, 504, 751

Santini, P., Maiolino, R., Magnelli, B., et al. 2014, A&A, 562, A30

Sargent, M. T., Daddi, E., Béthermin, M., et al. 2014, ApJ, 793, 19

Schinnerer, E., Groves, B., Sargent, M. T., et al. 2016, ApJ, 833, 112

Scott, N., Davies, R. L., Houghton, R. C. W., et al. 2014, MNRAS, 441, 274

Scoville, N., Arnouts, S., Aussel, H., et al. 2013, ApJS, 206, 3

Scoville, N., Aussel, H., Sheth, K., et al. 2014, ApJ, 783, 84

Scoville, N., Sheth, K., Aussel, H., et al. 2016, ApJ, 820, 83

Scoville, N., Lee, N., Vanden Bout, P., et al. 2017, ApJ, 837, 150

Seko, A., Ohta, K., Yabe, K., et al. 2016, ApJ, 819, 82

Sersic, J. L. 1968, Atlas de Galaxias Australes

Seymour, N., Stern, D., De Breuck, C., et al. 2007, ApJS, 171, 353

Shapley, A. E., Steidel, C. C., Pettini, M., & Adelberger, K. L. 2003, ApJ, 588, 65

Shimakawa, R., Kodama, T., Tadaki, K.-i., et al. 2015, MNRAS, 448, 666

—. 2014, MNRAS, 441, L1

Shimasaku, K., Ouchi, M., Okamura, S., et al. 2003, ApJL, 586, L111

Shivaei, I., Kriek, M., Reddy, N. A., et al. 2016, ApJL, 820, L23

Shivaei, I., Reddy, N. A., Shapley, A. E., et al. 2017, ApJ, 837, 157

Simons, R. C., Kassin, S. A., Trump, J. R., et al. 2016, ApJ, 830, 14

Simons, R. C., Kassin, S. A., Weiner, B. J., et al. 2017, ApJ, 843, 46

Smail, I., Geach, J. E., Swinbank, A. M., et al. 2014, ApJ, 782, 19

Smolčić, V., Novak, M., Bondi, M., et al. 2017, A&A, 602, A1

Sobral, D., Best, P. N., Matsuda, Y., et al. 2012, MNRAS, 420, 1926

Sobral, D., Best, P. N., Smail, I., et al. 2014, MNRAS, 437, 3516

Sobral, D., Smail, I., Best, P. N., et al. 2013, MNRAS, 428, 1128

Sobral, D., Best, P. N., Geach, J. E., et al. 2009, MNRAS, 398, 75

Solomon, P. M., Downes, D., Radford, S. J. E., & Barrett, J. W. 1997, ApJ, 478, 144

Solomon, P. M., Rivolo, A. R., Barrett, J., & Yahil, A. 1987, ApJ, 319, 730

Solomon, P. M., & Vanden Bout, P. A. 2005, ARA&A, 43, 677

Speagle, J. S., Steinhardt, C. L., Capak, P. L., & Silverman, J. D. 2014, ApJS, 214, 15

Springel, V., Frenk, C. S., & White, S. D. M. 2006, Nature, 440, 1137

Steidel, C. C., Adelberger, K. L., Dickinson, M., et al. 1998, ApJ, 492, 428

Steidel, C. C., Rudie, G. C., Strom, A. L., et al. 2014, ApJ, 795, 165

Straatman, C. M. S., Glazebrook, K., Kacprzak, G. G., et al. 2017, ApJ, 839, 57

Strazzullo, V., Gobat, R., Daddi, E., et al. 2013, ApJ, 772, 118

Swinbank, A. M., Smail, I., Sobral, D., et al. 2012, ApJ, 760, 130

Tacconi, L. J., Genzel, R., Smail, I., et al. 2008, ApJ, 680, 246

Tacconi, L. J., Neri, R., Genzel, R., et al. 2013, ApJ, 768, 74

Tacconi, L. J., Genzel, R., Saintonge, A., et al. 2017, ArXiv e-prints, arXiv:1702.01140

Tadaki, K.-i., Kodama, T., Tanaka, I., et al. 2013, ApJ, 778, 114

Tadaki, K.-i., Kodama, T., Tamura, Y., et al. 2014, ApJL, 788, L23

Tadaki, K.-i., Genzel, R., Kodama, T., et al. 2017, ApJ, 834, 135

Tanaka, I., De Breuck, C., Kurk, J. D., et al. 2011, PASJ, 63, 415

Tiley, A. L., Stott, J. P., Swinbank, A. M., et al. 2016, MNRAS, 460, 103

Toomre, A. 1964, ApJ, 139, 1217

—. 1977, ARA&A, 15, 437

Toomre, A., & Toomre, J. 1972, ApJ, 178, 623

Toshikawa, J., Kashikawa, N., Ota, K., et al. 2012, ApJ, 750, 137

Toshikawa, J., Kashikawa, N., Overzier, R., et al. 2014, ApJ, 792, 15

Tran, K.-V. H., Nanayakkara, T., Yuan, T., et al. 2015, ApJ, 811, 28

Tully, R. B., & Fisher, J. R. 1977, A&A, 54, 661

Turner, O. J., Harrison, C. M., Cirasuolo, M., et al. 2017a, ArXiv e-prints, arXiv:1711.03604

Turner, O. J., Cirasuolo, M., Harrison, C. M., et al. 2017b, MNRAS, 471, 1280

Übler, H., Förster Schreiber, N. M., Genzel, R., et al. 2017, ApJ, 842, 121

Ueda, J., Iono, D., Yun, M. S., et al. 2014, ApJS, 214, 1

Umehata, H., Tamura, Y., Kohno, K., et al. 2014, MNRAS, 440, 3462

—. 2015, ApJL, 815, L8

—. 2017, ApJ, 835, 98

Valentino, F., Daddi, E., Strazzullo, V., et al. 2015, ApJ, 801, 132

van Dokkum, P. G., Whitaker, K. E., Brammer, G., et al. 2010, ApJ, 709, 1018

van Dokkum, P. G., Nelson, E. J., Franx, M., et al. 2015, ApJ, 813, 23

Veale, M., Ma, C.-P., Greene, J. E., et al. 2017, MNRAS, 471, 1428

Venemans, B. P., Kurk, J. D., Miley, G. K., et al. 2002, ApJL, 569, L11

Venemans, B. P., Röttgering, H. J. A., Overzier, R. A., et al. 2004, A&A, 424, L17

Venemans, B. P., Röttgering, H. J. A., Miley, G. K., et al. 2007, A&A, 461, 823

Verdes-Montenegro, L., Yun, M. S., Williams, B. A., et al. 2001, A&A, 377, 812

Walter, F., Decarli, R., Sargent, M., et al. 2014, ApJ, 782, 79

Wang, T., Elbaz, D., Daddi, E., et al. 2016, ApJ, 828, 56

Weigel, A. K., Schawinski, K., Caplar, N., et al. 2017, ApJ, 845, 145

Weiner, B. J., Willmer, C. N. A., Faber, S. M., et al. 2006, ApJ, 653, 1027

Whitaker, K. E., van Dokkum, P. G., Brammer, G., & Franx, M. 2012, ApJL, 754, L29

Whitaker, K. E., Franx, M., Leja, J., et al. 2014, ApJ, 795, 104

White, S. D. M., & Frenk, C. S. 1991, ApJ, 379, 52

White, S. D. M., & Rees, M. J. 1978, MNRAS, 183, 341

Wisnioski, E., Förster Schreiber, N. M., Wuyts, S., et al. 2015, ApJ, 799, 209

Wuyts, E., Rigby, J. R., Gladders, M. D., & Sharon, K. 2014, ApJ, 781, 61

Wuyts, S., Förster Schreiber, N. M., van der Wel, A., et al. 2011, ApJ, 742, 96

Yun, M. S., Reddy, N. A., & Condon, J. J. 2001, ApJ, 554, 803

Yun, M. S., Aretxaga, I., Gurwell, M. A., et al. 2015, MNRAS, 454, 3485

The original LaTeXtemplate has been obtained at github.com/suchow/Dissertate under the permissive agpl license. The fonts and the style (including the header style, paper handling, and chapter design) of the template has been modified by myself to consider the overall structure and the appearance of the presented Dissertation and to incorporate with the university guidelines.

Appendix A

Flux measurement for measuring gas content

A.1 Flux versus S/N

We check whether the peak flux is consistent with other flux measurements, i.e., Gaussian fitting (using CASA commend `imfit`) and aperture photometry that is clipped below the 2.6 σ. For the CO (3–2) measurement, we also tested the spectra-based fitting by integrating the spectrum by using CASA `specfit`, if it is available for each smoothed image. All data are measured from the primary beam corrected maps. Furthermore, except for HAE16 in Band 6, all of the sources are within a good sensitivity region. While some compact sources (in the original image) with a high S/N ($\sim$ 10) have peak flux values consistent with those of other methods, the relatively low S/N (S/N$\leq$ 7) with extended ALMA detections do not ensure that a Gaussian fitting is a secure method. Therefore, taking a peak flux would be a more robust method to maximize the S/N and consider a galaxy as an unresolved source.

We investigate the growth curve of a galaxy to optimize the smoothing kernel and then to estimate a flux (Fig. A1 and A2). The growth curve gradually approaches the maximum value, while the S/N reaches a peak and then decreases as the noise level increases and the smoothing Gaussian kernel becomes larger. In some cases, the peak flux decreases after it has reached a peak because of contamination in side-lobes in interferometric data sets or contamination from nearby galaxies (on the map). Smoothing major axis = 0.0 implies no smoothing. We tested

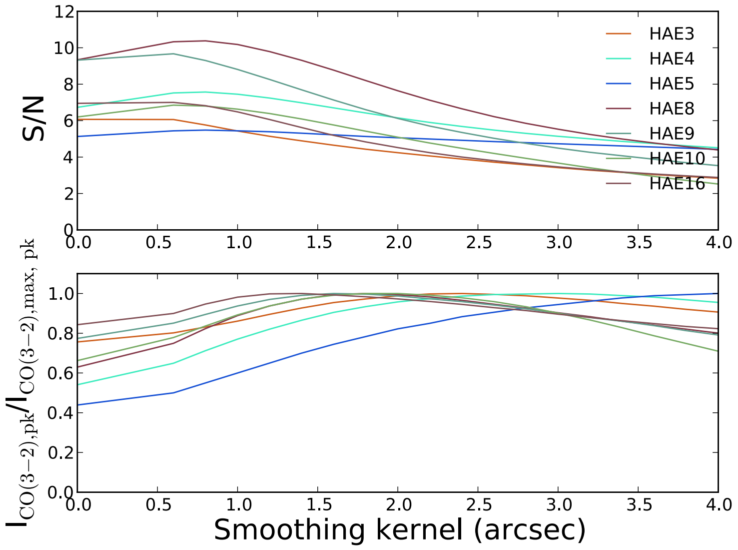

Figure A1: S/N and peak flux growth curve in Band 3. We need to consider both S/N and flux to optimize the smoothing parameter to estimate a total flux. We have chosen a kernel of 0.6 ″ to conduct uniform analysis with Band 6 data as well. At this kernel, the expected flux recovered at least 50% of the maximum flux (but with low S/N).

growth curves using kernels of 0″.4 to 4″.0 in steps of 0″.2 (convolved beam size = 0.8 to 4.1) for Band 6 and 0.6 to 4.0 for Band 3 (convolved beam size = ∼ 0″.9 to 4″.1). Combining all the growth curves in Band 3 and Band 6, we decided to use the Gaussian kernel of 0″.8 for Band 6 and 0″.6 for Band 3.

A.2 Position error

We investigated the peak position consistency between the Hα position (I. Tanaka et al., in preparation) and CO (3–2) or 1.1 mm. The observations have a similar resolution of ∼ 0″.7-0″.9. Figure A3 shows how far the peak position is offset in CO (3–2) and 1.1 mm images with respect to the NB position. The position error expected from the interferometric data depends on the S/N and synthesized beam size. The expected position error is ∼ 0″.1. More errors that could be associated with the phase error in the phase calibrator may be added. Compared to this, the position accuracy for NB compared to 2MASS is 0″.044 (I.Tanaka et al., in preparation).

While we conclude that the position is *roughly* consistent with each other within ∼ 0″.4 resolution, we note that there might be a systematic offset in the peak position of CO(3-2) and 1.1 mm compared to the Hα peak (on average ∼ 0″.2). The source with the highest offset is HAE4

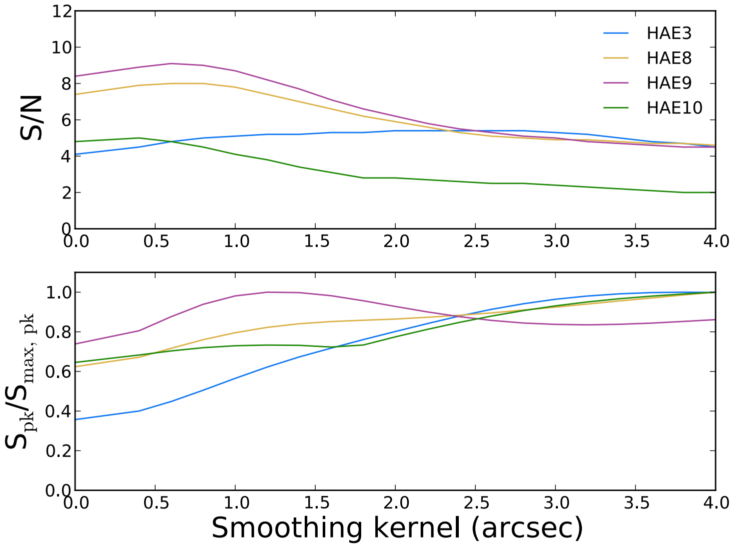

Figure A2: Same growth curve as in Fig. A1 but for Band 6. Again, although the peak flux is recovered less with the adopted kernel of $0.8''$, they have a low S/N, suggesting large uncertainties are also clearly included in the brightest peak.

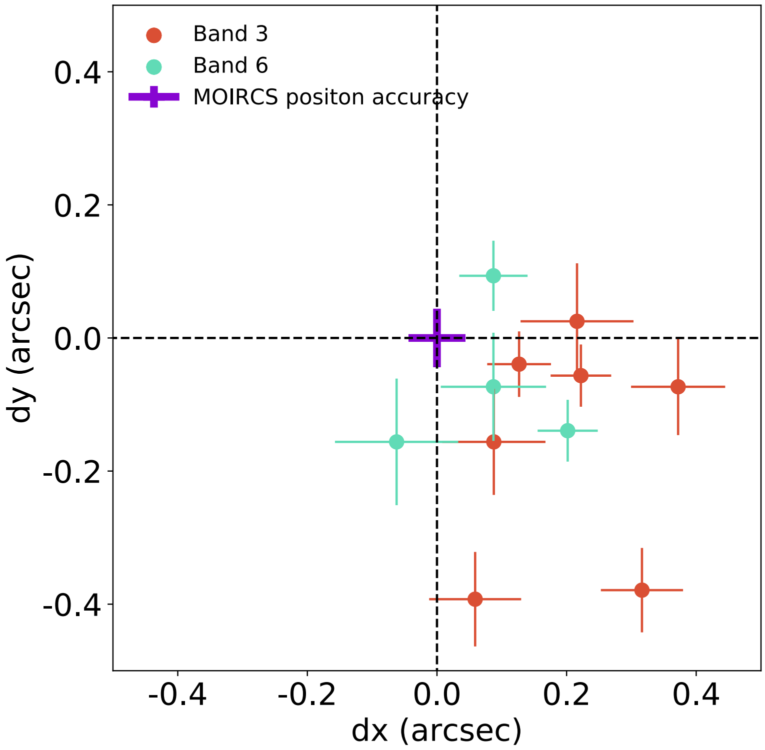

Figure A3: Position offset with respect to the NB catalogue. We find that the position is roughly consistent with each other within $\sim 0''.4$. Torquious circles indicate Band 6 1.1 mm observations and crimson circles indicate Band 3 CO (3–2) observations.The position accuracy for NB compared to 2MASS is $0''.044$ (I. Tanaka et al., in preparation).

(see also Fig. 3.2 ; the distribution of Hα is extended compared to the distribution of CO(3-2) or 1.1 mm). The position difference between the Hα, CO (3–2) and 1.1 mm, therefore, appears to originate from the difference in the internal structure of a galaxy and/or the effect of dust extinction. Further discussion should be conducted with a higher resolution and high sensitivity observation.

Appendix B

GalPaK^{3D} results

B.1 MCMC correlations

Figure B1 and B2 show the GalPaK^{3D} results showing the correlations between parameters.

B.2 Data and model in channel maps

Figure B3 and B4 show the channel maps with the model and residuals.

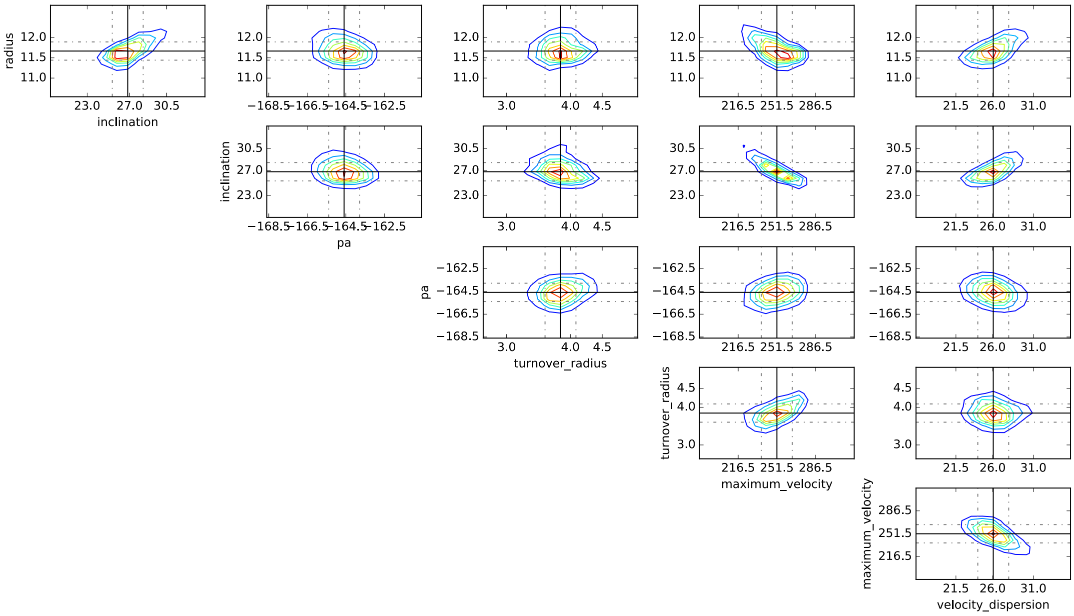

Figure B1: The MCMC correlation plot for HAE8.

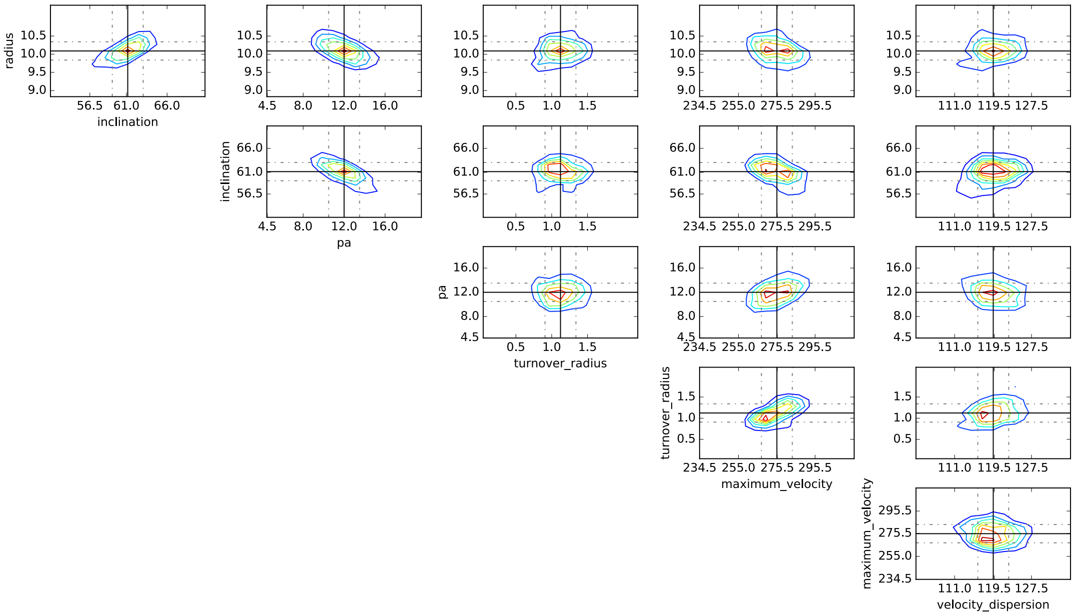

Figure B2: The MCMC correlation plot for HAE16.

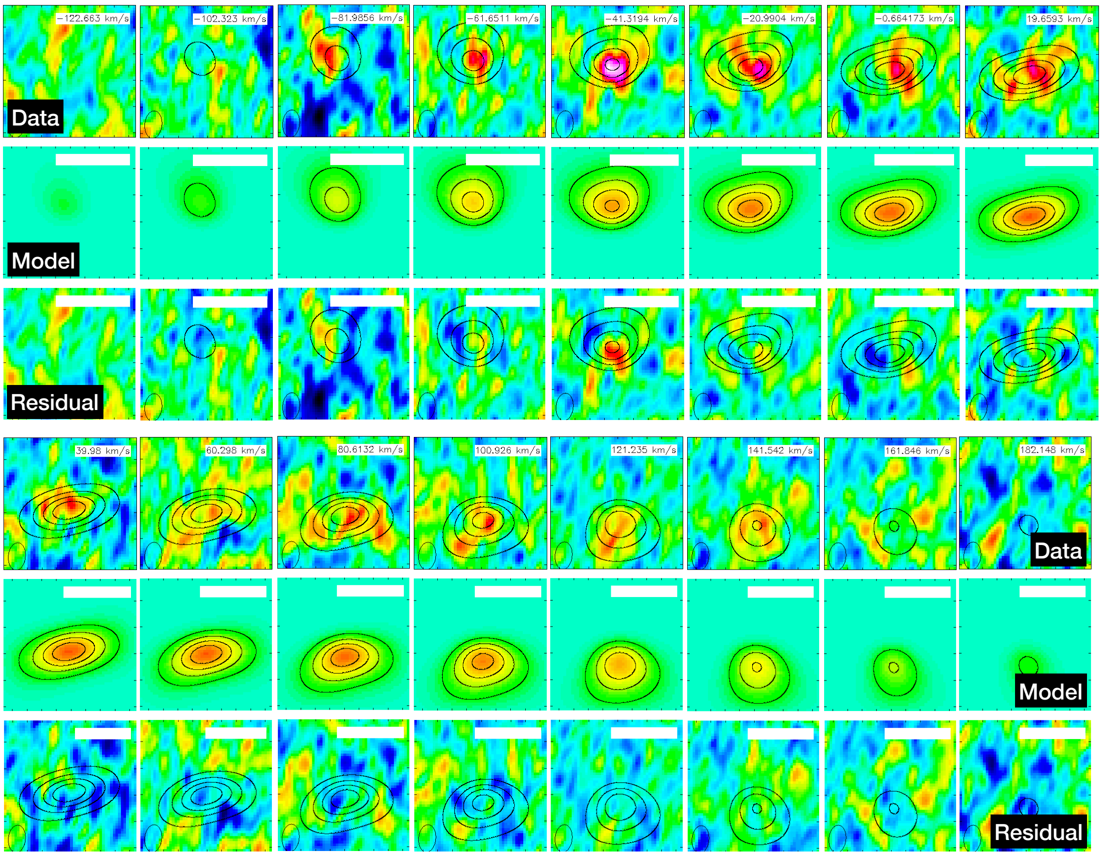

Figure B3: The channel maps for HAE8 in steps of $\sim\ 20\ \mathrm{km\,s^{-1}}$. Three panels in a column is data (top), model (middle) and residual (bottom). From right to left : increasing velocity starting from $\sim\ 123\ \mathrm{km\,s^{-1}}$. The contours are from model data cube, showing 20%, 40%, 60%, 80% of the peak flux.

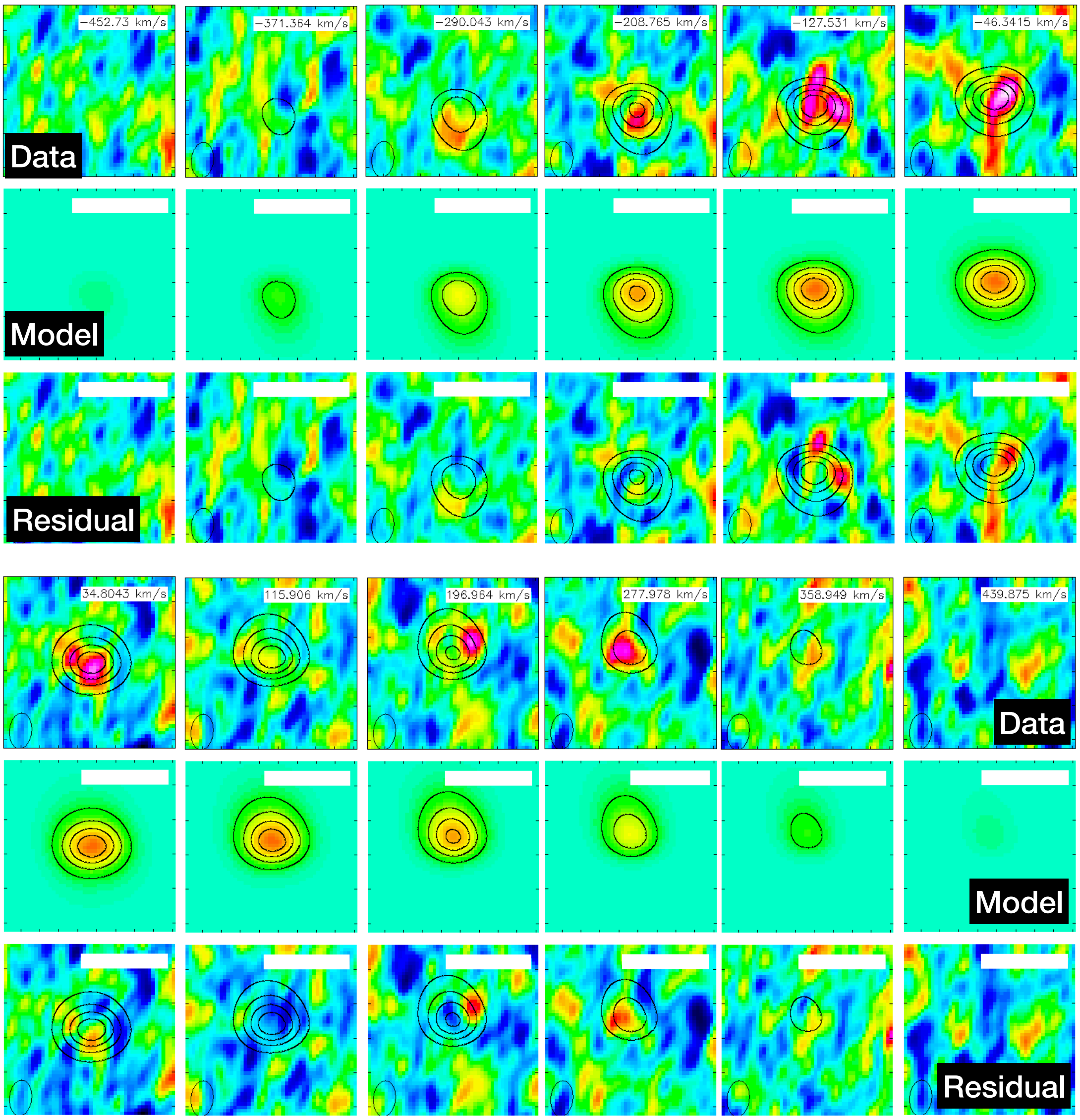

Figure B4: The channel maps for HAE16 in steps of $\sim$ 80 km s^{-1}. Three panels in a column is data (top), model (middle) and residual (bottom). From right to left : increasing velocity starting from $\sim$ 453 km s^{-1}.

> *We must reason in natural philosophy not from what we hope, or even expect, but from what we perceive.*
>
> Humphry Davy

Appendix C

Continuum emission from cm to mm in star forming galaxies

A part of the report on the dust continuum and JVLA observations on main-sequence HAEs will be included in the paper which will be submitted to ApJ.

This appendix reports three of the deepest observations ever made in a single field (FWHM = 7.5-15 arcmin) in two radio frequencies and at 2-mm toward the protocluster region. The former observations were carried out to trace the rest-frame ∼10 GHz (the depth at this frequency is comparable to the depth of the COSMOS field (e.g., Smolčić et al. [2017]) and ∼20 GHz emission that are both thought to be originated mostly from synchrotron emission (and to trace extinction-free star-forming activity), and the latter 2-mm observations were executed to detect the redshifted fine structure line of atomic carbon [CI](1-0) and 570 μm dust continuum [*].

We present the summary of these observations here to aid the findings discussed in Chapter 3 and Chapter 4 and to give our future prospects for probing protocluster galaxies.

C.1 Observations

C.1.1 ALMA

Two Band 4 observations were carried out under our ALMA Cycle 3 program

(ID : #2015.1.00152.S, PI : Minju Lee). Two spectral set-ups were used for targeting CO (4–3) and [CI] lines (see for CO (4–3) spectral configuration in Chap 4). 38 and 39 antennas were used in the observations with the unprojected length $L_{\rm baseline}$ between 15 m and 3.1 km (C40-6) for three days (2016 September 23,24 and 25) and total on-source time of $T_{\rm integ}$ = 2.7 hours. Four spectral windows (SPW) are set for the correlator, two of which were set to each sideband. For a SPW where the redshifted [CI] is expected to be observed, we set in the FDM with a 1.875 GHz bandwidth and 7.812 MHz resolution ($\sim$ 16.6 km s^{-1}). The remainder of three SPWs are observed in the TDM mode with a 2.0 GHz bandwidth and 15.625 MHz resolution to cover dust continuum at 2.27 mm. A quasar J2148+0657, J2025+3343, J1751+0939 was chosen for bandpass and/or flux calibration. Phase calibrator was J2114+2832.

We performed calibration using the Common Astronomy Software Applications package (`CASA`, McMullin et al. 2007). We used `CASA` versions of 4.7.0 and 5.1.0 for the calibration and the imaging, respectively. Calibration processes were done with the pipeline with the script provided by EA-ARC. Images are produced by `CASA` task, `tclean`. For continuum imaging, we combined the lower frequency coverage in Band 4 that was used for CO (4–3) detection to get higher S/N for continuum detection. By combining the all of the available data, which almost the doubled the bandwidth, the noise level decreased by $\sim$ 20% with the typical noise level of

---

[*] Except for the case of the radio galaxy

7.9 μJy beam^{-1}. The final synthesized beam after the data combining is $0''47. \times 0''.30$ with a natural weighting in `tclean`.

C.1.2 JVLA

Deep Jansky Very Large Array (JVLA) continuum observations were executed in 2012 for S-band (3 GHz, PI : Kenta Suzuki) and in 2015 C-band (6 GHz, PI : Minju Lee). 26-27 antennas were used in A-configuration (maximum baseline length 36.4 km) delivering the synthesize beam of $0''.69 \times 0.''.64$ and $0''.39 \times 0.''.38$ at S-band and C-band, respectively. The S-band spectrum configuration consists total of 16 sub-bands that ranges between 2 GHz and 4 GHz and individual sub-bands are divided into 64 channels corresponding to a spectral resolution of 2 MHz. The C-band configuration consists total of 32 sub-bands that ranges between 4 and 8 GHz and individual sub-bands are again divided into 64 channels corresponding to a spectral resolution of 2 MHz. A quasar 3C48 was chosen for bandpass and flux calibration and a phase calibrator was J2115+2933 for both C and S band observations. We used `CASA` versions 5.0.0 for the calibration to use the up-to-date EVLA pipeline 1.4.0 version. Imaging is done with the 5.1.0 version. For S-band imaging, we ignored the frequency range 2.11 - 2.37 GHz (spw# = 1 and 2) to minimize the effect of Radio Frequency Interferences (RFIs), the artificial signals from the earth, where the effect is strongest. For C-band, we generally used the whole frequency range. Since the size of the data is so huge, we ran `tclean` imaging in parallel. For parallel processing, we make a partition file by typing CASA commend `partition` for concatenated visibility and started casa with multiple-cores[†]. Images are produced by `CASA` task, `tclean` using a distinct deconvolver, Multi-term (Multi Scale) Multi-Frequency Synthesis (mtmfs) (Rau & Cornwell [2011]) to consider the extended structure like a radio lobe. Ideally, one may need additional option to take into account the wide field of view of S-band and C-band with respect to its beam size, for example w-projection, and a-projection. Since this was hardly cooperated with the current computing power in hand, I defer further sophisticated imaging process (see also discussion in the following sections) as a future task.

The typical noise level in the final image varies as a function of distance from the center. Typically, the noise level near the center, where the radio galaxy 4C 23.56 is located, is the highest and it decreases as a function of the distance from the radio galaxy. The dependency is occurred

---

[†] `https://casa.nrao.edu/docs/UserMan/casa_cookbook011.html`

not owing to the sensitivity of the antenna (which decreases as a function of radius from the center), but largely due to artificial signals near the strong source (see also, Smolčić et al. [2017]). A noise level ranges between [0.4-4.0] μJy beam^{-1} for S-band and [1.7-5.0] μJy beam^{-1} for C-band on the image for which primary beam correction unregistered. Given the noise level and the flux of the brightest flux from the radio galaxy, the dynamic ranges are extremely high, as high as $\sim$ 73000 for S-band and $\sim$ 7000 for C-band. This limits our imaging procedure in addition to the effect from the existence of RFIs. Of our interest region is the overdense region of HAEs close to the radio galaxy, where the noise level is typically high than the outer region.

C.2 Results

C.2.1 Rest-frame submm continuum

We gather all available continuum data from our ALMA observations. This results in total of three bands, 1.1 mm (Band 6), 2.6 mm (Band 4), and 3 mm (Band 3). At $z = 2.5$, these three bands correspond to rest-frame 280, 570 and 870 μm, respectively. Therefore, for star forming galaxies, these bands all traces the continuum emission from dust component within a galaxy.

As seen in Chapter 3, 1.1 mm is detected for HAE 3, 8, 9 and 10. We apply the same detection criteria for these bands; we regard as a detection if the peak flux is above 4 σ. In Figure B1, we show the postage stamps for HAEs if they have at least one detection in the underlying frequency ranges.

In 2 mm, we detect continuum from 4 galaxies, HAE 1, 7, 9 and 16 and marginal detection (3 σ) for HAE3 and HAE8. Related to new detection in HAE7 and HAE 16, they are both observed near the edge of the FoV in Band 6, the sensitivity is degraded so that ‘non-detection’ can be occurred. The non-detection in HAE 1 may be due to its low star forming activity (Theresa et al., in prep.) and/or due to its higher dust temperature.

In 3 mm, we detect continuum clearly from one galaxy, HAE 1, and a marginal detection in HAE 9.

HAE 1, the radio galaxy is detected in both band 3 and band 4, and the spectral index indicates that the emission in both bands traces the synchrotron emission, not from dust thermal continuum.

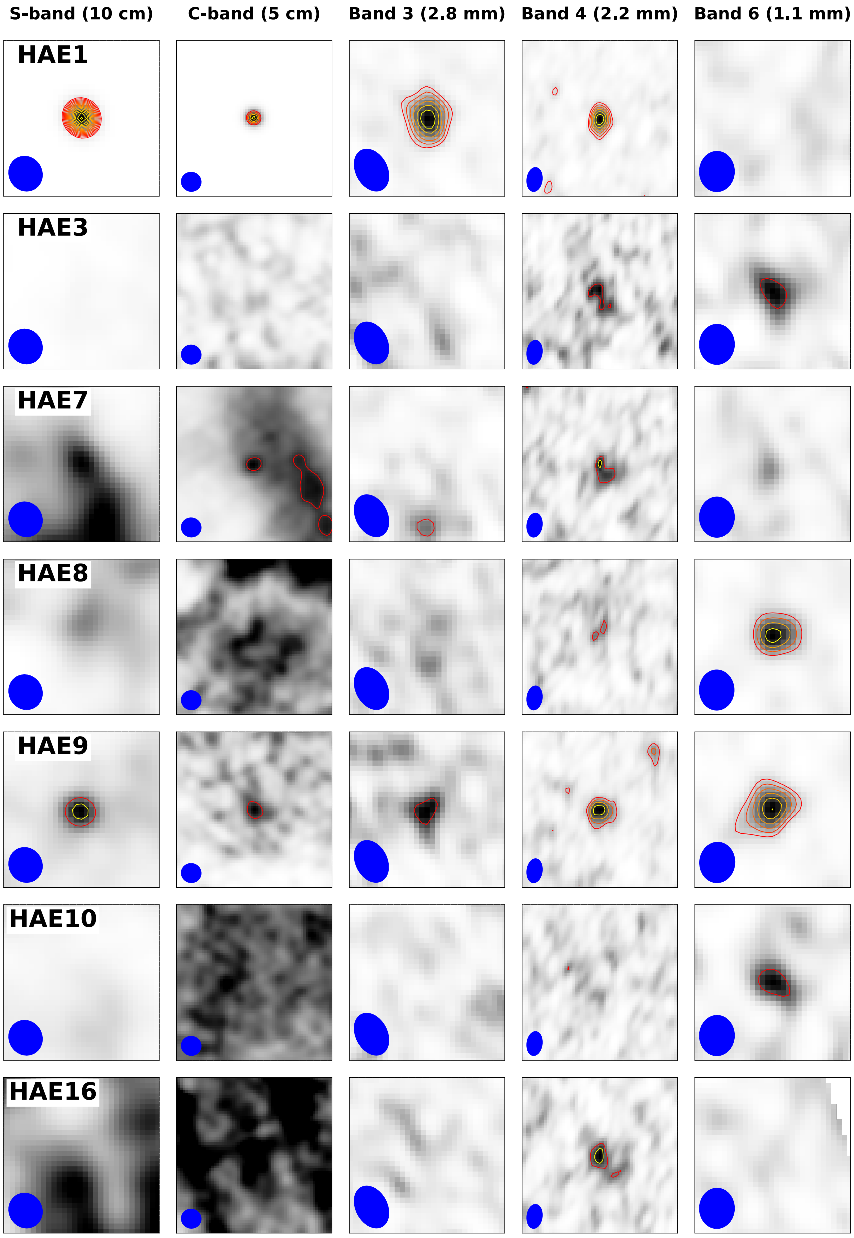

Figure B1: The postage stamps of galaxies detected in any observed bands from cm to mm wavelengths. We show galaxies if at least one band is detected. From left to right, we present images in the order of increasing frequency : S-band (13 cm), C-band (6 cm), Band 3 (3 mm), Band 4 (2.1 mm) and Band 6 (1.1 mm). On each panel, a blue filled circle is plotted for showing the beam size. The panel size for all postage stamps is in width of $3''$. Contours are basically plotted from $3\ \sigma$ in steps of $1\ \sigma$, i.e.,$4\ \sigma$,$5\ \sigma$, ..,. except for the radio galaxy in S-band and C-band. For the radio galaxy in the cm detection, the contours at starting from $1000\ \sigma$ in steps of $100\ \sigma$.

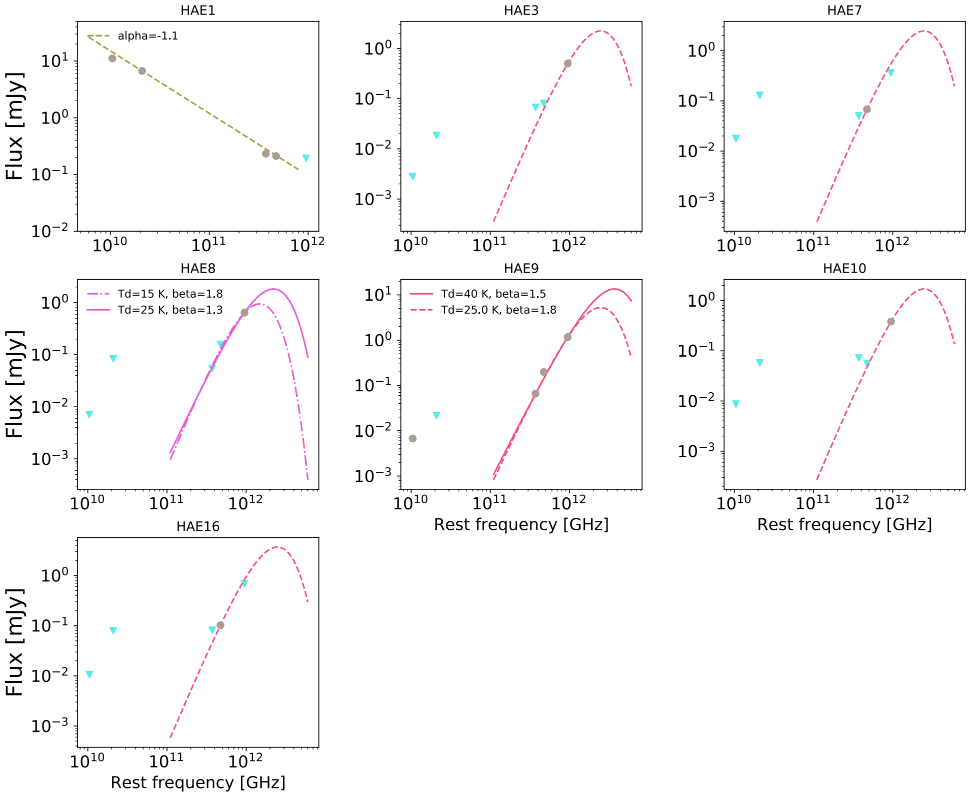

Figure B2: The data point and greybody SED for HAEs. Except for the case of HAE 1 (radio galaxy) the data points are scaled to fit the greybody SED. For these six galaxies, we assume nominal values for dust ($T_\mathrm{d} = 25$ K) and dust emissivity ($\beta = 1.8$) except HAE8, where we instead choose either lower $\beta = 1.3$ or lower dust temperature ($T_\mathrm{d} = 15$ K). We perform a rough estimate owing to the small number of data points for fitting and to fact that the data points do not cover the frequencies near the dust SED peak. Without covering the data point near the dust peak, there is a degeneracy between two parameters. Such degeneracy can be seen for HAE8 and HAE 9. Their redshifts are all constrained by CO line detections. Upper limits in grey squares are shown for 3σ limit.

C.3 Radio continuum

We detect radio continuum securely only from HAE 1 and HAE 9 at S and C bands. Other galaxies are not detected due to the degrade of sensitivity near the radio galaxy.

C.4 Comparison with greybody SED

For deriving the SED of individual galaxies, the photometry is done after we match the resolution. The flux estimates are summarized in Table C.1. We note that the flux measured at 1.1 mm is not listed (refer to Table C.1). We show in parenthesis for the errors of radio galaxy in

μJy. To match the resolution with other lower resolution images, we smoothed the image with a Gaussian kernel for JVLA C-band and ALMA Band 4 data using casa task `imsmooth`. The final (smoothed) beam size of two bands are $0''.80 \times 0''.79$ and $0''.84 \times 0''.76$ for C band and Band 4, respectively, and they are comparable to other resolutions. For measuring the flux, we use `imfit` which fit the source structure with 2D Gaussian.

Table C.1: The continuum flux for S, C bands with JVLA and Band3 and Band4 with ALMA

ID	RA(J2000)	Dec(J2000)	3 GHz [μJy]	6GHz [μJy]	3 mm [μJy]	2.2 mm [μJy]
1	21:07:14.835	+23:31:45.00	1.1×10^4 (5.0)	6.7×10^3 (3.2)	195±23	0.14 ± 0.02
3	21:07:21.047	+23:31:13.900	<2.8	<18.6	<66.7	<79.7
7	21:07:15.514	+23:31:37.343	<17.7	<128.6	<50.3	71.1
8	21:07:15.942	+23:31:27.500	<7.1	<83.6	<54.6	<62.2
9	21:07:22.587	+23:31:43.200	4.5 ± 1.1	<21.7	61.6 ± 17	120.5 ± 22
10	21:07:15.715	+23:31:12.000	<8.7	<57.4	<72.0	<55.0
16	21:07:14.635	+23:31:15.443	<10.7	<79.2	<81.1	<88.3

Figure B2 shows the constructed SED for these galaxies. Overall, the detection is very limited. HAE 9 and HAE 1 only allow for further investigation.

We compare with the greybody SED by assuming a typical dust ($T_{\rm d} = 25$ K) and dust emissivity ($\beta = 1.8$). By comparing this the non-detection in galaxies are broadly well explained, i.e., the depth for the continuum detection was not enough. With the limited data point we have some degeneracy between dust emissivity and dust temperature.

Although we have detection in Herschel bands toward this field, the field is the crowded field of the protocluster that is hard to deblend this field. To further argue on the luminosity weighted dust temperature, we need further observations at higher frequencies with ALMA.

For HAE 1, the Band 3 and Band 4 detection is reasonably well explained by the synchrotron emission where we modeled the flux $\log(S(\nu)) \propto \alpha \log(\nu)$, and α is referred to as radio spectral index. This target is particularly studied by one of the collaborator so that this chapter do not attempt to study go in details. In brief, we calculate an upper limit from the non-detection in Band 6 giving a lower value for its star formation rate (Theresa et al. 2017 in prep.). A detailed analysis will be addressed in the co-authored paper, here we plot its SED with the detection from 2 mm and 3 mm and JVLA detection only with the radio spectral index $\alpha = -1.1$ for the radio core.

For HAE 9, this galaxy is of particular interest in the overall context of the Dissertation. The galaxy is detected in all bands of the rest-frame submm and is well explained by a typical grey-body SED. The galaxy might be undergoing a merger (section 4.5) with bright 1.1 mm ($S_{1.1} =$ 1.1 mJy) emission. We compare HAE 9 with ALESS galaxies which might have similar properties. The ALESS survey is the follow-up of ALMA observations for the SMGs detected by LABOCA on the APEX telescope (Hodge et al. [2013]). For a comparison of SED, we obtained the averaged SED from da Cunha et al. [2015], which is obtained by the MAGPHYS code. The typical flux at 1.1 mm for ALESS SMGs typically is higher than that of HAE 9 so, we re-scaled the SED to fit with the data (by $\sim 0.5\times$). When it is scaled, the average SED of ALESS SMGs is matched well with the three submm data points in HAE 9. We also compared the radio continuum with the ALESS SED. We find HAE 9 has a lower value than is expected from the ALESS SMG SED. Radio continuum in MAGPHYS code to derive the ALESS SED is calculated by assuming the fixed slopes for the thermal and non-thermal radio emissions (-0.1 for free-free and -0.8 for the synchrotron emission) and the radio/FIR correlation (e.g., Yun et al. [2001]). The estimated SFR from Hα is consistent with the expected value from the radio continuum assuming the known radio/FIR. The difference need to be investigated with future deeper observations, we can at least argue that HAE 9 is not hosting radio-loud AGN. If it hosts an AGN, we expect higher radio flux than the one expected from typical radio/FIR correlation.

C.5 Summary and future prospects

We reported the continuum detection and non-detection for HAEs given the data set from cm-to-mm (all 5 frequencies). Two secure detections are occurred in radio galaxy, HAE 1, and HAE 9, at least from two bands. Other galaxies are detected in one of the observed bands that covers three rest-frame submm wavelengths. Overall, data points including the non-detection, whose upper limit is set by the 3σ, are broadly explained by a typical grey body SED with the dust temperature of $T_{\rm d} = 25$ K and dust emissivity index $\beta = 1.8$. Given the degeneracy of two parameters in constraining the dust SED, we need higher frequency observations.

Radio continuum observations are originally conducted to trace the extinction-free emission from galaxies. Historically, the radio continuum emission has been used as a strong tool to pin-down the positions of SMGs, as an alternative tool. The expected depth of our radio observations are sufficient to detect star forming galaxies with star formation rate $\gtrsim 100\ \mathrm{M}_\odot\ \mathrm{yr}^{-1}$ on the main sequence. The main obstacle with the continuum imaging in our target is perhaps not only the depth itself but also the technically-related issues on imaging (and calibration). Importantly, the high dynamic range of near the radio galaxy is expected and careful treatment of the image is necessary. As described before, the value is as large as 73000 for S-band. The problem will be revisited in the near future with more sophisticate imaging method.


東京大学
THE UNIVERSITY OF TOKYO